

**AN INVESTIGATION OF THE MICROSTRUCTURE AND PROPERTIES  
OF A CRYOGENICALLY MECHANICALLY ALLOYED  
POLYCARBONATE- POLY(ETHER ETHER KETONE) SYSTEM**

**Julie Patricia Martin**

Dissertation submitted to the Faculty of the  
Virginia Polytechnic Institute and State University  
in partial fulfillment of the requirements for the degree of

Doctor of Philosophy

In

Materials Science and Engineering

Ronald G. Kander, Committee Chairman

Alexander O. Aning

Stephen L. Kampe

Brian J. Love

Thomas C. Ward

November 14, 2001

Blacksburg, VA

KEYWORDS: Mechanical alloying, Polycarbonate,  
Poly(ether ether ketone), PC, PEEK

Copyright 2001, Julie P. Martin

# **An Investigation of the Microstructure and Properties of a Cryogenically Mechanically Alloyed Polycarbonate- Poly(ether ether ketone) System**

Julie Patricia Martin

Committee Chairman: Ronald G. Kander

Materials Science and Engineering

## **Abstract**

This work investigates processing-microstructure-property relationships of a model cryogenically mechanically alloyed polymer-polymer system: polycarbonate (PC) and poly (ether ether ketone) (PEEK). Mechanically milled and alloyed powders were characterized using a variety of techniques including microscopy and thermal analysis. Cryogenically mechanically alloyed powders processed for 10 hours were shown to have a sub-micron level two-phase microstructure. These powders were processed into testable coupons using a mini ram-injection molder; microstructure and bulk mechanical properties of the coupons were investigated as a function of mechanical alloying and injection molding parameters. Atomic force microscopy, transmission electron microscopy, and scanning transmission X-ray microscopy revealed that the intimate blending achieved during the mechanical alloying process is not retained upon post-processing using a conventional polymer processing technique. Injection molded coupons were tested in 3-point bend mode via dynamic mechanical and quasi-static mechanical testing. Results demonstrated that no improvement in energy to break, strain at failure, or failure strength was achieved in coupons made from cryogenically mechanically alloyed powders compared to those of coupons made from non-mechanically alloyed samples.

## ACKNOWLEDGMENTS

I would first like to thank my parents, Earl and Patricia Martin, and sister, Rachel Martin, who always have offered their unwavering support in all of my endeavors. I would like to express my gratitude to my maternal grandparents, William and Susie Mowbray, who taught me the value of an education and continually took clippings of my accomplishments to lunches with friends (this one may be a little too long to read during lunch). I would also like to acknowledge my paternal grandparents, Frank and Virginia Martin, who are no longer here physically but will always be in my heart.

Many thanks go to Susette Sowers at Virginia Tech, for her assistance and friendship during my time in Blacksburg. I would also like to acknowledge Steve McCartney, who taught me more than I could ever have learned in a classroom about microscopy, and without knowing it, has exemplified the concept of taking one's soul to work. Of course, I could not have accomplished this without the guidance of Dr. Ron Kander, who served not only as my advisor for many years, but also as a trusted friend. Credit also goes to the late Dr. Richard Porter, who recruited me into the Materials Science and Engineering Department at NCSU, and believed I could earn a Ph.D. before I believed it myself.

I cannot express the gratitude I have for Scott Trenor, who has become my best friend. Thanks, Scott, not only for reading this 1,000 times and offering invaluable suggestions, but for encouraging me to be the best version of myself I can imagine.

And last but not least, I am very grateful to have shared the majority of my graduate school years with PJ (the cat), who, although he always seemed to lay on top of the most important papers and books (and sometimes the keyboard), has ensured that during these 5 ½ years, I kept my sense of wonder about the world. This has his paw prints all over it. Literally.

# TABLE OF CONTENTS

ABSTRACT.....	ii
ACKNOWLEDGMENTS .....	iii
TABLE OF CONTENTS.....	iv
LIST OF FIGURES .....	vii
LIST OF TABLES .....	xii
1. MOTIVATION .....	1
2. BACKGROUND .....	3
2.1 Thermodynamics of Polymer Blends .....	3
2.2 Mechanical Alloying Process .....	7
2.3 Mechanical Alloying Metals.....	8
2.3.1 Amorphization During MA of Metals.....	9
2.3.2 Physics and Modeling of MA Metals .....	10
2.4 Mechanically Milling/Alloying Polymers .....	11
2.4.1 Particle Size and Shape .....	14
2.4.2 Crystallinity and Crystal Structure .....	14
2.4.3 Molecular Weight.....	16
2.4.4 Bonding.....	18
2.4.5 Thermal Properties .....	19
2.4.6 Mechanical Properties .....	19
2.4.7 Scale of Mixing and Phase Morphology .....	20
3. PROJECT GOAL & THESIS STATEMENT .....	24
4. TECHNICAL APPROACH .....	25
4.1 System Selection Criteria.....	25
4.2 Imaging .....	26
4.3 Processing .....	29
4.4 Testing .....	30
4.5 Chapter Summary.....	31
5. MATERIALS AND METHODS .....	33
5.1 Materials .....	33
5.1.1 Polycarbonate (PC) .....	33
5.1.2 Poly(aryl ether ether ketone) (PEEK) .....	33
5.2 Mechanical Milling and Alloying .....	34
5.3 Injection Molding Processing .....	35

5.4 Characterization of Mechanically Milled and Mechanically Alloyed Powders .....	36
5.4.1 Particle Size Analysis .....	36
5.4.2 Thermogravimetric Analysis (TGA) .....	37
5.4.3 Gel Permeation Chromatography .....	38
5.4.4 Melt Rheology .....	38
5.4.5 Fourier Transform Infrared Spectroscopy .....	39
5.4.6 Wide Angle X-Ray Diffraction .....	39
5.4.7 Differential Scanning Calorimetry .....	40
5.4.8 Transmission Electron Microscopy .....	40
5.4.9 Scanning Transmission X-ray Microscopy .....	41
5.5 Characterization of Injection Molded Bars .....	41
5.5.1 Three-Point Bend Dynamic Mechanical Analysis .....	41
5.5.2 Three-Point Bend Quasi-Static Testing .....	42
5.5.3 Scanning Electron Microscopy .....	42
5.5.4 Transmission Electron Microscopy .....	43
5.5.5 Atomic Force Microscopy .....	43
5.5.6 Scanning Transmission X-ray Microscopy .....	43
 6. RESULTS FROM MECHANICALLY MILLED POWDERS .....	 44
6.1 Characterization of Powders .....	44
6.1.1 Particle Size Analysis .....	44
6.1.2 Thermogravimetric Analysis .....	46
6.1.3 Differential Scanning Calorimetry .....	47
6.1.4 Gel Permeation Chromatography .....	48
6.1.5 Melt Rheology .....	49
6.1.6 Fourier Transform Infrared Spectroscopy .....	50
6.1.7 Wide Angle X-Ray Diffraction .....	51
6.2 Imaging Mechanically Milled Powders .....	53
6.2.1 Field Emission Scanning Electron Microscopy .....	53
6.2.2 Transmission Electron Microscopy .....	54
 7. RESULTS FROM MIXED AND CONTROL SYSTEMS .....	 57
7.1 Characterization of Powders .....	57
7.1.1 Particle Size Analysis .....	57
7.1.2 Thermogravimetric Analysis .....	58
7.1.3 Differential Scanning Calorimetry .....	59
7.1.4 Transmission Electron Microscopy .....	60
7.2 Testing Molded Bars .....	62
7.2.1 Differential Scanning Calorimetry .....	62
7.2.2 Dynamic Mechanical Analysis .....	64
7.2.3 Quasi-Static Three-Point Bend Testing .....	70
7.3 Imaging Molded Bars .....	75
7.4 Imaging Tested Bars .....	76
7.4.1 Scanning Electron Microscopy .....	76
7.5 Testing Annealed Bars .....	78
7.5.1 Dynamic Mechanical Analysis .....	78
 8. RESULTS FROM THE CMA 10H SYSTEM .....	 81
8.1 Powder Characterization .....	81
8.1.1 Particle Size Analysis .....	81
8.1.2 Thermogravimetric Analysis .....	82
8.1.3 Differential Scanning Calorimetry .....	84
8.1.4 Fourier Transform Infrared Spectroscopy .....	84

8.1.5 Scanning Electron Microscopy .....	85
8.1.6 Transmission Electron Microscopy.....	86
8.1.7 Scanning Transmission X-Ray Microscopy.....	87
8.2 Testing Molded Bars .....	88
8.2.1 Dynamic Mechanical Analysis .....	88
8.2.2 Quasi-Static Three-Point Bend Testing.....	94
8.3 Imaging Molded Bars .....	99
8.3.1 Atomic Force Microscopy .....	99
8.3.2 Transmission Electron Microscopy.....	101
8.3.3 Scanning Transmission X-Ray Microscopy.....	102
8.4 Imaging Tested Bars.....	103
8.4.1 Scanning Electron Microscopy .....	103
8.5 Testing Annealed Bars .....	105
8.5.1 Dynamic Mechanical Analysis .....	105
8.5.2 Quasi-Static Three-Point Bend Testing.....	108
8.6 Imaging Annealed Bars .....	113
8.6.1 Atomic Force Microscopy .....	113
9. DISCUSSION AND CONCLUSIONS.....	117
9.1 Discussion of Results.....	117
9.1.1 Mechanical Testing Trends .....	117
9.1.2 Degradation Issues.....	124
9.1.3 Microstructural Issues.....	126
9.1.4 Molding Issues.....	128
9.2 Summary and Conclusions .....	133
9.3 Contribution and Impact.....	134
9.4 The Future of Mechanically Alloying Polymers .....	134
10. FUTURE WORK .....	140
10.1 Extensions of This Study .....	140
10.2 New Directions for Mechanically Alloying Polymers .....	141
10.2.1 Fundamental Demixing Studies .....	141
10.2.2 Novel Materials for Selective Laser Sintering.....	142
10.2.3 Reactive Systems.....	143
11. TECHNICAL ACKNOWLEDGMENTS .....	144
12. REFERENCES .....	145
VITA.....	147

## LIST OF FIGURES

<b>Figure 2.1:</b> Idealized schematic of Upper (a) and Lower (b) Critical Solution Temperatures. ....	6
<b>Figure 2.2:</b> Vibratory ball mill vial (B) and balls (A). ....	7
<b>Figure 2.3:</b> Powder particles trapped between colliding balls during high energy collision. Particles are fractured in Region B and then welded together in Region A. <sup>30</sup> .....	8
<b>Figure 2.4:</b> Idealized schematic of two-phase morphology resultant from the MA process. <sup>30</sup> .....	8
<b>Figure 2.5:</b> Particle configuration with increased milling time. <sup>25</sup> .....	8
<b>Figure 2.6:</b> $T_g$ vs. ambient milling time for polyisoprene. <sup>15</sup> .....	17
<b>Figure 2.7:</b> Change in $M_n$ (open symbols) and $M_w$ (solid symbols) with cryogenic MM (circles, solid lines) and ambient (triangles, dashed lines) MM for (a) high molecular weight PMMA (b) medium molecular weight PMMA (c) low molecular weight PMMA (d) PEP. <sup>8</sup> .....	17
<b>Figure 4.1:</b> X-ray micrograph of mechanically alloyed SR/PMMA with compatibilizer. The blend has been cryogenically mechanically milled for 10 hours, melt-pressed, then annealed for 30 minutes at 150°C. <sup>10</sup> .....	27
<b>Figure 4.2a-c:</b> TEM micrographs of mechanically alloyed a) metal-metal example, b) PEEK-Vectra B950 c) PEEK-LaRC-TPI. ....	28
<b>Figure 4.3a-c:</b> Micrographs of MA a) PEEK-LaRC-TPI particle, b) alumina-nylon-12 particle c) tyn-nylon12 particles. ....	29
<b>Figure 4.4:</b> AFM phase image of injection molded PEEK/PC bar (10 $\mu$ m x10 $\mu$ m cross-section). ....	29
<b>Figure 4.5:</b> Response of a viscoelastic material to applied stress or strain. <sup>51</sup> .....	31
<b>Table 5.1:</b> Selected material properties. $T_g$ and $T_m$ values were measured using DSC performed at 10°C/minute. ....	34
<b>Figure 5.2:</b> Photo of the ball mill used in this work. <sup>52</sup> .....	34
<b>Figure 5.3:</b> Schematic of the ball mill. <sup>52</sup> .....	35
<b>Figure 5.4:</b> Schematic of injection molded bar coupon. ....	36
<b>Figure 5.5:</b> Sample particle size histogram obtained from Horiba L-700 instrument. ....	37
<b>Figure 5.6:</b> TGA Unmilled PC raw data plot and derivative. ....	38
<b>Figure 5.7:</b> FTIR spectra of Unmilled PC. ....	39
<b>Figure 5.8:</b> Amorphous halo adjusted to unmilled PEEK WAXD raw data. ....	40
<b>Figure 5.9:</b> DMA data for Mixed sample injection molded at 360°C then annealed. ....	42
<b>Figure 6.1:</b> Particle size histogram for Unmilled PC. ....	45
<b>Figure 6.2:</b> Particle size histogram for PC MM 10h. ....	45
<b>Figure 6.3:</b> Particle size histogram for Unmilled PEEK. ....	45
<b>Figure 6.4:</b> Particle size histogram for PEEK CMM10h. ....	45
<b>Figure 6.5:</b> Mean particle size values for Unmilled and mechanically milled powders. ....	46
<b>Figure 6.6:</b> Typical Unmilled PC TGA raw data and derivative plot. ....	46
<b>Figure 6.7:</b> Typical Unmilled PEEK TGA raw data and derivative plot. ....	46
<b>Figure 6.8:</b> Degradation temperatures of mechanically milled PC. ....	47
<b>Figure 6.9:</b> Degradation temperatures of mechanically milled PEEK. ....	47
<b>Figure 6.10:</b> DSC curves performed at 10°C/minute for Unmilled PC, PC CMM, and PC AMM. Curves have been shifted vertically for comparison. ....	48
<b>Figure 6.11:</b> DSC curves performed at 10°C/minute for Unmilled PEEK, PEEK CMM, and PEEK AMM. Curves have been shifted vertically for comparison. ....	48
<b>Figure 6.12:</b> Melt rheology data obtained for Unmilled PEEK and CMM 10h PEEK. ....	49
<b>Figure 6.13:</b> FTIR spectra of Unmilled PEEK and PEEK CMM 10h samples. Spectra have been shifted vertically for comparison. ....	51
<b>Figure 6.14:</b> WAXD patterns for PEEK CMM samples milled for various times. Data have been shifted vertically for comparison. ....	51
<b>Figure 6.15:</b> Crystallinity index values calculated from WAXD data for PEEK CMM and PEEK AMM samples. ....	52

<b>Figure 6.16:</b> Field emission scanning electron micrographs of PC and PEEK before and after mechanical milling.....	53
<b>Figure 6.17:</b> TEM micrograph of Unmilled PC.....	54
<b>Figure 6.18:</b> TEM micrograph PC CMM 10h.....	54
<b>Figure 6.19:</b> TEM micrograph of Unmilled PEEK.....	55
<b>Figure 6.20:</b> TEM micrograph of PEEK CMM 10h.....	56
<b>Figure 7.1:</b> Particle size histogram for Control sample.....	57
<b>Figure 7.2:</b> Unmilled PC TGA raw data and derivative plot.....	58
<b>Figure 7.3:</b> Unmilled PEEK TGA raw data and derivative plot.....	58
<b>Figure 7.4:</b> Mixed sample TGA raw data and derivative plot.....	58
<b>Figure 7.5:</b> Degradation temperatures measured for Mixed and Control samples.....	59
<b>Figure 7.6:</b> DSC curves performed at 10°C/minute for Mixed and Control samples. Curves have been shifted vertically for comparison.....	60
<b>Figure 7.7:</b> TEM micrographs of Control powder particles.....	61
<b>Figure 7.8:</b> DSC curves performed at 10°C/minute for injection molded bars Control samples. Curves have been shifted vertically for comparison.....	63
<b>Figure 7.9:</b> Representative storage modulus curves for Mixed and Control samples injection molded at 350°C.....	64
<b>Figure 7.10:</b> Representative loss modulus curves for Mixed and Control samples injection molded at 350°C.....	64
<b>Figure 7.11:</b> Representative storage modulus curves for Mixed and Control samples injection molded at 360°C.....	65
<b>Figure 7.12:</b> Representative loss modulus curves for Mixed and Control samples injection molded at 360°C.....	65
<b>Figure 7.13:</b> Representative storage modulus curves for Mixed and Control samples injection molded at 370°C.....	66
<b>Figure 7.14:</b> Representative loss modulus curves for Mixed and Control samples injection molded at 370°C.....	66
<b>Figure 7.15:</b> Representative storage modulus curves for Control samples injection molded at 380°C.....	67
<b>Figure 7.16:</b> Representative loss modulus curves for Control samples injection molded at 380°C.....	67
<b>Figure 7.17:</b> Representative storage modulus curves for Mixed and Control samples injection molded at 390°C.....	67
<b>Figure 7.18:</b> Representative loss modulus curves for Mixed and Control samples injection molded at 390°C.....	67
<b>Figure 7.19:</b> Mixed inner samples Loss modulus curves.....	69
<b>Figure 7.20:</b> Mixed outer samples Loss modulus curves.....	69
<b>Figure 7.21:</b> Control inner samples Loss modulus curves.....	69
<b>Figure 7.22:</b> Control outer samples Loss modulus curves.....	69
<b>Figure 7.23:</b> 3-point bend data for replicate Mixed samples injection molded at 350°C.....	70
<b>Figure 7.24:</b> 3-point bend data for replicate Control samples injection molded at 350°C.....	70
<b>Figure 7.25:</b> 3-point bend data for replicate Mixed samples injection molded at 360°C.....	70
<b>Figure 7.26:</b> 3-point bend data for replicate Control samples injection molded at 360°C.....	70
<b>Figure 7.27:</b> 3-point bend data for replicate Mixed samples injection molded at 370°C.....	71
<b>Figure 7.28:</b> 3-point bend data for replicate Control samples injection molded at 370°C.....	71
<b>Figure 7.29:</b> 3-point bend data for replicate Mixed samples injection molded at 380°C.....	71
<b>Figure 7.30:</b> 3-point bend data for replicate Control samples injection molded at 380°C.....	71
<b>Figure 7.31:</b> 3-point bend data for replicate Mixed samples injection molded at 390°C.....	71
<b>Figure 7.32:</b> 3-point bend data for replicate Control samples injection molded at 390°C.....	71
<b>Figure 7.33:</b> Energy to failure values calculated from 3-point bend data. Arrows indicate samples where actual values are higher than measured values because the test was stopped at 40% strain.....	72
<b>Figure 7.34:</b> Failure strength values determined from 3-point bend data.....	73

<b>Figure 7.35:</b> Strain at failure values determined from 3-point bend data. Arrows indicate samples where actual values are higher than measured values because the test was stopped at 40% strain. ..	73
<b>Figure 7.36:</b> AFM images of injection molded Control bars. ....	75
<b>Figure 7.37:</b> SEM micrographs of Control fracture surfaces tested at 0.1mm/s. ....	77
<b>Figure 7.38:</b> Annealed (dotted) vs. as-molded (solid) Mixed samples, molded at 350°C. ....	78
<b>Figure 7.39:</b> Annealed (dotted) vs. as-molded (solid) Control samples, molded at 350°C. ....	78
<b>Figure 7.40:</b> Annealed (dotted) vs. as-molded (solid) Mixed samples, molded at 360°C. ....	79
<b>Figure 7.41:</b> Annealed (dotted) vs. as-molded (solid) Control samples, molded at 360°C. ....	79
<b>Figure 7.42:</b> Annealed (dotted) vs. as-molded (solid) Mixed samples, molded at 370°C. ....	79
<b>Figure 7.43:</b> Annealed (dotted) vs. as-molded (solid) Control samples, molded at 370°C. ....	79
<b>Figure 7.44:</b> Annealed (dotted) vs. as-molded (solid) Mixed samples, molded at 390°C. ....	79
<b>Figure 7.45:</b> Annealed (dotted) vs. as-molded (solid) Control samples, molded at 390°C. ....	79
<b>Figure 8.1:</b> Particle size histogram for Unmilled PC. ....	81
<b>Figure 8.2:</b> Particle size histogram for Unmilled PEEK. ....	81
<b>Figure 8.3:</b> Particle size histogram for CMA 10h sample. ....	81
<b>Figure 8.4:</b> .....	82
<b>Figure 8.5:</b> Effect of mechanical alloying time on degradation temperature of CMA and AMA samples. ....	83
<b>Figure 8.6:</b> Effect of number of milling balls (charge ratio) on degradation temperature of CMA samples. ....	83
<b>Figure 8.7:</b> DSC curves performed at 10°C/minute for the CMA 10h sample. Curves have been shifted vertically for comparison. ....	84
<b>Figure 8.8:</b> FTIR spectra of Unmilled and CMA 10h samples. Spectra have been shifted vertically for comparison. ....	85
<b>Figure 8.9:</b> FTIR spectra of cryogenically and ambiently mechanically alloyed samples. Spectra have been shifted vertically for comparison. ....	85
<b>Figure 8.10:</b> SEM micrographs of PC-PEEK CMA 10h particles. ....	85
<b>Figure 8.11:</b> Transmission electron micrographs of CMA 10h powder. ....	86
<b>Figure 8.12:</b> STXM image of CMA 10h powder collected at 286.2eV. ....	87
<b>Figure 8.13:</b> X-ray spectra of Unmilled PC and PEEK. ....	88
<b>Figure 8.14:</b> Storage Modulus data for CMA 10h samples injection molded at 350°C. ....	89
<b>Figure 8.15:</b> Storage Modulus data for CMA 10h samples injection molded at 360°C. ....	89
<b>Figure 8.16:</b> Storage Modulus data for CMA 10h samples injection molded at 370°C. ....	90
<b>Figure 8.17:</b> Storage Modulus data for CMA 10h samples injection molded at 380°C. ....	90
<b>Figure 8.18:</b> Storage Modulus data for CMA 10h samples injection molded at 390°C. ....	91
<b>Figure 8.19:</b> Loss Modulus data for CMA 10h samples injection molded at 350°C. ....	91
<b>Figure 8.20:</b> Loss Modulus data for CMA 10h samples injection molded at 360°C. ....	92
<b>Figure 8.21:</b> Loss Modulus data for CMA 10h samples injection molded at 370°C. ....	92
<b>Figure 8.22:</b> Loss Modulus data for CMA 10h samples injection molded at 380°C. ....	93
<b>Figure 8.23:</b> Loss Modulus data for CMA 10h samples injection molded at 390°C. ....	93
<b>Figure 8.24:</b> 3-point bend data for replicate bars molded at 350°C, tested at 0.1mm/sec. ....	95
<b>Figure 8.25:</b> 3-point bend data for replicate bars molded at 350°C, tested at 1.0mm/sec. ....	95
<b>Figure 8.26:</b> 3-point bend data for replicate bars molded at 360°C, tested at 0.1mm/sec. ....	95
<b>Figure 8.27:</b> 3-point bend data for replicate bars molded at 360°C, tested at 1.0mm/sec. ....	95
<b>Figure 8.28:</b> 3-point bend data for replicate bars molded at 370°C, tested at 0.1mm/sec. ....	95
<b>Figure 8.29:</b> 3-point bend data for replicate bars molded at 370°C, tested at 1.0mm/sec. ....	95
<b>Figure 8.30:</b> 3-point bend data for replicate bars molded at 380°C, tested at 0.1mm/sec. ....	96
<b>Figure 8.31:</b> 3-point bend data for replicate bars molded at 380°C, tested at 1.0mm/sec. ....	96
<b>Figure 8.32:</b> 3-point bend data for replicate bars molded at 390°C, tested at 0.1mm/sec. ....	96
<b>Figure 8.33:</b> 3-point bend data for replicate bars molded at 390°C, tested at 1.0mm/sec. ....	96

<b>Figure 8.34:</b> Energy to failure values for CMA 10h samples tested at 0.1mm/s and 1.0mm/s. Arrows indicate samples where actual values are higher than measured values because the test was stopped at 40% strain. ....	97
<b>Figure 8.35:</b> Energy to failure values for Control and CMA 10h samples tested at 0.1mm/s. Arrows indicate samples where actual values are higher than measured values because the test was stopped at 40% strain. ....	97
<b>Figure 8.36:</b> Failure strength values for CMA 10h samples tested at 0.1mm/s and 1.0mm/s. ....	98
<b>Figure 8.37:</b> Failure strength values for Control and CMA 10h samples tested at 0.1mm/s.....	98
<b>Figure 8.38:</b> Strain at failure values for CMA 10h samples tested at 0.1mm/s and 1.0mm/s. Arrows indicate samples where actual values are higher than measured values because the test was stopped at 40% strain. ....	98
<b>Figure 8.39:</b> Strain at failure values for Control and CMA 10h samples tested at 0.1mm/s. Arrows indicate samples where actual values are higher than measured values because the test was stopped at 40% strain. ....	98
<b>Figure 8.40:</b> AFM images of injection molded MA 10h bars .....	100
<b>Figure 8.41:</b> TEM micrograph showing cross-section of bar injection molded at 360°C.....	102
<b>Figure 8.42:</b> STXM images of CMA 10h bar molded at 380°C, taken at (a) 286.2 eV and (b) 287.2eV. ....	102
<b>Figure 8.43:</b> SEM micrographs of CMA 10h fracture surfaces tested at 0.1mm/s.....	104
<b>Figure 8.44:</b> Comparison plot of annealed vs. as-molded CMA 10h samples, molded at 350°C. ....	105
<b>Figure 8.45:</b> Comparison plot of annealed vs. as-molded CMA 10h samples, molded at 360°C. ....	106
<b>Figure 8.46:</b> Comparison plot of annealed vs. as-molded CMA 10h samples, molded at 370°C. ....	106
<b>Figure 8.47:</b> Comparison plot of annealed vs. as-molded CMA 10h samples, molded at 380°C. ....	107
<b>Figure 8.48:</b> Comparison plot of annealed vs. as-molded CMA 10h samples, molded at 390°C .....	107
<b>Figure 8.49:</b> 3-point bend data for bars molded at 350°C, then annealed. ....	108
<b>Figure 8.50:</b> 3-point bend data for bars molded at 360°C, then annealed. ....	109
<b>Figure 8.51:</b> 3-point bend data for bars molded at 370°C then annealed. ....	109
<b>Figure 8.52:</b> 3-point bend data for bars molded at 380°C then annealed. ....	110
<b>Figure 8.53:</b> 3-point bend data for bars molded at 390°C then annealed. ....	110
<b>Figure 8.54:</b> Energy to failure values for CMA 10h as-molded and CMA 10h annealed samples tested at 0.1mm/s. Arrows indicate samples where actual values are higher than measured values because the test was stopped at 40% strain.....	111
<b>Figure 8.55:</b> Failure strength values of CMA 10h as-molded and CMA 10h annealed samples tested at 0.1mm/s. ....	112
<b>Figure 8.56:</b> Strain at failure values of CMA 10h as-molded and CMA 10h annealed samples tested at 0.1mm/s. Arrows indicate samples where actual values are higher than measured values because the test was stopped at 40% strain.....	113
<b>Figure 8.57:</b> AFM phase images of annealed samples.....	114
<b>Figure 9.1:</b> Generalized schematic of expected property variation with injection molding temperature. ....	118
<b>Figure 9.2:</b> Property change with injection molding temperature for the Control system: (a) schematic of observed trend (b) energy to failure, (c) strain at failure and (d) failure strength. Arrows indicate samples where actual values are higher than measured values because the test was stopped at 40% strain. ....	119
<b>Figure 9.3:</b> Property change with injection molding temperature for CMA 10h samples: (a) schematic of trend observed (b) energy to failure, (c) strain at failure and (d) failure strength. Arrows indicate samples where actual values are higher than measured values because the test was stopped at 40% strain. ....	121
<b>Figure 9.4:</b> Property change with injection molding temperature for Mixed, Control, and CMA 10h samples (a) energy to failure, (b) strain at failure and (c) failure strength. Arrows indicate samples where actual values are higher than measured values because the test was stopped at 40% strain .....	123

**Figure 9.5:** Weight loss results for CMA 10h powders held at temperature for 5 minutes ..... 125

**Figure 9.6:** Annealed vs. as-molded CMA 10h samples, molded at 360°C. .... 129

**Figure 9.7:** Property change with injection molding temperature for CMA 10h annealed and CMA 10h as-molded samples (a) strain at failure, (b) energy to failure and (c) failure strength. Arrows indicate samples where actual values are higher than measured values because the test was stopped at 40% strain. .... 131

**Figure 9.8:** Property change with injection molding temperature for Mixed, CMA 10h as-molded, and CMA 10h annealed samples (a) strain at failure, (b) energy to failure and (c) failure strength. Arrows indicate samples where actual values are higher than measured values because the test was stopped at 40% strain. .... 132

**Figure 9.9:** Selective laser sintering equipment schematic..... 138

## LIST OF TABLES

Table 5.1: <b>Selected material properties. <math>T_g</math> and <math>T_m</math> values were measured using DSC performed at 10°C/minute.</b> .....	<b>34</b>
Table 5.2: Mechanical alloying conditions.....	35
Table 6.1: Particle size data for unmilled and mechanically milled materials. ....	45
Table 6.2: Transition values obtained from DSC data. ....	48
Table 6.3: GPC results for Unmilled and PC CMM 10h samples. ....	49
Table 6.4: Melt rheology data. ....	50
Table 7.1: Particle size data for Unmilled and Control materials. ....	57
Table 8.1: Particle size data for Unmilled and mechanically alloyed materials.....	82
Table 8.2: Summary of data. ....	116
Table 9.1: Microstructure comparison before and after injection molding for Control and CMA 10h samples.....	126

## 1. MOTIVATION

Mechanical alloying (MA) is a well established technique for processing metals that is capable of producing alloys with fine microstructures. Some researchers have also applied the mechanical alloying technique to blending polymers<sup>1,2,3,5,6,7,8,9</sup> in anticipation of improved polymer blend properties due to intimately mixed phases. Some studies<sup>1,5,6,7,8,10,11,12,13,14,42,43,44</sup> have briefly examined physical and mechanical properties obtained from mechanically milled or mechanically alloyed polymers. Other published results<sup>1,14,42,43</sup> have characterized the topology of mechanically milled or mechanically alloyed powders and used optical microscopy to image the microstructure, but were not able to differentiate phase domains. Recent studies<sup>2,3,8,9,10,11,12,13,15,40,48</sup> at North Carolina State University (NCSU) have successfully utilized scanning transmission X-ray microscopy to image mechanically alloyed polymer blends. These papers make up the only processing-microstructure studies of mechanically alloyed polymer systems published in the open literature to date. While the NCSU work has contributed significantly to the ability to image polymer microstructures obtained by MA and to determine the effects of subsequent heating, their work did not address post-mechanically alloyed processing at realistic conditions, nor did it investigate the effects of microstructure on mechanical properties. The existing body of work on mechanically alloying polymers fails to address the questions: Is mechanical alloying polymers just an academically interesting process? Does it have applications in niche markets such as recycling or selective laser sintering or does it have wide-spread industrial relevance for producing commercial blends?

A polymer blend can be defined as a “physical mixture of structurally different homo or copolymers”.<sup>16</sup> The objective of blending two or more polymers is generally to create novel materials with improved or unique properties and/or improved processing. In addition, blends are economical because they allow for quick modifications of performance with low capital investment compared to developing new polymers, and can lower the cost of using expensive resins by combining them with less expensive commodity resins.<sup>16</sup> Conventional polymer blending techniques such as solution and melt blending often require solvents, or compatibilizers to form blends because of the inherent immiscibility of most polymer combinations.

Some<sup>14</sup> have claimed that MA can produce blends in the solid state of thermodynamically immiscible polymers, giving rise to an infinite numbers of polymer-polymer blend permutations. However, this is not what would be expected if the intimately mixed blend was subjected to realistic subsequent processing involving heat and/or shear. This work, therefore, uses a model system to investigate the microstructure of mechanically alloyed powders as well as coupons that have been subsequently injection molded from these mechanically alloyed powders. The mechanical properties of the coupons were investigated and compared to those of non-mechanically alloyed blends in order to determine if the MA process is warranted in terms of mechanical property improvement.

## 2. BACKGROUND

### 2.1 Thermodynamics of Polymer Blends

Although an exhaustive review of the thermodynamics of polymer blends is beyond the scope of the present study, a brief introduction is presented here.

The miscibility of polymer blends depends on the delicate balance between entropic and enthalpic contributions to the Gibbs free energy of mixing ( $\Delta G_{mix}$ ).<sup>17,18,19</sup> For constant pressure and volume, the Gibbs free energy of mixing can be expressed as:

$$\Delta G_{mix} = \Delta H_{mix} - T\Delta S_{mix} \quad \text{Equation 2.1}$$

where  $\Delta H_{mix}$  is the enthalpy of mixing, T is the temperature in Kelvin, and  $\Delta S_{mix}$  is the entropy of mixing. In general, a negative  $\Delta G_{mix}$  term indicates that miscibility of phases is thermodynamically favorable (although the actual miscibility also depends on the kinetics of mixing). This means that for a positive  $\Delta H_{mix}$  term, the  $T\Delta S_{mix}$  term must override the enthalpic contribution. Unlike small molecule systems, however, both components of a polymer-polymer system possess high molecular weights, leading to a small number of moles of each polymer compared to those in metal alloys or other small molecule systems. The entropic term (which can be calculated using statistical methods) is usually negligible because of the small number of moles of the polymer chains and low self-diffusion coefficients, making the enthalpic contribution significant.<sup>18,19,20</sup> For polymer blend systems where specific interactions do not occur, the  $T\Delta S_{mix}$  term usually does not override the endothermic  $\Delta H_{mix}$  term and the polymers are consequently immiscible, exhibiting phase separation on a macroscopic scale.

Alternately, if enough specific interactions (such as hydrogen bonding or acid-base interactions) exist between chemical groups of the two polymer components to outweigh the dispersive contributions to the enthalpy of mixing, then the enthalpy of mixing term can be negative (exothermic). The negative enthalpy of mixing term causes the Gibbs free energy of mixing to be less than zero in spite of the weak contribution

from the combinatorial entropy term. These specific interactions are the reason why miscibility exists in most cases of miscible polymer-polymer systems,<sup>17,18,19</sup> and are represented in the Flory-Huggins theory as an interaction parameter,  $\chi$ . While no single, succinct theory exists to describe all the details of phase equilibria in polymers, the Flory-Huggins Theory,<sup>17,18,19,21</sup> independently proposed by Flory and Huggins, is a reasonable first-order approximation.

The combinatorial entropy of mixing of polymers A and B is defined from statistical thermodynamics as:

$$\Delta S_m = -k(N_A \ln v_A + N_B \ln v_B) \quad \text{Equation 2.2}$$

where  $k$  is Boltzman's constant,  $N_i$  is the number of moles of component  $i$  and  $v_i$  is the volume fraction of component  $i$ . The Flory-Huggins Theory gives the Gibbs free energy of mixing of polymers  $A$  and  $B$  as:

$$\Delta G_{mix} = kT(N_A \ln v_A + N_B \ln v_B + \chi N_A v_B) \quad \text{Equation 2.3}$$

These equations assume incompressibility (no volume change upon mixing). The parameter  $\chi$  present in Equation 2.3 measures interactions between repeat units when chains are placed in contact, can be defined as

$$\chi = \frac{\Delta H_{mix}}{kTN_A v_B} \quad \text{Equation 2.4}$$

By rearranging Equation 2.3, one arrives at an expression for partial molar free energy

$$\frac{\Delta G_{mix}}{kTV} = \frac{N_A \ln v_A}{V_A} + \frac{N_B \ln v_B}{V_B} + \frac{\chi v_A v_B}{V_A} \quad \text{Equation 2.5}$$

where  $V$  is the volume of the lattice cell and  $V_i$  is the molar volume of component  $i$ .

Using a lattice model, the lattice coordination number,  $z$  (between 6 and 12), can be used to approximate the basic equation for mixing of polymer blends<sup>17,21</sup>

$$\frac{\Delta G_{mix}}{kT} = \frac{V}{V_r} v_A v_B \chi \left( 1 - \frac{2}{z} \right) + N_c [v_1 \ln v_1 + v_2 \ln v_2] \quad \text{Equation 2.6}$$

where  $V$  is the sample volume,  $V_r$  is the volume of one cell,  $N_c$  is the number of molecules in 1 cubic centimeter. The first term on the right is the heat of mixing, and its sign depends on the value of the interaction parameter  $\chi$ . The entropic contribution (the second term on the right of Equation 2.6) is negative and very small because, unlike small molecules, the macromolecules must remain in connected configurations. As a result, the interaction coefficient  $\chi$  dominates the phase behavior of the polymer-polymer blend. Equation 2.6 can therefore be approximated as

$$\frac{\Delta G_{mix}}{kTV} \approx \chi v_A v_B \quad \text{Equation 2.7}$$

A characteristic feature of high molecular weight polymer-polymer systems is the existence of a lower critical solution temperature (LCST), meaning that for partially miscible polymers, phases separate as the temperature of the blend is raised above a characteristic temperature<sup>17,18,21</sup> (Figure 2.1a). The presence of a LCST is not accounted for in the theory proposed by Flory and Huggins, but later polymer phase equilibria theories improved on assumptions such as incompressibility made in the early theories. The use of equations of state (e.g. Flory *et al.*) and lattice fluid models (e.g. Sanchez *et al.* and Koningsveld *et al.*) account for both combinatorial molecular rearrangements (entropic) and specific interaction (enthalpic) contributions to  $\chi$ .<sup>17,18</sup>

In contrast to systems which exhibit a LCST, the presence of an upper critical solution temperature (UCST), predominates in small molecules and systems with solvents<sup>18</sup> but may also occur for short chain polymers<sup>17</sup> (Figure 2.1b). For materials that exhibit an UCST, the addition of thermal energy allows for increased “entropic” mixing. For most macromolecules, however, the mixing is driven by the enthalpic contribution to the Gibbs free energy as a result of specific interactions, which cause a volume change upon mixing. If the temperature of the system is increased, the entropic term in the Gibbs free energy of mixing

equation ( $T\Delta S_{mix}$ ) decreases the effect of the negative enthalpic term ( $\Delta H_{mix}$ ), and the total free energy of mixing increases. The free energy eventually becomes positive at the LCST, causing demixing to occur at a higher temperature (LCST) rather than a lower one (UCST). Even when a polymer blend is miscible or partially miscible, phase separation is therefore likely to occur upon heating. This separation may occur via one of two mechanisms: nucleation and growth, or spinodal decomposition. In nearly all polymer blend systems, the mechanism at work in phase separation is nucleation and growth.<sup>50</sup>

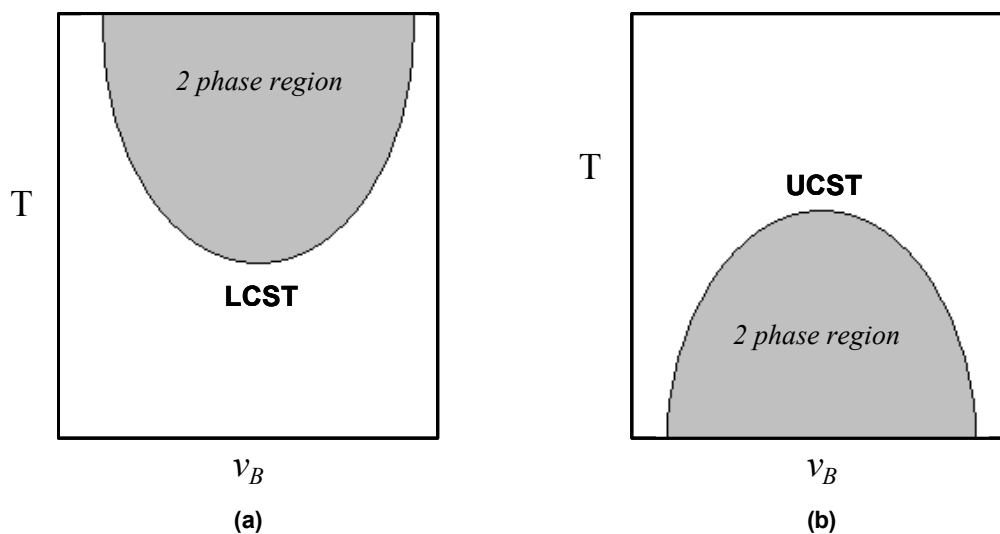


**Figure 2.1:** Idealized schematic of Upper (a) and Lower (b) Critical Solution Temperatures.

Most polymers are mutually immiscible or only partially miscible at best,<sup>17</sup> and therefore form two-phase systems when blended with one another. The inclusion of a compatibilizer (a third phase in which both phases of the blend are miscible) is often a practical necessity to promote partial miscibility between the polymer phases.<sup>22</sup> Compatibilizing agents are usually block or graft copolymers with segments that have chemistry similar to each of the blended components. These agents act as polymeric surfactants to reduce interfacial tension (promoting interfacial adhesion), thereby obtaining a finer dispersion and more uniform distribution of the dispersed phase.<sup>22</sup> In the case of mechanical alloying polymers, a non-equilibrium two-phase microstructure is formed. As these non-equilibrium microstructures are heated, it is expected that the phases will demix via a mechanism similar to Ostwald ripening, where the size of the coarsening phase is a function of time and temperature.

## 2.2 Mechanical Alloying Process

Mechanical milling (one component) and mechanical alloying (two or more components) are techniques originally developed in the late 1960's for the solid state processing of metals. Mechanical alloying is widely used in the metals industry for producing composite metal powders with fine microstructures.<sup>1</sup> According to traditional terminology, when two or more metals are mechanically alloyed, a new phase with a different composition is formed at the interface of the two initial phases. As applications for this technique expanded to blending polymers and producing coatings, the terminology was borrowed from the metals industry, with a different meaning. In the case of polymers and ceramics, the new meaning simply implied an improved dispersion of phases or the creation of a uniform coating without the formation of a new phase. Ball mills consisting of a motor, vial, and balls are used in the mechanical alloying process. Several different ball mill configurations exist, but two key parts are common to all configurations: the vial and balls (Figure 2.2).

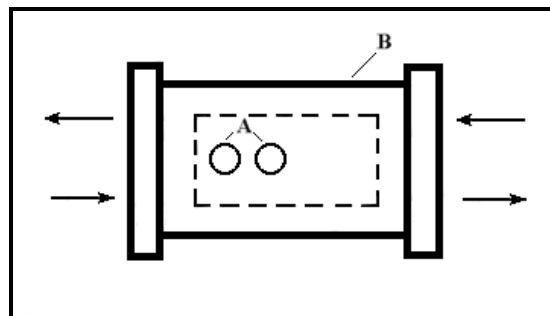


**Figure 2.2:** Vibratory ball mill vial (B) and balls (A).<sup>23</sup>

During mechanical alloying, powders are placed in the vial with two or more metallic or ceramic balls. The mill's motor vigorously shakes the vial, resulting in high energy impacts between the balls and the material. These impacts trap material between the balls, or a ball and the vial wall with each agitation (Figure 2.3). As milling occurs, the particles are repeatedly fractured, deformed, and fused together. This process of repeated fracturing and cold-welding causes a refinement in microstructure with milling time. The result is a two-phase lamellar microstructure (Figure 2.4) with an interlamellar distance dependent on total milling energy<sup>7</sup> (Figure 2.5).

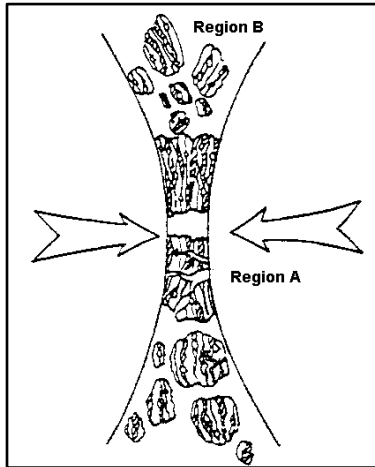


**Figure 2.3:** Powder particles trapped between colliding balls during high energy collision. Particles are fractured in Region B and then welded together in Region A.<sup>30</sup>

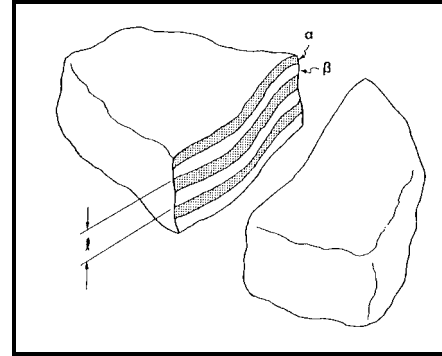


**Figure 2.4:** Idealized schematic of two-phase morphology resultant from the MA process.<sup>30</sup>

Total milling energy can be manipulated by changing the ratio of the total ball mass to powder mass (charge ratio), milling temperature, ball mill design, ratio of the diameter of the balls to the internal diameter of the cylindrical vial, or the milling time. The milling temperature can be critical because of its effect on both the material brittleness and thermally aided diffusion across interfaces.

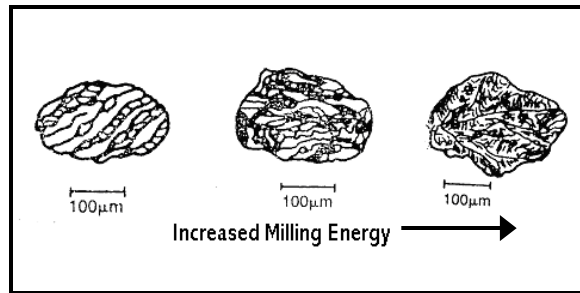


**Figure 2.5:** Particle configuration with increased milling time.<sup>25</sup>

### 2.3 Mechanical Alloying Metals

Mechanical alloying is well established as a metals processing technique. Mechanical alloying was developed as a method for producing oxide dispersion strengthened nickel-based superalloys for use in gas turbine engines. In addition to uses for dispersing a second phase in a matrix,<sup>24</sup> mechanical alloying has been used widely in the metals industry for other applications such as coatings, the production of amorphous

alloys and alloys which are normally immiscible, and the production of intermetallic alloys with appreciably different melting temperatures<sup>25</sup>. Mechanical alloying has also been used to produce metastable crystalline phases.<sup>26</sup>

The microstructural evolution of mechanically alloyed metals has been well characterized in the literature, although the fundamental mechanisms were not studied until the 1990's. During this time, the physics of mechanical alloying metals has been studied and attempts made to model such events as impact velocities, collision energies, temperature rises, and kinetics associated with the process.<sup>27</sup>

In studies using a commercial SPEX™ vibratory mill, mechanically alloying Ru and AlRu produced a narrow particle size distribution and broadened initially sharp X-ray diffraction peaks due to increase in internal strain.<sup>28</sup> These results are similar to those found in studies of mechanically alloyed polymers (Section 2.4). The mechanisms of deformation and amorphization are different for metals and polymers, however. Because deformation occurs via dislocation sliding in metals, Hellstern<sup>28</sup> attributes changes in the physical properties of the metal to decreasing crystalline sizes, and therefore, increased grain boundaries. No analogous theories have been postulated for polymers. Hellstern<sup>28</sup> concludes that milling time provides only an arbitrary scale for material property evaluation because it is dependent on not only the equipment type, but the size of the vial, number of balls, etc.

### **2.3.1 Amorphization During MA of Metals**

There are two main theories regarding how amorphization is achieved in MA metals.<sup>29</sup> The first theory involves the formation and subsequent rapid solidification of melt pools due to a temperature rise when balls collide, subsequently solidifying by rapid heat conduction. This theory states that boundaries between the particles would become amorphous if the solidification was fast enough. The entire powder would become amorphous through repeated fracture and cold welding because un-amorphized material would be brought into contact with each collision. It has been shown, however, that achievable velocities (approximately 4-6 m/s in a SPEX™ mill<sup>30</sup>) are two to three orders of magnitude below what would be necessary to accomplish amorphization in this way.<sup>29</sup> In contrast, one study<sup>31</sup> reported large temperature rises during MA though no

mechanism was offered. Other evidence which opposes the idea of large temperature rises during MA have been reported for other ductile systems.<sup>32</sup> Namely, mechanically alloyed amorphous alloys do not thermally re-crystallize during MA, indicating that local temperature rises do not reach the material's re-crystallization temperature in the bulk. Davis and coworkers<sup>32</sup> conclude that a temperature rise exceeding a material's melting temperature is not likely, but that a small temperature rise may enhance micro-diffusion.

The second theory regarding the amorphization of MA metals involves a solid state amorphization reaction (SSAR) taking place during MA.<sup>29</sup> Schwarz and Koch were the first to discover the solid state amorphization phenomenon in mechanically alloyed metals. They identify two conditions necessary for a SSAR to take place. First, one element must be an anomalously fast diffuser in the other, and, the two elements must have a large negative heat of mixing in the amorphous phase. The first criteria ensures a reasonable reaction rate, the second ensures a thermodynamic driving force. Diffusion therefore plays an important role in the SSAR of MA metals<sup>33</sup>, along with the presence of dislocations, point defects, and grain boundaries generated during milling by plastic deformation.<sup>29,33</sup> Furthermore, the dynamic nature of MA ensures that unalloyed material is continually brought to the surface,<sup>27</sup> and the high strains ensure short-cut diffusion paths through grain boundaries and other defects.<sup>33</sup>

Binary mixtures of metals have been formed for systems not meeting either of Schwarz and Koch's requirements (Ni-W for example).<sup>34</sup> The additional driving force for amorphization is believed to be a structural driving force, lying in the internal energy associated with nano-structure. When combined with the chemical driving force, amorphization may occur in metal systems not having a large negative heat of mixing. Amorphization occurring as a result of MA is generally observed in MA metal powders as broadened peaks in an X-ray diffraction pattern.<sup>29</sup>

### **2.3.2 Physics and Modeling of MA Metals**

The mechanics of collision events have been studied,<sup>30,35</sup> and equations have been developed for ductile metals regarding the change of particle shape, size, and hardness with mechanical milling and mechanical alloying. Computer programs have been developed in this effort<sup>36,37,38,39</sup> to optimize mill efficiency. The

computational approaches have been compared to experimental studies,<sup>35,36,37</sup> finding reasonable agreement. Both local and global modeling approaches have been developed. Local modeling involves the details of a single collision, and the parameters modeled are not specific to the type of mill device used. Global modeling is device specific and considers mill heterogeneities.

Local modeling studies have concluded that the greatest number of collisions are ball-powder-ball type<sup>37</sup> and the most effective impacts (in terms of evolution of microstructure) are those which are within a few degrees of head-on collisions. Calculations from Davis and coworkers indicate that in their model, a very small percentage of impacts (4-7%) result in an energy loss on the order of 1 J, which is that of a high velocity, head-on impact.<sup>32,38</sup> Most collisions result in an energy loss (transfer) between  $10^{-2}$  and  $10^{-3}$  J, even in a SPEX™ mill, which is considered a high energy mill;<sup>32</sup> therefore, only a small percentage of impacts are “effective” in the milling process.

## **2.4 Mechanically Milling/Alloying Polymers**

Mechanical alloying has been shown to create novel polymer blend morphologies with sub-micron phase domains in the powder state.<sup>2,3,8,9,10,11,12,13</sup> Given the success of using MA in the metals industry, it certainly seems to be an interesting process to consider for polymers. Pan and Shaw<sup>14</sup>, the first team to study mechanically alloyed polymers, asserted that “This mechanical alloying technique promises to provide the ability to make almost infinite permutations of polymeric alloys. This means that once the process is better understood, the properties of the alloy may be specifically designed resulting in a truly ‘Engineered Material’.” Subsequent studies on mechanically alloying polymers have for the most part, been driven by such claims. While forming polymer blends via MA has been proven possible, many questions remain unanswered regarding the efficacy of using this technique for polymer-polymer systems.

Originally, concerns about mechanical milling and alloying polymer-polymer systems were limited to worries of chain scission and degradation. Significant differences in molecular weight could arise from the polymer chains breaking during the milling process, creating free radicals which could then react with

oxygen, nitrogen, or other polymer molecules to produce grafts, cross-links, or further degradation.<sup>40</sup> In addition, the potential for locally elevated temperatures during milling could cause thermal degradation.<sup>14,4,40</sup> Mechanical alloying above the glass transition temperature of a polymer could be problematic due to high ductility, so polymers are often mechanically alloyed at cryogenic temperatures to ensure that they remain in the glassy state during the process.

Shaw is credited as the first researcher to apply the concept of mechanical milling (MM) or MA to polymers.<sup>41</sup> Pan and Shaw<sup>2,4,14,42,43</sup> studied cryogenically mechanically milled nylon polyamide (PA), ultra high molecular weight polyethylene (UHMWPE), mechanically alloyed PA-UHMWPE blends, mechanically alloyed PA-ABS (acrylonitrile-butadiene-styrene) powders, and a mechanically processed material produced by crushing. In their work, they characterized mechanically milled and alloyed powder microstructure, basic macrostructure, crystal structure, density, and some mechanical properties, concluding that responses of different polymeric materials to milling or alloying are very similar. These researchers utilized polarizing light microscopy to examine the mechanically alloyed microstructure of consolidated billets, and determined that the microstructure produced via MA is finer than that of a melt processed blend of the same materials.

A number of research groups have published work involving mechanical milling or alloying of polymers following Pan and Shaw's work: Ishida<sup>5</sup> (Japan), Font *et al.*<sup>44,45</sup> (Spain), Castricum *et al.*<sup>46</sup> (The Netherlands), Farrell, Kander and Aning at Virginia Tech<sup>7</sup>, and most recently, Smith *et al.*<sup>2,3,6,8,9,10,11,12,13,15,40</sup> at North Carolina State University. Thermal properties, crystallinity and structure, molecular weight, particle size and shape, bonding characteristics, and limited mechanical properties (mainly impact testing) have been investigated in these studies. Until NCSU published work in late 1999 and early 2000, no consideration was given to the phase morphology of MA powders or its retention of microstructure upon subsequent thermal processing.

Castricum<sup>46</sup> used a laboratory built vibratory ball mill and commercial planetary mill to process polyethylene glycol (PEG) and polystyrene (PS), and concluded that the planetary mill was more "powerful" (efficient) than the vibratory mill. More importantly, this was the first study where a complete phase transformation was reported for a pure polymer via mechanical milling. Font *et al.*<sup>44</sup> reported amorphization

of both sucrose and poly(ethylene terephthalate) (PET) by ball milling in a centrifugal mill for times up to 60 hours, and found that the amorphous material created via milling and amorphous material created via quenching from the melt exhibited different crystallization behavior, as shown by differential scanning calorimetry. Ishida<sup>5</sup> studied mechanically alloying poly(tetrafluoroethylene) (PTFE) with PE (normally incompatible polymers) in a vibratory ball mill in an argon atmosphere, as well as the individually milled components, concluding that MA causes amorphization and increased miscibility of these materials.

Farrell, Kander, and Aning<sup>7</sup> used a SPEX™ 8000 vibratory mill to mechanically mill and alloy polypropylene and Vectra B950 liquid crystalline polymer, and examined the resulting powders using thermal gravimetric analysis, optical microscopy, tensile testing, infrared spectroscopy, and X-ray diffraction. Other work at Virginia Tech<sup>47</sup> has proven the usefulness of MA for coating a ceramic (BaTiO<sub>3</sub>) with a polymer (LaRC-TPI) for composite grain boundary capacitor applications. This work published TEM images of MA ceramic-polymer powder particles prior to any post-processing or consolidation steps.

Researchers at North Carolina State University<sup>2,6,40</sup> initially focused on Vectra liquid crystalline polymer and two PET resins with initially different crystallinity levels, achieving a refined microstructure on a smaller scale than is achievable via conventional melt processing. Later studies<sup>3,8,9,48</sup> included poly(methyl methacrylate) (PMMA), poly(ethylene-*alt*-propylene) (PEP), and polyisoprene (synthetic rubber, SR). They published the first TEM micrograph of a mechanically alloyed polymer microstructure, imaging a cold-compacted disk of powder.<sup>6</sup> This was the first experimental evidence of the small size of phase domains achievable via MA since Pan and Shaw's use of light microscopy. More recent research at NCSU focused on imaging and tracking phase morphology of PMMA-SR or PMMA-PEP<sup>2,3,8,9,10,11,12,13,48</sup> materials using scanning transmission X-ray microscopy (STXM) and near-edge X-ray absorption fine structure (NEX-AFS) microscopy, which takes advantage of the differences in relative X-ray absorption of the two polymer components in the mechanically alloyed blend. Smith *et al.* were the first to apply STXM and NEX-AFS to imaging polymer-polymer MA blends; proving the application of this technique to be a major contribution to the field. This technique is useful for MA polymer-polymer systems; in particular, PMMA-PEP mechanically alloyed systems were examined in the powder state, compacted disks, and melt-pressed films as a function

of MA time, annealing temperature and time. Researchers at NCSU were also the first to use a copolymer as a compatibilizer to achieve a finer microstructure and to promote limited compatibilization during post-processing.<sup>10</sup>

Other work<sup>48</sup> has shown the efficacy of mechanically alloying polymers for recycling tires. PMMA and PET were each mechanically alloyed with tire scrap, and the microstructure was characterized with STXM and NEX-AFS. Sub-micron dispersions of tire material within PET and PMMA were achieved.

#### **2.4.1 Particle Size and Shape**

Mechanical milling has been shown to quickly reduce and narrow overall particle size distributions compared to original particle size distributions and those obtained from other quick crushing techniques.<sup>6,14</sup> Polymers that are cryogenically mechanically milled tend to show rapid reductions in particle size initially, then a continued reduction at a much slower rate.<sup>14</sup> When polymers are mechanically milled at ambient temperature, however, there can be an initial increase in average particle size as flake-like agglomerates form, and a reduction in size at longer milling times occurs as fracture competes with cold welding.<sup>6</sup> The final topology of MM polymers has been imaged using SEM in several studies<sup>1,4, 14,43,43</sup> and appear very similar for different materials, with only the size differing. The particle shape may also be related to other properties. For example, Balik *et al.* reported that the initial flattening of particles evident from particle topology images lead to stress induced crystallization in PET.<sup>6</sup>

#### **2.4.2 Crystallinity and Crystal Structure**

Several studies have reported that MM and MA cause amorphization (either complete amorphization or reduction in crystallinity) of polymers. These studies prove that MM and MA of polymers, like metals, have the potential to produce amorphous polymer powders although it is assumed that the underlying mechanisms are different<sup>5</sup>. Common techniques for investigating the amount of crystallinity present in polymers and traditional polymer blends have also proved to be useful tools for studying MM and MA polymers. Differential scanning calorimetry (DSC), wide angle X-ray diffraction (WAXD) and C<sup>13</sup> solid state nuclear magnetic resonance have been used to compare the percent crystallinity and crystal structure before

and after mechanical milling or alloying. Some studies have determined that both the amount of crystallinity and the crystal structure change with milling.<sup>4,14,41</sup> Other research has concluded that no change in the unit cell occurred although percent crystallinity reduction took place during milling.<sup>42,44</sup> Castricum reported a phase transformation (from orthorhombic to monoclinic) for PE.<sup>46</sup> Studies that employed WAXD to verify changes in crystallinity have indicated that initially sharp diffraction peaks generally broaden as a result of MM. The broadening of diffraction peaks could be due to either lattice strains induced during milling or a decrease in crystallite size.<sup>5</sup> Researchers at NCSU found that for the low-crystallinity PET used in their work, the crystallinity increased with MM time. Since the melting temperature of PET (190°C) is unlikely to be exceeded in the bulk during cryogenic milling, the increase in crystallinity may be attributed to a driving force other than thermal energy.<sup>40</sup> The crystallinity value of the initially highly-crystalline PET decreased with MM time (all occurring within the first hour of milling).<sup>6</sup> The explanation in this case is unique to the structure of PET, which contains stacked phenyl sheets. After short MM times, order within the phenyl sheets is believed to be lost, and after long MM times, these sheets are thought to become rotationally disoriented about the chain axis.<sup>6,15,40</sup> With extended milling, an “oriented amorphous” phase,<sup>15</sup> resulting from locally aligned but rotationally disordered chains form in this system.<sup>40</sup> The authors of these studies have determined that crystallinity values obtained from WAXD were not at all consistent with DSC results<sup>15</sup> and they attribute this discrepancy to crystallization of MM samples upon heating in the DSC, which is not accurately accounted for by subtracting the heat of crystallization from the enthalpy of fusion. Presumably, the crystal imperfection increases with mechanically milling or alloying, and non-equilibrium stress states exist in the mechanically processed material. Enthalpic relaxations may occur when the material is heated in a DSC experiment due to trapped residual stresses. By comparing DSC and WAXD crystallization results for these highly oriented samples, the authors conclude that DSC data alone can produce misleading results and erroneous conclusions for mechanically milled samples.

### 2.4.3 Molecular Weight

Pan and Shaw reported an increase in molecular weight from 17,000 to 18,000 g/mole with mechanically milled of ABS;<sup>14</sup> no explanation was given, and the authors did not state whether they believed this difference was significant. Balik and coworkers determined that milling temperature affected the molecular weight of mechanically milled PET; the molecular weight of PET decreased by 13.8% and 46.7% when mechanically milled for 16 hours cryogenically and ambiently, respectively.<sup>6,49</sup> Marked decreases in number average molecular weight ( $M_n$ ) and weight average molecular weight ( $M_w$ ) were also found with increased MM time for PMMA, with a greater change resulting from ambient milling compared to cryogenic milling.<sup>15</sup> These results indicate that MM did not cause cross-linking in these materials.<sup>6,15</sup> The difficulty in performing GPC analysis for some solvent-resistant polymers has led several researchers to rely on changes in glass transition temperature as indicators of changes in molecular weight of MM polymers.

Balik's group used a change in glass transition temperature ( $\Delta T_g$ ) between milled and unmilled polyisoprene as an indicator of change in molecular weight. When the  $\Delta T_g$  of polyisoprene is plotted vs. milling time (Figure 2.6), an initial 8°C increase in  $T_g$  is followed by a decrease in  $T_g$  after two hours of milling. The initial decrease is followed by a very small difference in  $\Delta T_g$  at intermediate milling times before it increases slightly again at longer milling. The authors conclude that polyisoprene undergoes chemical cross-linking during cryogenic milling. Their finding was used to support the theory that milling is a dynamic competition between chains breaking (decrease in molecular weight) and cross-linking (for cross-linkable polymers) under the non-equilibrium conditions of MM.<sup>15</sup> When the authors plotted  $\Delta T_g$  for ambiently milled PMMA, they found a monotonic decrease indicating that chain scission occurs during ambient MM of this polymer.

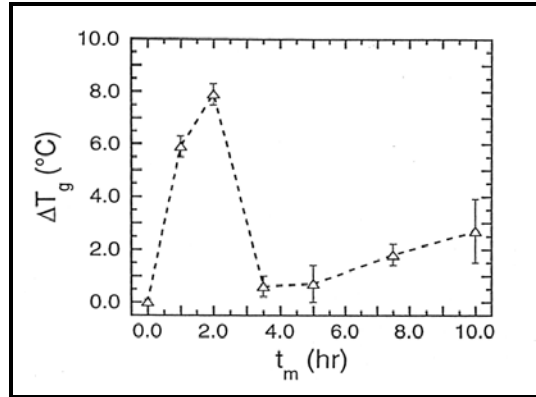


**Figure 2.6:**  $T_g$  vs. ambient milling time for polyisoprene.<sup>15</sup>

Another paper from the same group<sup>8</sup> examined the effects of mechanical milling on PMMA, polyisoprene, and PEP homopolymers. The authors reported significant reductions in both the number and weight average molecular weights (measured by gel permeation chromatography) for each of these materials mechanically milled at both cryogenic and ambient temperatures (Figure 2.7). Some samples exhibited an order of magnitude drop in number average molecular weight with an hour of milling under their conditions. An increase in the polydispersity index (PDI) of these materials followed by decrease in PDI, attributed to the preferential breaking of long chains at short milling times.<sup>8</sup>

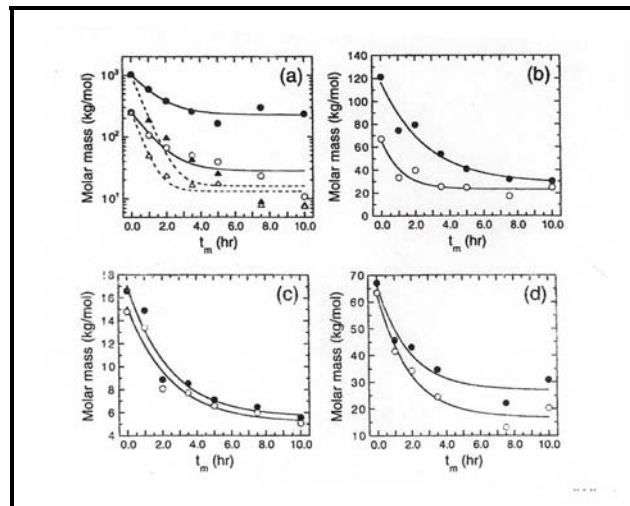


**Figure 2.7:** Change in  $M_n$  (open symbols) and  $M_w$  (solid symbols) with cryogenic MM (circles, solid lines) and ambient (triangles, dashed lines) MM for (a) high molecular weight PMMA (b) medium molecular weight PMMA (c) low molecular weight PMMA (d) PEP.<sup>8</sup>

Castricum *et al.*,<sup>46</sup> on the other hand, found no significant differences in  $M_w$ ,  $M_n$ , or z-average molecular weights and did not find any change in PDI of MM poly(ethylene glycol) or PE. The absence of any broadening or average molecular weight value changes led to the conclusion that no chemical changes took place, and that the energy imparted by MM was insufficient to break carbon-carbon bonds.

#### 2.4.4 Bonding

Investigations into the bonding relationships present in mechanically processed powders have been driven by the possibility of chain scission during MM or MA. Chain scission could create free radicals which have the potential to form new bonds, either by reacting with nitrogen or oxygen in the air and creating new functional groups, or by bonding with other fractured dissimilar polymers, creating graft or block copolymers.<sup>5,6</sup> Currently, the mechanisms at operation in MM or MA polymer are not clear, and some researchers claim that the complexity of the mechanisms may be due to combinations of chemical reactions and physical changes that lead to metastable microstructures<sup>6</sup>. No changes in peak positions of Fourier Transform Infrared Spectroscopy (FTIR) spectra have been reported, however.<sup>5,6,7</sup> Despite contradictory reports, most researchers conclude that mechanical milling and alloying leads to stronger interfaces, whether by physical interpenetrations, or by chemical bonding. Pan and Shaw were the first to consolidate billets of a mechanically milled polymer below its melting temperature, consolidating PA at 160° below melt (with 60 MPa of pressure for 48 hours).<sup>4,14</sup> These authors attribute the low temperature consolidation to particle surface reactivity, enabling bonding to occur with less thermal energy. This phenomenon is not exclusive to MM, however – the same consolidation was possible with quick-crushed material. They believe that active reaction sites allow both chemical bonding and physical interpenetrations<sup>1,4,14</sup> which, when combined with the large number of interfaces created by MM, create a higher bonding strength. Their argument of increased reactivity is questionable since any free radicals or reactive sites would disappear within a very short time. They present no evidence for their theory, and minimal molecular weight analysis. It is more likely that increases in strength are due to increased surface area created by MM and consequent faster diffusion. “Bonding strength” in Pan and Shaw’s work was characterized by formic acid dissolution tests, where MM

material took 45% longer to dissolve than non-milled material.<sup>4,14</sup> The concept of internally stored energy arising from the MM or MA process has also been suggested to be a cause of the lower thermal activation energies which apparently occur due to MM.<sup>1,57</sup>

#### **2.4.5 Thermal Properties**

Changes in thermal properties cannot necessarily be separated from changes in molecular weight (Section 2.4.3), but often can be more easily measured. Balik *et al.*<sup>6</sup> has indicated that the melting temperature of PET increases slightly after mechanical milling at ambient temperature, but not after cryogenic milling. The crystallization temperature of PET decreased by 30°C after some milling (2 hours for low crystallinity PET and 20 minutes for high crystallinity PET). The  $\Delta T_g$  between unmilled polyisoprene and cryogenically MM polyisoprene has been studied and used to indicate changes in molecular weight.

Some researchers report decreases in the degradation temperature of mechanically milled and alloyed polymers,<sup>5</sup> while others report no significant change due to mechanical processing.<sup>7</sup> Accelerated degradation of one phase in the presence of another (PP in the presence of a liquid crystalline polymer) has been attributed to the MA process.<sup>7</sup> Based on a reduction in the start of decomposition, Ishida suggests that the miscibility of PTFE and PE begins to occur after 40 hours of milling.<sup>5</sup>

Differences in the thermal crystallization behavior of amorphous material formed by MM and that formed by a post-heating quench have been found by Font and coworkers for sucrose and PET.<sup>44</sup> This study found that quenched amorphous sucrose does not thermally recrystallize, unlike amorphous sucrose formed via MM. The amorphous PET formed via MM exhibited a lower glass transition temperature and higher crystallization temperature.

#### **2.4.6 Mechanical Properties**

Mechanical property evaluations of consolidated billets by Pan and Shaw have indicated higher strength<sup>1,4,14,42,43</sup> as well as ductility<sup>1,4,14</sup> and impact energy<sup>4,14</sup> than thermally processed or mechanically cut material, with the properties dependent on milling and consolidating parameters. Pan and Shaw concluded that MA produces stronger material but offered no clear explanation why; they assumed the enhanced

mechanical properties were due to physical interpenetrations on the molecular level between amorphous and crystalline phases.<sup>4</sup> The authors found that the hardness of mechanically milled PA increased by approximately 13% and mechanically milled PE increased by nearly 32% over thermally processed materials. Similarly, the hardness of mechanically alloyed PE-PA increased 34% compared to melt blended material and was equal to 120% of the expected value from the rule of mixtures (ROM).<sup>42</sup> Farrell reported promising results from tensile tests of melt-pressed films of mechanically alloyed PP-Vectra compared to an unmilled mixture.<sup>7</sup> Balik and coworkers found an increase in hardness compared to thermally processed material and the rule of mixtures prediction.<sup>6</sup> The improvement in mechanical properties is believed to be due to the decrease in phase domain size and increase in physical interpenetrations, similar to a decrease in grain size for metals, a decrease in spherulite size for crystalline polymers, or finer dispersions in a composite material. Other work, however, has reported a drastic decrease in the impact strength of consolidated billets accompanying a proportional reduction in molecular weight with mechanical alloying<sup>8</sup>. This reduction in impact strength is lessened, however, by the incorporation of small amounts of copolymer compatibilizer during the MA process,<sup>10</sup> which simultaneously achieved a finer microstructure compared to blends processed without the copolymer addition.

#### **2.4.7 Scale of Mixing and Phase Morphology**

Pan and Shaw<sup>14,4</sup> used scanning electron microscopy (SEM) to show the extremely fine structure of compacted disks, and used optical microscopy to qualitatively compare the size of thermally blended microstructure to that formed via MA. The difference was readily visible in the micrographs. The authors further imaged mechanically alloyed powder particles using SEM, and noticed that each particle appeared to be a conglomeration of sub-particles (a fact reinforced by particle size data), noting that the individual phases could not be distinguished using this technique.<sup>14,42,43</sup> Farrell qualitatively compared the microstructure of mechanically alloyed polymer to an unmilled mixture of powder components. In this case, the two mixtures of PP and Vectra were hot pressed and then cryogenically fractured. Due to the fibrillar nature of the Vectra material, both blends resembled a fiber-reinforced composite. The unmilled mix resembled a fiber reinforced

composite with very little interfacial bonding between phases (indicated by fiber pullout).<sup>7</sup> The mechanically alloyed sample, on the other hand, displayed considerable matrix tearing. The mechanically alloyed blend exhibited a homogeneous distribution of phases. Balik *et al.*<sup>6</sup> compacted disks of mechanically alloyed PET-Vectra and compared the microstructure to that of a thermally processed film using transmission electron microscopy. Although these micrographs revealed a significant difference in the scale of mixing achieved by MA vs. thermal processing, no consideration was given in this study to potential phase demixing upon heating of the mechanically alloyed microstructure. In addition, the phase domains of this compacted disk may be different than that of the actual mechanically alloyed powder.<sup>6</sup>

Very recent papers published by Smith *et al.*<sup>2,3,8,9,10,11,12,13,48</sup> from North Carolina State University have shown successful imaging of MA polymers using scanning transmission X-ray microscopy in conjunction with near edge X-ray absorption fine structure (NEX-AFS) microscopy. Smith *et al.* were the first to employ this technique to image mechanically alloyed polymers.<sup>2</sup> They examined the microstructure of MA Vectra and PET blends,<sup>2</sup> as well as blends of PMMA with SR and PEP.<sup>2,3,8,9,10,11,12,13</sup>

The first system explored by this group consisted of Vectra liquid crystalline polymer and PET, in which they imaged the extremely fine dispersions of Vectra in PET (200-500nm in diameter) in mechanically alloyed powder blends.<sup>6</sup> Another paper<sup>2</sup> examined the phase demixing upon heating with no shear in mechanically alloyed blends of the same materials. The authors observed more phase demixing with increased annealing temperature. Virtually no demixing took place when the powders were annealed close to the low temperature component's glass transition temperature. Other parameters that were identified to influence phase morphology included Vectra concentration and milling temperature. It was concluded that despite demixing, a large degree of the mixing achieved via MA could be preserved even after heating in the melt.

Other papers<sup>2,3,9,10,11,12,13,48</sup> by the same group utilize the STXM and NEX-AFS techniques to image PMMA-PI and PMMA-PEP mechanically alloyed powders. Some of these papers<sup>2,3,10,11,12</sup> also examined the de-mixing of phases upon post-processing. This is an important issue since these systems exhibit an upper critical solution temperature, and the inherent thermodynamic incompatibility of the polymers will become

apparent as the mechanically alloyed blend is heated. Smith *et al.* reported<sup>11,13</sup> substantial “coarsening” (demixing) in PEP-PMMA blend films molded in a hot press at relatively short annealing times (5 minutes). This system was highly immiscible and mobile above the  $T_g$  of PMMA. Using STXM, they were able to track phase domain size and shape with milling time and post-processing temperature and time. The authors found that as mechanical alloying time increased for PMMA-PEP blends, the size of phase domains in MA powders decreased, as expected. While the mechanically alloyed phases are highly dispersed in the powder form, annealed samples show increasing domain sizes with additional annealing time at constant temperature so that the mechanically alloyed microstructure is at least partially lost. Increased phase domain sizes were also found for increased annealing temperature at constant annealing time. Based on these observations and gel permeation chromatography molecular weight data, the authors concluded<sup>9</sup> that for the PMMA-PEP system, no milling-induced inter-chain coupling occurred; MA simply reduced the scale of mixing by physical reduction rather than chemical means. However, for the SR-PMMA<sup>9</sup> system, cross-linking during the mechanical alloying process greatly influences the morphology of the blend. The cross-linking causes the SR chains to become increasingly constrained as the mechanical alloying process proceeds, allowing for more retention of intimately mixed microstructure upon annealing. In fact, they reported that for annealing times longer than 5 minutes, blends actually exhibited negligible differences in morphology, resulting in novel microstructures for those blends where macromolecular interactions occur during the MA process.

Another important aspect of Smith’s study involves the use of a solid- state compatibilizer to achieve a finer microstructure in the PMMA-SR binary blend. This work proved the usefulness of a solid state compatibilizer poly(methyl methacrylate-*b*-isoprene) diblock copolymer<sup>10</sup> for stabilizing and refining mechanically alloyed polymer-polymer systems. At high concentrations of the copolymer, the microstructure could be somewhat retained during post-processing in the melt. While a distribution of the copolymer along the phase domain interface would be most useful in terms of mechanical property improvement, MA seems to merely disperse the copolymer well enough to allow for a reduction in phase demixing and a corresponding enhancement of mechanical properties.

Combined with mechanical property data, microstructural information can be correlated to processing conditions for a more complete understanding of the process-structure-property relationships. From this, a judgment can be made regarding whether MA is able to produce a microstructure which can be retained in a useful part geometry and provide improved properties.

### 3. PROJECT GOAL & THESIS STATEMENT

Much of the published literature regarding mechanically alloying polymers has been based on an anticipated improvement in mechanical properties resulting from intimate mixing achieved in the powder state. Only a few studies, however, have investigated the microstructure of mechanically alloyed polymers that have been post-processed. Of these studies, only two have processed mechanically alloyed powders above their glass transition temperature; both obtained limited mechanical data. No mechanical property data exist in the published literature for a mechanically alloyed polymer-polymer system that has been realistically post-processed using both temperature and shear.

This study poses the following three questions for a model system:

1. Is the microstructure created via mechanical alloying retained when mechanically alloyed powders are post-processed into a testable coupon?
2. Does mechanical alloying cause changes in measured mechanical properties compared to a similar non-mechanically alloyed system?
3. Is the extra processing step of mechanical alloying warranted for the model system?

Furthermore, this work aims to develop an understanding of why differences (if any) exist between the studied systems so that a direction for fruitful future work in this area can be proposed. Given the differences in the thermodynamics of mixing between small molecules and macromolecules, it is anticipated that the mechanically alloyed powder microstructure will greatly demix upon traditional post-processing, yielding little or no improvement in measured mechanical properties over non-mechanically alloyed systems.

## 4. TECHNICAL APPROACH

This work asks several questions about the effects of mechanical milling and mechanical alloying on polymers: 1) How does MM affect the properties of an individual polymer? 2) Do the microstructure and properties of the powders or injection molded parts change with MA compared to control samples? 3) Does demixing occur upon post-MA injection molding, and if so, how does it affect properties?

If a demonstration system is carefully chosen, all of these questions can be addressed for the model system. For example, questions regarding microstructure can be answered directly by imaging. The selection of a model system and an appropriate imaging technique is an iterative process, as the imaging technique used may depend on the system, and the system chosen may depend on the availability of appropriate imaging equipment. The general characteristics of a model system for such a study are outlined in the following sections.

### 4.1 System Selection Criteria

There are a virtually unlimited number of polymer systems that could be considered for a mechanical alloying study. The model system chosen for this study, however, should have the following characteristics:

- ***Relatively low molecular weight:*** A low molecular weight system is desirable to ensure that the time scales for molecular motion are relatively short, resulting in a system in which, if demixing occurs, it does so relatively quickly so that it can be examined on realistic timescales in the laboratory.
- ***Attractive physical property combination:*** As with any polymer blend system, the individual materials selected should each have desirable properties that can contribute to the properties of the blended system and which lead to property differences that are measurable in the laboratory.
- ***Easily processed after MA:*** It is desirable to limit the post-MA processing temperature window to ensure a finite test matrix for studying processing and demixing.
- ***Easily characterized:*** Perhaps the most important and difficult criteria, a model system should be characterized by readily available methods. This could mean that the materials have: different electron

densities, solvent resistance, crystallinity characteristics, hardness, or modulus values. Relative differences in electron densities of the two phases mean that a blend can be examined using scanning electron microscopy (SEM) or transmission electron microscopy (TEM), which provides higher resolution than SEM. The same effect is also achieved if one phase can be stained with a small molecule such as RuO<sub>4</sub>, changing the electron density of that phase. If one phase is more easily soluble than another, then a solvent could potentially be used to etch away one phase for a relief image. A microtomed and etched surface could be examined using atomic force microscopy (AFM), TEM (which detects differences in thickness as well as electron density) or SEM (useful for imaging topology). Differences in inherent hardness or modulus values may produce contrast between the two materials in the phase image in tapping mode AFM. The same is true for different crystallinity characteristics: an amorphous material may exhibit a different AFM phase image than a semi-crystalline one.

## 4.2 Imaging

The goal of this work is primarily to develop a process whereby the efficacy of the MA process for producing not only blended powders, but also blended post-processed coupons can be determined and understood. In order to do this, it is necessary to be able to image the system in question. Appropriate imaging techniques vary with the particular system of interest. For some systems, identifying a technique that will detect phase differences on the sub-micron level can be extremely time consuming. The successful use of scanning transmission X-ray microscopy (STXM) in conjunction with near-edge X-ray absorption fine structure (NEX-AFS) microscopy has therefore been a major contribution to the field, as it can be used to differentiate phases of virtually any two polymers. This equipment, however, has limited availability. Other techniques attempted in this work, along with their advantages and disadvantages, are discussed below.

Scanning transmission X-ray microscopy has been utilized to image mechanically alloyed blends of PMMA-SR, PMMA-compatibilizer-SR, and PMMA-PEP<sup>2,3,8,9,10,12,13</sup> in both powder and film form. Annealed films were also imaged, with phase separation visible. Each chemical structure has a X-ray “fingerprint”

which can be exploited by carefully selecting a photon energy so that one polymer phase appears dark relative to the other when the sample is raster-scanned to create an absorbance map, which leads to unambiguous differentiation between phases. Figure 4.1 is one such STXM absorbance map of a PMMA-compatible SR melt pressed film.

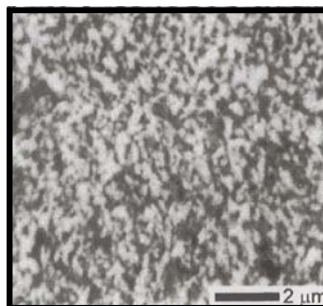


**Figure 4.1:** X-ray micrograph of mechanically alloyed SR/PMMA with compatibilizer. The blend has been cryogenically mechanically milled for 10 hours, melt-pressed, then annealed for 30 minutes at 150°C.<sup>10</sup>

Alternatively, the STXM X-ray beam can be focused on one position within the sample and the photon energy incrementally changed over a period of several hours, allowing a “stack” to be created, consisting of a series of absorbance maps at each programmed X-ray energy. These data can then be utilized to obtain an optical density spectrum. In addition, in either mode, the STXM can be used to identify individual phases within the sample by recording an X-ray spectra of a particular area of interest.

Metal-polymer, ceramic-polymer, and metal-metal systems are relatively easy to image with other methods because their inherent differences in electron energy densities create contrast when viewed with TEM. A TEM micrograph of a mechanically alloyed metal-metal system is shown in Figure 4.2a. Likewise, a polymer-polymer system that can be preferentially stained can be imaged using TEM (Figure 4.2b), but artifacts from the microtoming process such as chatter may be superimposed on the inherent microstructure (Figure 4.2c). If one polymer doesn’t stain well, it can be very difficult to differentiate the two phases using TEM.

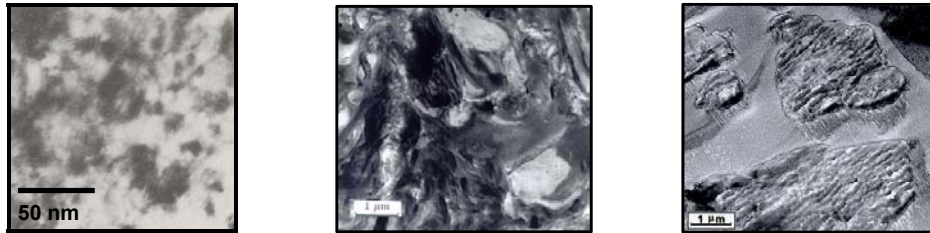


**Figure 4.2a-c:** TEM micrographs of mechanically alloyed a) metal-metal example, b) PEEK-Vectra B950 c) PEEK-LaRC-TPI.

Scanning electron microscopy or field emission scanning electron microscopy (FESEM) is useful for imaging the topology of mechanically alloyed powders. The X-ray photoelectric spectroscopy (XPS) capabilities can perform elemental analysis on mechanically alloyed powders. If one phase has an elemental “tag,” XPS can be used to determine the elements present in a powder particle, and it can be determined if both phases are present in a mechanically alloyed powder particle. However, the spatial resolution of mechanically alloyed particles cannot be distinguished if sub-micron phases exist. The use of FESEM for mechanically alloyed polymers does have applications, however; it may be useful to determine that a particle consists of two phases, even if the sizes can't be resolved. FESEM is very useful for polymer-metal and polymer-ceramic systems, since the phases have inherently different electron densities and show up differently in backscatter mode. Applications for FESEM are demonstrated in Figure 4.3: Figure 4.3a is a micrograph of a mechanically alloyed polymer-polymer particle, where topology is apparent, but no distinction between phases can be made. Figure 4.3b is a micrograph of a mechanically alloyed polymer-ceramic system, where two phases can be differentiated. Figure 4.3c shows cross sections of particles from a mechanically alloyed metal-polymer system (bright areas are tin particles and darker particles are nylon-12). Elemental analysis confirmed that these particles were not alloyed after 2 hours of cryogenic MA.

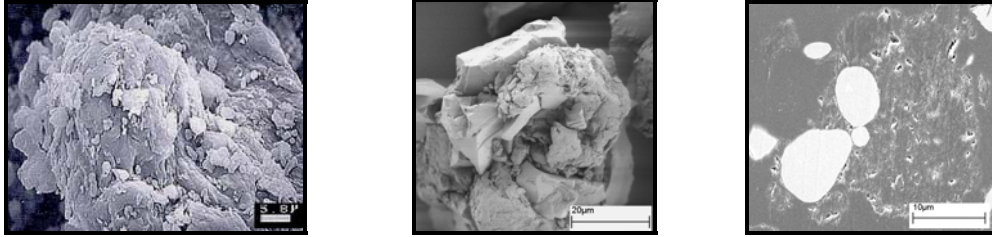


**Figure 4.3a-c:** Micrographs of MA a) PEEK-LaRC-TPI particle, b) alumina-nylon-12 particle c) tin-nylon12 particles.

Atomic force microscopy phase contrast images can be used to image two polymers if their chemistries, hardness or modulus values, or microstructural characteristics cause relative differences in the phase signal of the tip in TappingMode™. Figure 4.4 shows a phase contrast image of an injection molded PC-PEEK bar. Two phases can be distinguished in this sample in the AFM phase image.

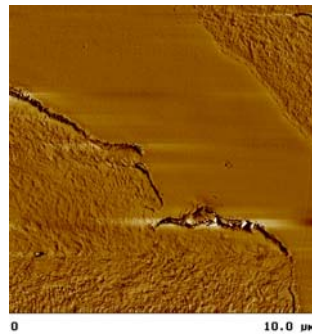


**Figure 4.4:** AFM phase image of injection molded PEEK/PC bar (10μm x10μm cross-section).

### 4.3 Processing

The technical approach to processing in this work can be divided into two categories: the mechanical processing of powders (mechanical milling or alloying) and the post-MA processing into a usable shape by injection molding. In the mechanical alloying process itself, several parameters can be varied. First of all, the charge ratio can be changed by varying either the total volume (mass) of the polymer powder, or the number of balls used (total ball mass). The milling time can also be varied, with the assumption that longer times generally result in further alloying if all other variables remain the same. The mill design used also affects

results, as different mill designs impart different amounts of energy. Milling temperature is also known to affect the resultant blend, since lower temperatures generally make the polymers more brittle during the MA process.

While several studies have examined the effects of melt-pressing mechanically alloyed powders, none have examined the effects of both temperature and shear on the morphology and properties of post-mechanically alloyed processed parts: a more realistic proposition, as polymeric parts are commonly injection molded or extruded rather than pressed. A miniature ram injection molding machine that uses very little material would be ideal for a laboratory-scale study. The widest variation in microstructure would be obtained by molding at temperatures covering the full processing temperature window of the system. The resultant coupons could then be used for testing and characterization as a function of MA parameters as well as injection molding conditions.

#### **4.4 Testing**

In order to answer the first question raised in this work regarding the effects of the milling process on individual polymers, properties such as glass transition temperature, degradation temperature, and crystallinity should be examined. These tests could also be applied to mechanically alloyed powders. Changes in these characteristic transitions may indicate that the MM or MA process promotes degradation. In addition, knowledge of the molecular weight distributions of the MM components would help answer questions about whether chain scission and/or cross-linking occur during the MM process. Furthermore, changes in powder chemistry in MM and MA powders may be detected with infrared spectroscopy.

Once parts have been injection molded into bars, mechanical properties will be explored to determine if the properties of mechanically alloyed samples are different than non-mechanically alloyed samples. Failure strength, strain at failure, and energy to break can be obtained from a quasi-static 3- point bend test. In addition to static testing, examination of dynamic mechanical behavior may elucidate differences between coupons made from mechanically alloyed samples and those made from non-mechanically alloyed

materials. Dynamic mechanical measurements consist of subjecting the sample to oscillating sinusoidal loads, causing the sample to undergo small amplitude displacements.<sup>50,51</sup> Measurements may be conducted at a fixed frequency as a function of temperature, or isothermal measurements may be taken as a function of frequency. Because polymers are viscoelastic materials, the polymer molecules store a portion of the energy elastically and dissipate some of the energy as heat. As a result, measured strain lags behind the stress<sup>51</sup> (Figure 4.5).

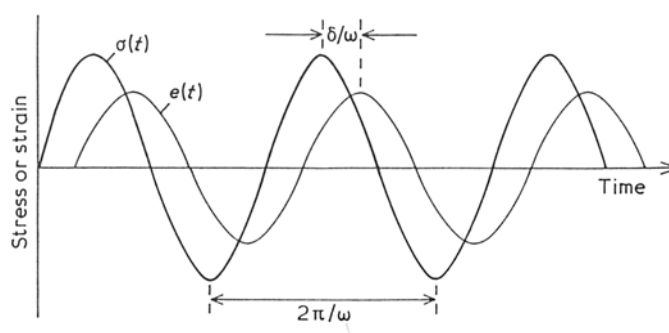


**Figure 4.5:** Response of a viscoelastic material to applied stress or strain.<sup>51</sup>

Measured quantities include the dynamic moduli,  $E'$ , which measures the elastic portion and  $E''$ , which measures the loss portion. The ratio between the two is defined as  $\tan \delta$ , where  $\delta$  is the angle between the in and out of phase components. Peaks in  $E''$  or  $\tan \delta$  are commonly used to define the characteristic glass transition temperature.<sup>50,51</sup> In this study, dynamic mechanical behavior could be evaluated using a similar geometry, allowing changes in  $T_g$ , loss and storage modulus to be evaluated as a function of MA conditions.

## 4.5 Chapter Summary

In this chapter, an approach to an appropriate test methodology has been identified and discussed. This technical approach will enable a model polymer-polymer system to be selected and studied, addressing the following questions about the effects of MM and MA on a model polymeric system: 1) How does MM affect the properties of an individual polymer? 2) Do the morphology and properties of the powders or injection molded parts change with MA compared to a set of control samples? 3) Does demixing occur upon post-MA

injection molding, and if so, how does it affect selected properties? Given these goals and the selection criteria for a model system outlined in Section 4.1, a model system has been selected and is described in Section 5.1. The specific test methodologies selected for this work are based on the previous discussion, and are described in detail in the following chapter.

## 5. MATERIALS AND METHODS

### 5.1 Materials

The materials selected for this research include relatively low molecular weight versions of a semi-crystalline thermoplastic, poly (ether ether ketone) (PEEK) and an amorphous thermoplastic, polycarbonate (PC). This system was chosen because of its ability to be imaged by a variety of techniques as well as its attractive physical property combination. PC is a relatively tough polymer, while PEEK is a relatively stiff polymer. If any synergistic effects could be garnered by the combination of these materials via MA, this system has potential to be a useful blend. Furthermore, the semi-crystalline (PEEK) and amorphous (PC) phase domains present in the system's injection molded parts can be imaged in TappingMode™ AFM, with distinct phases visible, as well as via TEM with no staining necessary. This system has been previously studied by Schultz at Virginia Tech<sup>52,54</sup> as a potential system for rapid prototyping laser sintering applications, and has industrial potential in that arena.

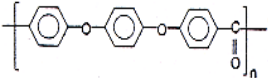
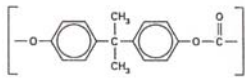
#### 5.1.1 Polycarbonate (PC)

A commercial grade of polycarbonate, Laserite™ Polycarbonate Compound powder (LPC3000), was obtained from DTM Corporation of Austin, Texas. This material is commonly used in rapid prototyping laser sintering applications. Gel permeation chromatography (GPC) analysis conducted as part of this work indicates that the as-received material has a weight average molecular weight of 22,915 g/mole and a number average molecular weight of 12,605 g/mole (PDI=1.82). Structure and thermal properties are given in Table 5.1.

#### 5.1.2 Poly(aryl ether ether ketone) (PEEK)

Victrex® PEEK 150PF powder was obtained from Victrex USA, Inc. of Greenville, South Carolina. The intrinsic viscosity reported by the supplier is approximately 1.5 Pa-s, corresponding to weight and number

average molecular weights of 33,500 and 11,700 g/mol, respectively (PDI=2.86).<sup>53</sup> Structure and thermal properties are shown in Table 5.1.

	PEEK	Polycarbonate
Chemical Structure		
T <sub>g</sub>	≈145°C	≈144°C
T <sub>m</sub>	≈346°C	No T <sub>m</sub> (amorphous)

**Table 5.1:** Selected material properties. T<sub>g</sub> and T<sub>m</sub> values were measured using DSC performed at 10°C/minute.

## 5.2 Mechanical Milling and Alloying

A cryogenic vibratory ball mill, designed and built by Schultz at Virginia Tech,<sup>54</sup> was used to form blends at cryogenic temperatures (approaching -196°C). Liquid nitrogen was continuously dripped over the vial into the mill unit, ensuring that the vial was kept cold throughout the milling process. The milling vial and balls used were stainless steel. The ball mill provides linear vibratory motion on a single axis. This mill was designed as an alternative to a commercial SPEX mill because of its cryogenic capabilities and significantly larger vial volume milled per batch. A photo (Figure 5.2) and schematic of the ball mill (Figure 5.3) are shown below.

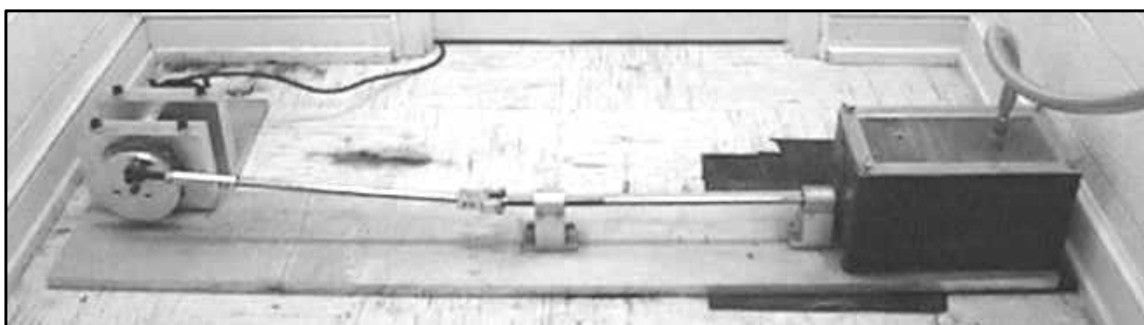


**Figure 5.2:** Photo of the ball mill used in this work.<sup>52</sup>

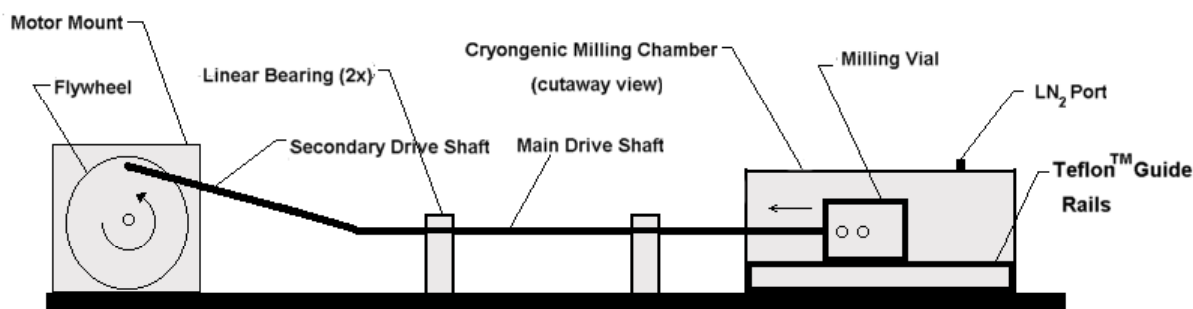


**Figure 5.3:** Schematic of the ball mill.<sup>52</sup>

Binary blends of PEEK/PC were produced from resins in powder form in a 50/50 volume percent ratio. Individual components and blends were milled for periods of time from 1 to 10 hours at various charge ratios (Table 5.1). The motor speed was set between 425-450 rpm (corresponding to approximately 8 Hz) for all samples. The polymer masses were chosen to maintain the volume fraction ratio and a total powder volume of 30 cubic centimeters

Sample Designation	Material	Total Polymer Mass	# Milling Balls	Charge Ratio	Temperature	Time (hrs)
Mixed	PC-PEEK	35.3	-	-	-	0
Control	PC-PEEK	35.3	2	2	Cryogenic	1
PC CMM 10h	PC	33.9	4	4	Cryogenic	10
PEEK CMM 5h	PEEK	36.7	4	3.8	Cryogenic	5
PEEK CMM 10h	PEEK	36.7	4	3.8	Cryogenic	10
PC AMM 10h	PC	33.9	4	4	Ambient	10
PEEK AMM 5h	PEEK	36.7	4	3.8	Ambient	5
PEEK AMM 10h	PEEK	36.7	4	3.8	Ambient	10
CMA 5h	PC-PEEK	35.3	4	4	Cryogenic	5
AMA 5h	PC-PEEK	35.3	4	4	Ambient	5
CMA 10h	PC-PEEK	35.3	4	4	Cryogenic	10
AMA 10h	PC-PEEK	35.3	4	4	Ambient	10

**Table 5.2:** Mechanical alloying conditions

### 5.3 Injection Molding Processing

In order to examine the effects of post-mechanically alloyed processing on the microstructure and properties of the materials used in this study, a DACA Instruments (Goleta, California) MicroInjector™ mini-

ram injection molder was used to make bars suitable for mechanical testing. “Shots” of four bars were made using approximately 4g of powder per shot (Figure 5.4) from 50/50 volume percent mixtures of as-received powders and cryogenically mechanically alloyed powders. Bars were designated “o” and “i” for outer and inner, respectively, due to potential differences in shear conditions between the two during molding. Molding temperatures of 350°C, 360°C, 370°C, 380°C and 390°C were chosen because they represent the range of processing for this blend system: at 350°C (approximately the  $T_m$  of the PEEK semi-crystalline component) the polymer barely flowed into the mold. At 390°C, the PC began to degrade if it remained in the barrel more than a few minutes.

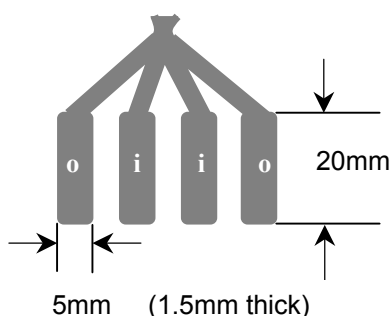


**Figure 5.4:** Schematic of injection molded bar coupon.

Prior to molding bars, the barrel was pre-heated, the polymers were packed in the barrel, and then allowed to equilibrate to temperature for 5 minutes before being injected into the room temperature mold.

## 5.4 Characterization of Mechanically Milled and Mechanically Alloyed Powders

### 5.4.1 Particle Size Analysis

A Horiba LA-700 particle size analyzer was used to obtain particle size distributions of as-received and mechanically milled and alloyed powder samples. The particle size analyzer equipment uses light scattering to determine particle size histograms of the powders dispersed in ethanol. A sample histogram of unmilled PC obtained from raw data is shown in Figure 5.5.

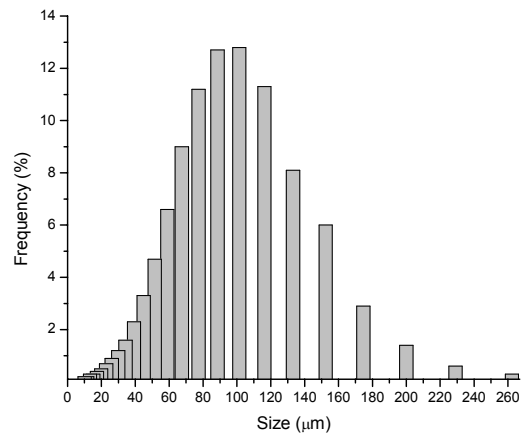


**Figure 5.5:** Sample particle size histogram obtained from Horiba L-700 instrument.

#### 5.4.2 Thermogravimetric Analysis (TGA)

A Perkin-Elmer TGA-7 thermogravimetric analyzer was used to determine degradation temperatures of the individual components and mechanically alloyed powders. The samples were heated at a rate of 10°C/minute in a nitrogen environment. The temperature corresponding to the peak in the first derivative of weight percent with time is reported as the degradation temperature ( $T_d$ ), indicating the temperature corresponding to the highest rate of degradation. These calculations are performed from raw weight percent vs. temperature data using the software accompanying the TGA-7. Additional tests were conducted in air to simulate heating during the injection molding process. Example raw data curves for Unmilled PC are shown in Figure 5.6.

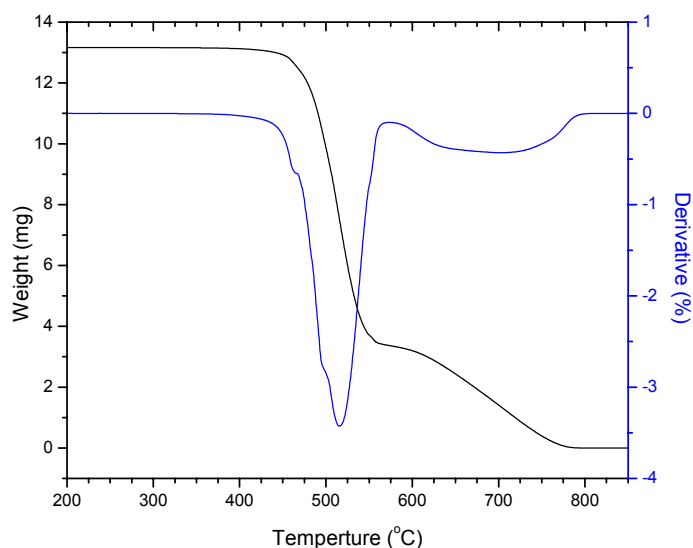


**Figure 5.6:** TGA Unmilled PC raw data plot and derivative.

### 5.4.3 Gel Permeation Chromatography

Gel permeation chromatography was performed on four replicates of Unmilled and CMM 10h PC powders at Viscotek Corporation in Houston, TX using a Viscotek Model 300 Triple Detector System. Powders were dissolved in methylene chloride and data was collected at a flow rate of 1.0 ml/minute. Results were analyzed using TriSEC software.

### 5.4.4 Melt Rheology

Viscosity data was collected in a nitrogen environment using a TA AR1000 Advanced Rheometer on Unmilled PEEK and CMM 10h PEEK at 375°C using a frequency sweep of 0.1-100 rad/sec. A plate gap of 1000 $\mu$ m was used with 5% strain, and seven points per decade were recorded. Zero shear viscosity values were extrapolated from log viscosity vs. log frequency plots. Zero shear viscosity values were used to estimate the weight average molecular weight ( $M_w$ ) values of Unmilled PEEK and CMM 10h PEEK samples using the equation

$$\eta = kM_w^a \quad \text{Equation 5.1}$$

where  $\eta$  is the zero shear viscosity,  $M_w$  is the weight average molecular weight and  $k$  and  $a$  are material constants.

#### 5.4.5 Fourier Transform Infrared Spectroscopy

Fourier transform infrared spectroscopy was performed on selected powder samples using a Nicolet Impact 510™ spectrometer with a Spectra-Tech ATR attachment utilizing a horizontal ZnSe crystal at  $2\text{ cm}^{-1}$  resolution, and 128 scans per sample. The collected spectra were analyzed using Omnic 3.0 software in order to determine if any potential chemical changes occurring during the MM process could be detected with this method. Figure 5.7 shows sample FTIR spectra for Unmilled PC.

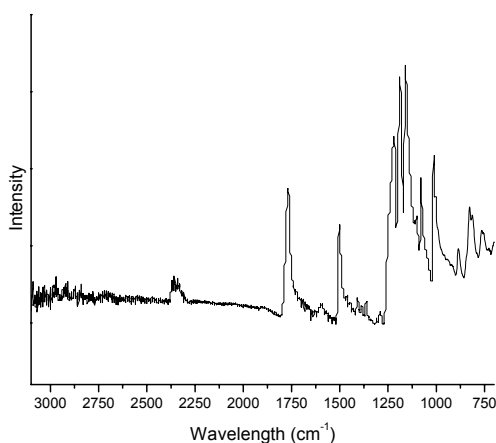


Figure 5.7: FTIR spectra of Unmilled PC.

#### 5.4.6 Wide Angle X-Ray Diffraction

Wide angle X-ray diffraction spectra were collected for PEEK samples before and after mechanical processing at various conditions in order to compare crystalline index values as well as crystal structure information. The spectrum corresponding to PEEK in its amorphous state (obtained by rapid quenching of a melt-pressed film) is scaled to the corresponding diffraction spectrum of the semi-crystalline material in order to calculate a crystalline index using the following equation:

$$\text{CrystallinityIndex} = \frac{A_{total} - A_{amor}}{A_{total}} \quad \text{Equation 5.1}$$

where  $A_{total}$  is the total integrated area of the semi-crystalline WAXD pattern and  $A_{amor}$  is the integrated area of the amorphous halo, adjusted to each diffraction spectrum. The scaling procedure is done using a macro in the Microsoft Excel program based on a program presented in the literature.<sup>55</sup> A sample spectrum and corresponding amorphous halo are shown for Unmilled PEEK in Figure 5.8.

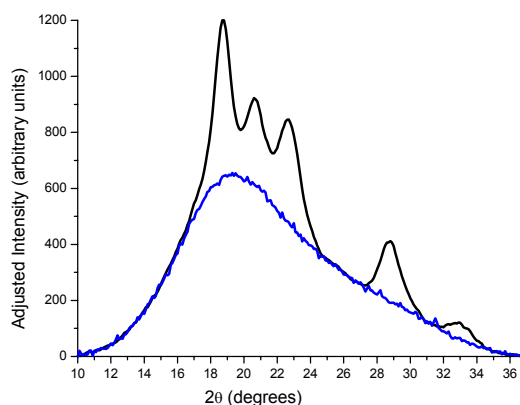


**Figure 5.8:** Amorphous halo adjusted to unmilled PEEK WAXD raw data.

#### 5.4.7 Differential Scanning Calorimetry

Sample masses of approximately 8-10mg (for powders) or 12-15mg (for bars) were heated in a Perkin Elmer DSC-7 in a nitrogen environment at a rate of 10°C/minute and a baseline subtraction was used. A second heat scan was performed after cooling the sample in the DSC instrument at 200°C/minute. Perkin Elmer software was used to determine glass transition, crystallization, and melting temperatures.

#### 5.4.8 Transmission Electron Microscopy

Transmission electron microscopy was performed on mechanically milled and alloyed powders. Powder particles were embedded in epoxy, which was cured at room temperature overnight, then microtomed onto 300 mesh gold grids. The resulting sections were examined using a Philips 420T Transmission Electron Microscope at 100kV.

#### **5.4.9 Scanning Transmission X-ray Microscopy**

Scanning Transmission X-ray Microscopy data were collected at Brookhaven National Lab's X-1A beamline in Upton, Long Island. X-ray images of the CMA 10h powder sample were taken in the form of a stack. To accomplish this, the sample was held in a fixed position while beam energy was varied, creating an absorption spectrum from a small volume of sample. Beam energy calibration was performed with carbon dioxide gas prior to data collection.

### **5.5 Characterization of Injection Molded Bars**

#### **5.5.1 Three-Point Bend Dynamic Mechanical Analysis**

A Perkin-Elmer DMA-7 was used to obtain dynamic mechanical data in 3-point bend mode at a frequency of 1 Hz. Storage modulus, loss modulus, and tan delta were recorded as a function of temperature. A 5mm span width fixture was used with a knife-edge probe. Isochronal scans were performed from 25°C to 200°C at a rate of 10°C/min. Displacement control mode was used to maintain deflection through  $T_g$ , with an applied static force that was 20% higher than the dynamic force. Some samples were also thermally annealed at 160°C for 20 minutes. Samples were placed on a platform located on top of the 3-point bend fixture so that no sample deflection could occur during annealing. The probe was lowered onto the sample with no applied load. After the annealing step, the sample was cooled to room temperature and the isochronal heating step described above was performed. Example storage and loss modulus curves are shown in Figure 5.9.

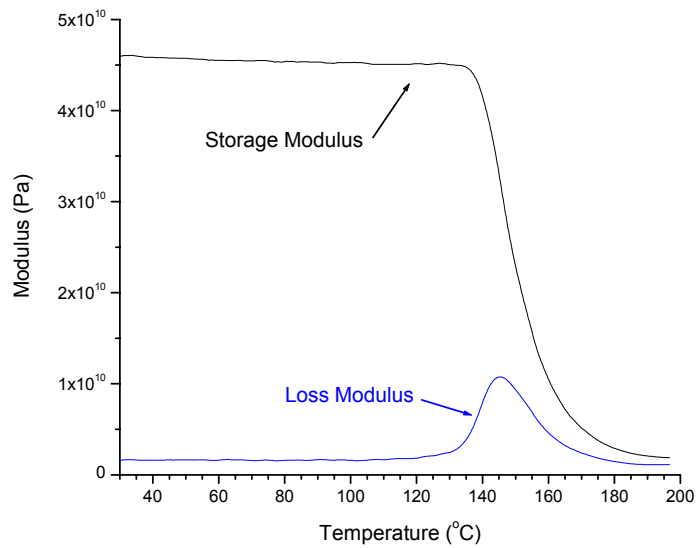


**Figure 5.9:** DMA data for Mixed sample injection molded at 360°C then annealed.

### 5.5.2 Three-Point Bend Quasi-Static Testing

A TA.XT2i Texture Analyzer (Texture Technologies Corp., Scarsdale, NY/Stable Micro Systems, Godalming, Surrey, UK) (referred to as the TA.XT2i) with a three-point bend fixture was used to test injection molded bars of mixed and mechanically alloyed systems. A span width of 5.14mm was used. Tests were performed at rates of 0.1mm/sec and 1.0 mm/sec. Load vs. displacement data was obtained, and converted to stress ( $\sigma$ ) vs. strain ( $\epsilon$ ).

If the samples did not fracture by the time 40% strain was reached, the test was stopped because at this point the specimen slid down into the 3-point bend fixture, rendering results past 40% strain inaccurate. Failure strength and strain at failure values were obtained by identifying the stress and strain at which either (1) the sample fractured or (2) the test was stopped. In addition, the energy absorbed per unit volume of the sample, termed the “energy to failure” here, was obtained by integration of the stress-strain plots.

### 5.5.3 Scanning Electron Microscopy

A LEO 1550 field emission scanning electron microscope with an accelerating voltage of 20kV was used to view the topology of the mechanically processed powders and fracture surfaces of injection molded bars.

Prior to imaging, a BAL-TEC SCD 05 sputter coater was used to coat samples with gold to prevent charging during imaging.

#### **5.5.4 Transmission Electron Microscopy**

The injection molded bar samples were microtomed at room temperature and resulting sections were collected on 300 mesh gold grids. The resulting sections were examined using a Philips 420T Transmission Electron Microscope at 100kV.

#### **5.5.5 Atomic Force Microscopy**

A Digital Instruments Nanoscope IIIa™ atomic force microscope was used in TappingMode™ on samples of powders and injection molded bars. All samples were microtomed at room temperature. Powder samples were embedded in epoxy prior to microtoming. Phase contrast images are reported in this work.

#### **5.5.6 Scanning Transmission X-ray Microscopy**

STXM images were obtained from selected injection molded bar samples. After initial X-ray spectra were obtained for individual PC and PEEK samples, a photon energy of 286.2eV was chosen for data collection, as the PEEK absorbs at this energy and the PC does not, causing the PEEK phase to appear darker in the X-ray images.

## 6. RESULTS FROM MECHANICALLY MILLED POWDERS

### 6.1 Characterization of Powders

#### 6.1.1 Particle Size Analysis

Particle size histograms of Unmilled PC and PC CMM 10h samples are shown in Figure 6.1 and Figure 6.2. Histograms are shown for PEEK samples in Figure 6.3 and Figure 6.4. The mean and median particle size values are shown in Table 6.1. In addition, mean particle size values shown graphically in Figure 6.5.

Mean particle size values for Unmilled PC are larger than Unmilled PEEK, and Unmilled PC exhibits a more uniform distributions. Upon cryogenic mechanical milling, mean particle size values decrease with increased mechanical milling time. Upon ambient mechanical milling, the mean particle size increases relative to the Unmilled size, as a result of the dominance of welding over fracture during the mechanical milling process. Mechanical milling at room temperature therefore produces larger, flatter particles that resemble flakes (shown in Figure 6.16 (b) and (e), values reported in Table 6.1). Upon cryogenic mechanical milling of PEEK, the mean particle size values initially decrease, then, after 10 hours of CMM, increase to approximately the same values as the Unmilled powder.

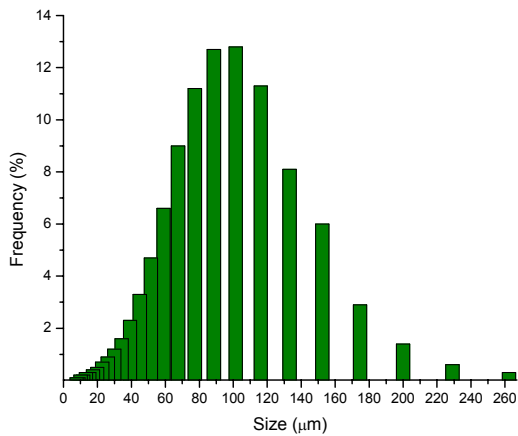


**Figure 6.1:** Particle size histogram for Unmilled PC.

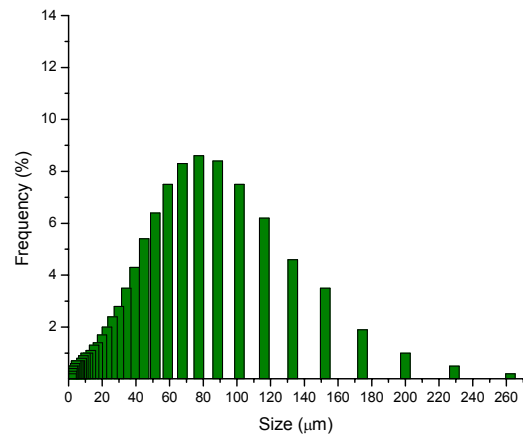


**Figure 6.2:** Particle size histogram for PC MM 10h.

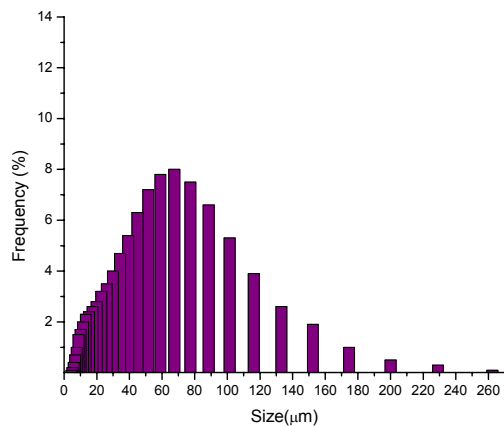


**Figure 6.3:** Particle size histogram for Unmilled PEEK.

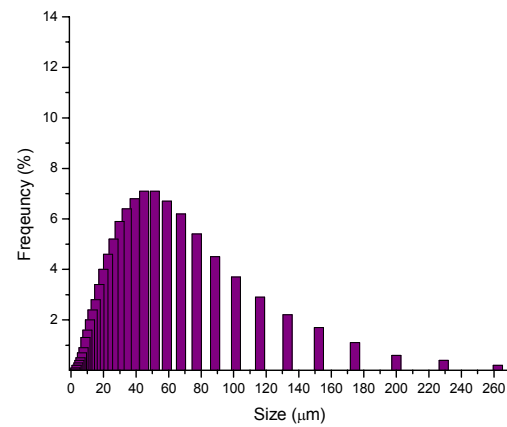


**Figure 6.4:** Particle size histogram for PEEK CMM10h.

Sample	Mean (μm)	Median Particle Size (μm)	Sample	Mean (μm)	Median Particle Size (μm)
Unmilled PC	89.00 ± 4.50	79.40 ± 4.44	Unmilled PEEK	56.26 ± 1.03	46.58 ± 0.57
PC CMM 5h	75.38 ± 5.91	41.17 ± 3.03	PEEK CMM 5h	43.78 ± 1.13	32.98 ± 0.39
PC CMM 10h	66.58 ± 5.60	57.71 ± 4.35	PEEK CMM 10h	53.70 ± 2.37	41.17 ± 3.03
PC AMM 10h	94.71 ± 5.17	86.54 ± 7.71			

**Table 6.1:** Particle size data for unmilled and mechanically milled materials.

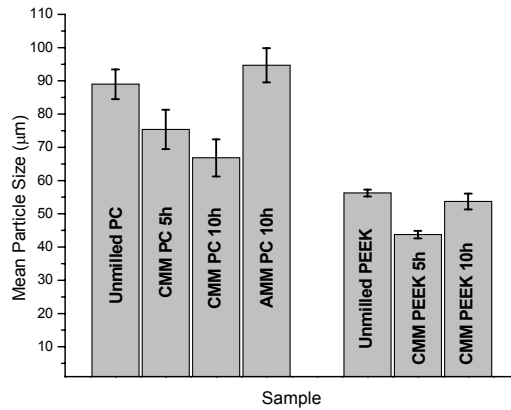


**Figure 6.5:** Mean particle size values for Unmilled and mechanically milled powders.

### 6.1.2 Thermogravimetric Analysis

Representative raw (weight vs. temperature) data and derivative plots obtained from TGA are shown in Figure 6.6 and Figure 6.7 for Unmilled PC and Unmilled PEEK samples.

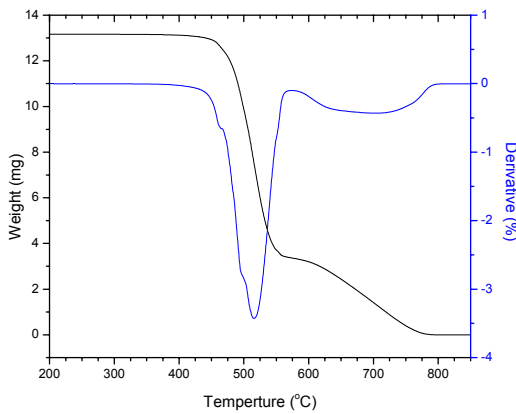


**Figure 6.6:** Typical Unmilled PC TGA raw data and derivative plot.

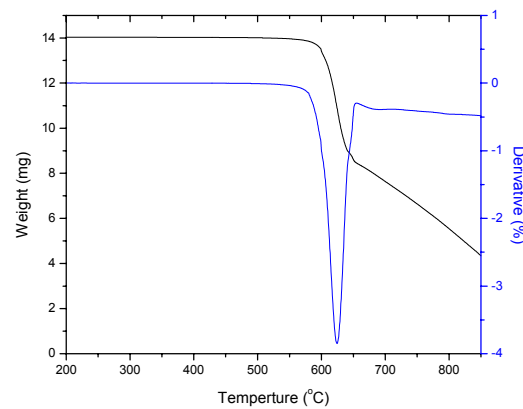


**Figure 6.7:** Typical Unmilled PEEK TGA raw data and derivative plot.

Degradation temperatures of mechanically milled materials are shown in Figure 6.8 and Figure 6.9. The values shown correspond to the value of the peak in the derivative of the weight percent vs. temperature curve. These values are averages from three experiments, shown here with standard deviation error bars.

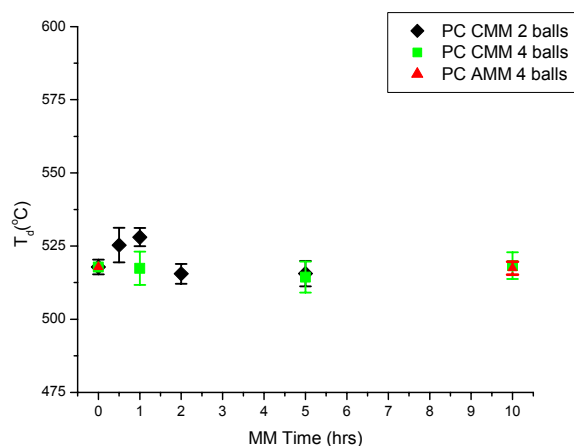


**Figure 6.8:** Degradation temperatures of mechanically milled PC.

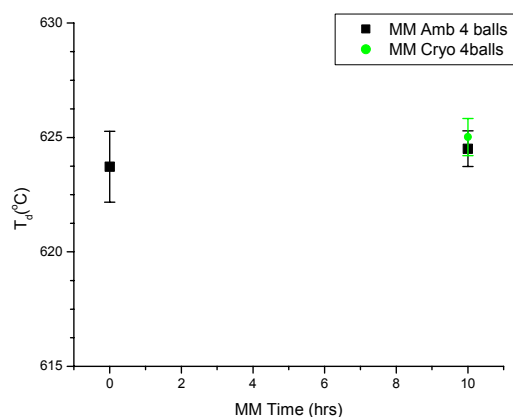


**Figure 6.9:** Degradation temperatures of mechanically milled PEEK.

No drastic differences in degradation temperatures of the Unmilled vs. mechanically milled materials are observed for milling times up to 10 hours, regardless of the mechanical milling time, temperature, or number of milling balls used. Likewise, no significant changes in peak shape or onset are observed for MM PC or PEEK samples. While the peak in the derivative value is the most reproducible way to determine a characteristic degradation temperature, the actual degradation temperature of the material exhibits an onset at a lower temperature and also depends on the time spent at a given temperature and, therefore, the rate of heating.

### 6.1.3 Differential Scanning Calorimetry

Differential scanning calorimetry tests were performed on Unmilled, CMM 10h and AMM 10h samples of both PC and PEEK. Following the first heat, samples were allowed to cool to room temperature and a second heat was performed. Raw data is shown in Figure 6.10 and Figure 6.11, and transition values are shown in Table 6.1.

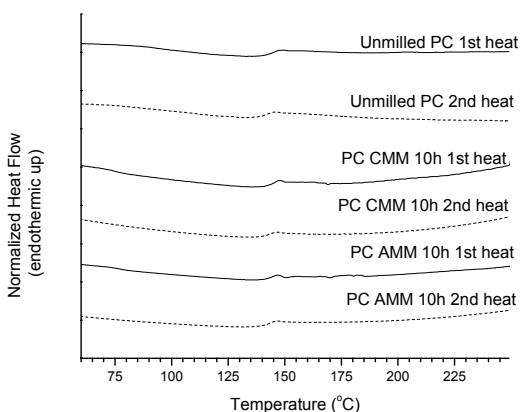


**Figure 6.10:** DSC curves performed at 10°C/minute for Unmilled PC, PC CMM, and PC AMM. Curves have been shifted vertically for comparison.

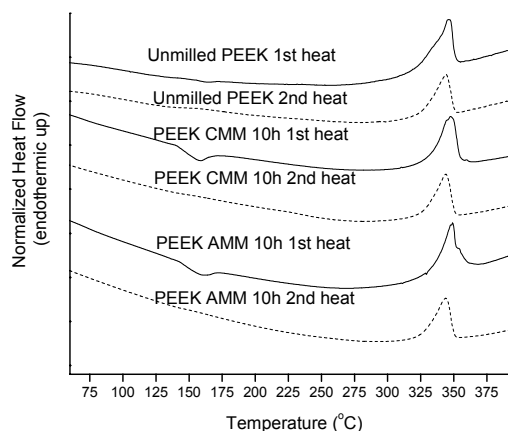


**Figure 6.11:** DSC curves performed at 10°C/minute for Unmilled PEEK, PEEK CMM, and PEEK AMM. Curves have been shifted vertically for comparison.

	PEEK			PC
	$T_g$	$T_c$	$T_m$	$T_g$
Unmilled	$145.0 \pm 1.6$	$163.4 \pm 0.2$	$345.7 \pm 1.4$	$143.8 \pm 0.9$
CMM 10h	---	$157.4 \pm 0.5$	$347.4 \pm 0.9$	$144.1 \pm 1.1$
AMM 10h	$148.9 \pm 2.1$	$159.1 \pm 0.5$	$348.1 \pm 0.9$	$143.5 \pm 0.8$

**Table 6.2:** Transition values obtained from DSC data.

According to T-tests (performed at a 95% confidence level), differences in  $T_g$  values for Unmilled PEEK are not significantly different from those of PEEK AMM 10h samples. No  $T_g$  value is reported for PEEK CMM 10h samples, as it was difficult to discern a reproducible glass transition from DSC curves. Crystallization temperature values for Unmilled PEEK, PEEK CMM 10h, and PEEK AMM 10h samples are significantly different. Differences in  $T_m$  values for PEEK and  $T_g$  values for PC are not significantly different for Unmilled samples compared to mechanically milled samples.

#### 6.1.4 Gel Permeation Chromatography

Number and weight average molecular weights, as well as polydispersity index values of polycarbonate powders cryogenically MM at various times and charge ratios were determined from GPC data collected at Viscotek. The results from four replicate tests are summarized in Table 6.3.

Sample-Replicate #	$M_w$	$M_n$	PDI
Unmilled PC-1	22,890	12,520	1.83
Unmilled PC-2	22,920	12,660	1.81
Unmilled PC-3	22,930	12,670	1.81
Unmilled PC-4	22,920	12,570	1.82
<b>Unmilled PC Mean</b>	<b>22,915 ± 17</b>	<b>12,605 ± 72</b>	<b>1.82</b>
PC CMM 10h-1	22,570	12,100	1.87
PC CMM 10h-2	22,650	12,240	1.85
PC CMM 10h-3	22,690	12,390	1.83
PC CMM 10h-4	22,650	12,350	1.83
<b>PC CMM 10h Mean</b>	<b>22,640 ± 50</b>	<b>12,270 ± 130</b>	<b>1.85</b>

**Table 6.3:** GPC results for Unmilled and PC CMM 10h samples.

T-tests performed on  $M_w$  and  $M_n$  values obtained for Unmilled PC and PC CMM 10h samples indicate that the differences measured in these values, although small, are statistically significant, indicating that some chain degradation does occur during cryogenic mechanical milling of PC. If it is assumed that chains break in the middle, the reported decrease in molecular weight corresponds to approximately 2.5% of the chains fracturing during mechanical milling.

### 6.1.5 Melt Rheology

Viscosity data is shown in Figure 6.12 for Unmilled PEEK and CMM 10h PEEK samples along with the zero shear viscosity values obtained from a linear fit of low frequency viscosity data.

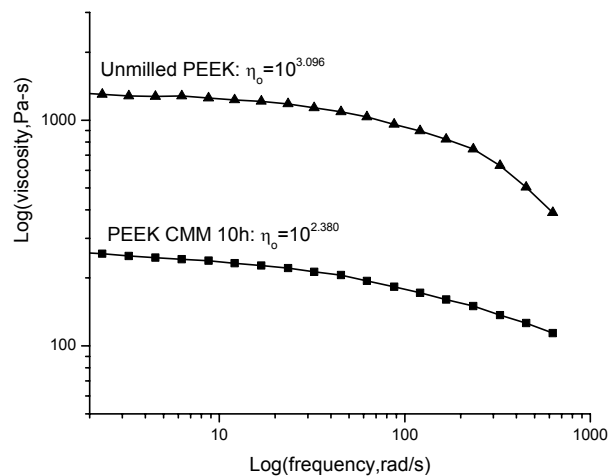


**Figure 6.12:** Melt rheology data obtained for Unmilled PEEK and CMM 10h PEEK.

The zero shear viscosity values calculated for Unmilled PEEK and PEEK CMM 10h samples are given in Table 6.4. Using  $a=3.4$  (a reasonable value for most polymers above the critical molecular weight for entanglement) for the power constant Equation 5.1, and assuming that the  $K$  values are equivalent for both PEEK samples, an estimate for the weight average molecular weights of the Unmilled PEEK and CMM 10h PEEK samples can be obtained using the  $M_w$  value for Unmilled PEEK of 33,500g/mol provided by the supplier.

	$\eta$ (Pa-s)	Approximate $M_w$ (g/mol)
Unmilled PEEK	1247.4	33,500
PEEK CMM 10h	239.9	20,628

**Table 6.4:** Melt rheology data.

These data indicate that a significant decrease in molecular weight may occur as a result of cryogenically mechanically milling PEEK powder for 10 hours. If it is assumed that chains break in the middle, the reported decrease in molecular weight corresponds to nearly 77% of the chains fracturing during mechanical milling. In addition, the shape of the log viscosity vs. log frequency curves indicate that the molecular weight distribution of the PEEK CMM 10h sample has a larger polydispersity index than the Unmilled PEEK sample.

### 6.1.6 Fourier Transform Infrared Spectroscopy

Infrared spectra of Unmilled PEEK and PEEK CMM 10h samples are shown in Figure 6.13. While peak intensity may vary due to variations in powder contact with the stage, no new peaks are observed in the MM sample, and no existing peaks disappear in milled sample spectra compared to the unmilled sample spectra.

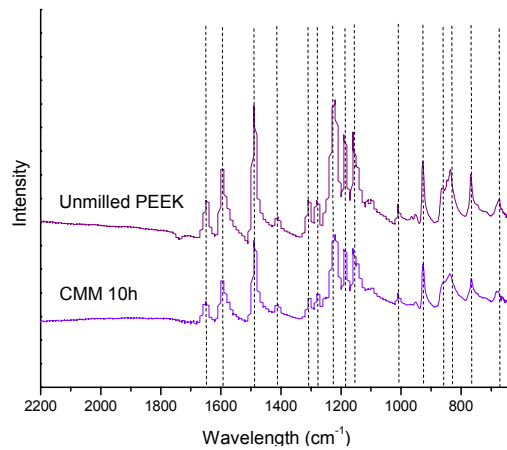


**Figure 6.13:** FTIR spectra of Unmilled PEEK and PEEK CMM 10h samples. Spectra have been shifted vertically for comparison.

### 6.1.7 Wide Angle X-Ray Diffraction

Wide angle X-ray diffraction patterns are shown in Figure 6.14 for PEEK CMM samples milled with 2 balls for up to 90 minutes as well as PEEK CMM samples milled with 4 balls for 5 and 10 hours.

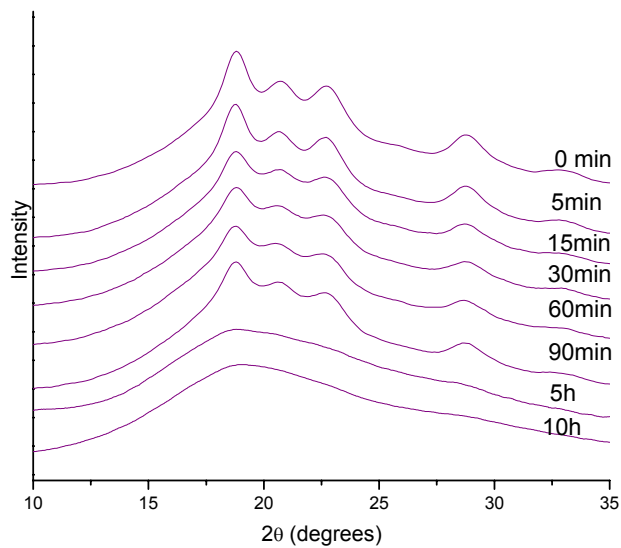


**Figure 6.14:** WAXD patterns for PEEK CMM samples milled for various times. Data have been shifted vertically for comparison.

The crystallinity index values (calculated according to Equation 5.3) for the PEEK AMM and CMM samples are plotted as a function of milling time in Figure 6.15. Each point shown is the average of three experiments and standard deviations are shown as error bars.

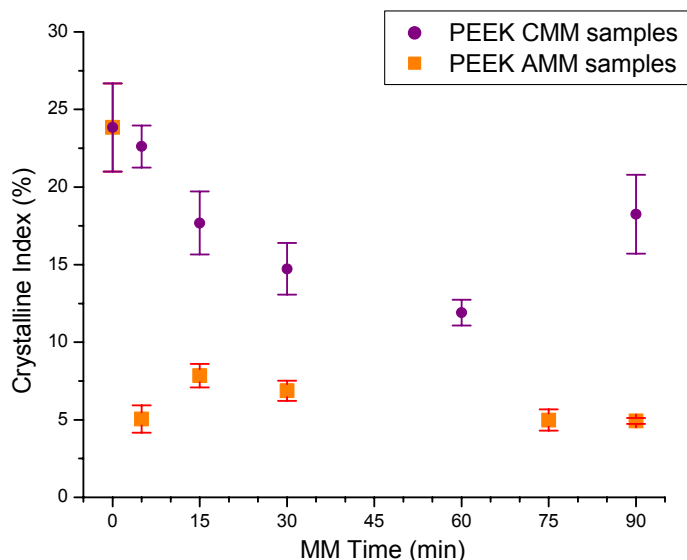


**Figure 6.15:** Crystallinity index values calculated from WAXD data for PEEK CMM and PEEK AMM samples.

A comparison of crystallinity index values as a function of milling time for PEEK milled at ambient and cryogenic temperatures, suggests that the rise in crystallinity index values is due to strain-induced crystallization rather than thermal recrystallization, since the CMM samples are milled at a temperature far below the crystallization temperature ( $T_c$ ) of PEEK. At long milling times (5 and 10 hours), the WAXD patterns closely resemble those of amorphous PEEK and have a crystallinity index value near zero (Figure 6.15).

The width of the first three crystalline peaks in the WAXD spectra remain constant up for milling times up to 90 minutes. In addition, the location of the WAXD peaks does not change significantly (within machine variation) as a result of milling, no new peaks appear in the pattern, and no existing peaks disappear. These results suggest that no alternate crystal structures or polymorphs form upon CMM.

## 6.2 Imaging Mechanically Milled Powders

### 6.2.1 Field Emission Scanning Electron Microscopy

Example micrographs of Unmilled, AMM and CMM polycarbonate and PEEK samples are shown in Figure 6.16. All micrographs were taken at the same magnification, and 10 $\mu$ m bars are shown for each.

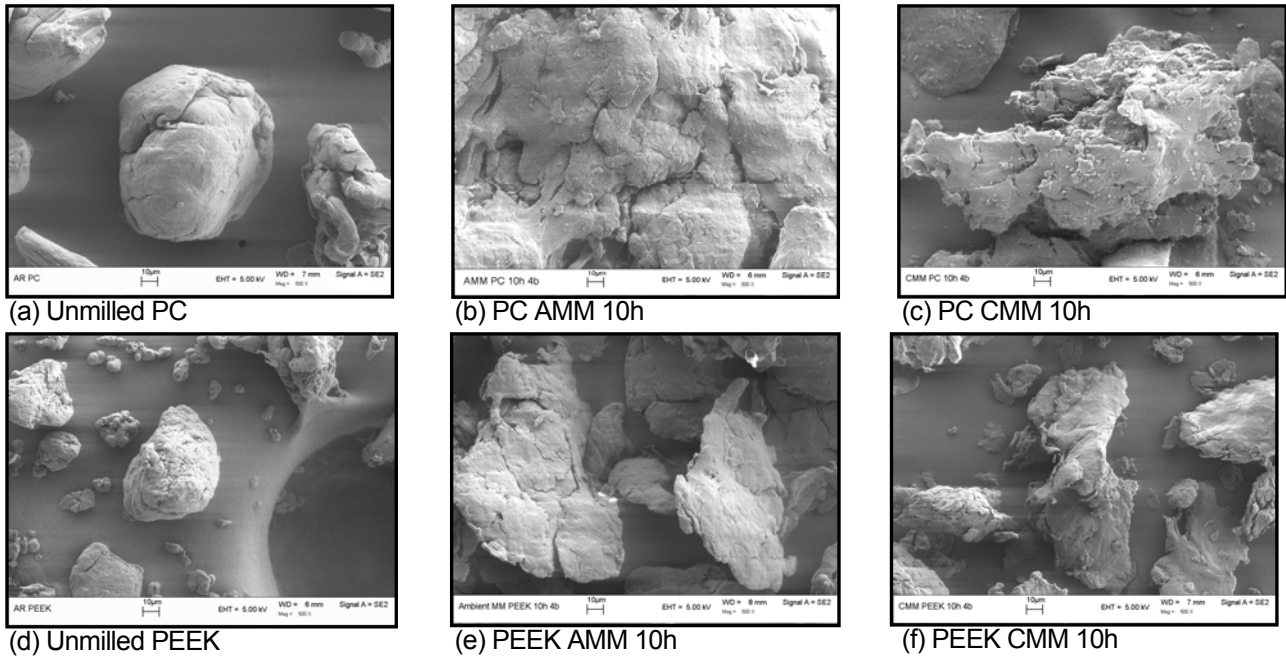


**Figure 6.16:** Field emission scanning electron micrographs of PC and PEEK before and after mechanical milling.

No quantitative conclusions regarding particle size information can be drawn from these micrographs; they illustrate differences in shape of the unmilled particles compared to mechanically milled samples. The AMM and CMM powders consist of layers of material which have been fractured then cold-welded during the mechanical alloying process, resulting in a layered appearance. The AMM particles especially appear similar to flakes, rather than the more spherical shapes of the Unmilled particles. In some micrographs, the carbon tape used to adhere the powder to the sample mount is visible (especially Figure 6.16d). The violent nature of the milling process is evidenced by the CMM PEEK 10hrs micrograph (Figure 6.16f), which shows a particle that has been twisted in the milling process. These results qualitatively support the particle size analysis data, which demonstrated that AMM particles are in general larger than CMM particles, and the PC particles are larger on average than the PEEK particles. Recall that the particle size analysis data presented

in Section 6.1 indicated that the mean particle size for CMM PC particles was smaller than the Unmilled PC particles. The mean particle size for CMM PEEK particles was approximately the same as Unmilled PEEK particles, which is not evident from the particles represented in these micrographs.

### 6.2.2 Transmission Electron Microscopy

Transmission electron micrographs of Unmilled PC and PC CMM 10h samples as well as Unmilled PEEK and PEEK CMM 10h are shown below. The micrographs showing Unmilled PC (Figure 6.17 and 6.20) reveal very little contrast within the Unmilled PC particle or the PC CMM 10h particle.

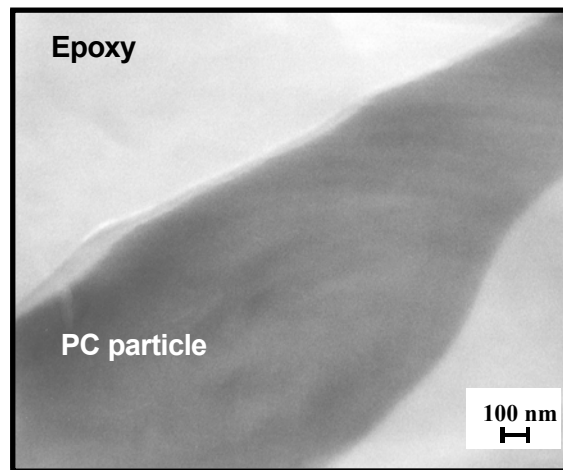


Figure 6.17: TEM micrograph of Unmilled PC.

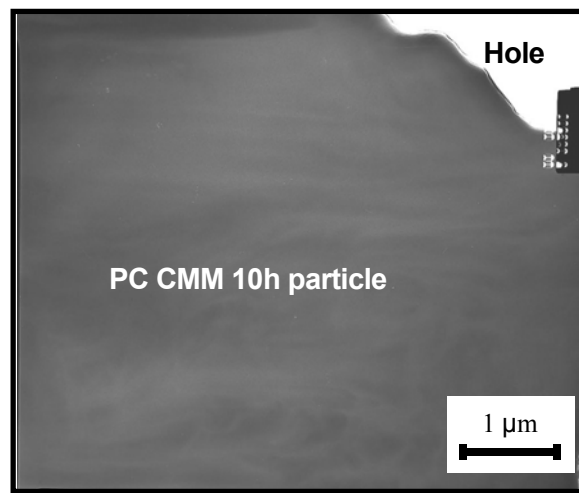
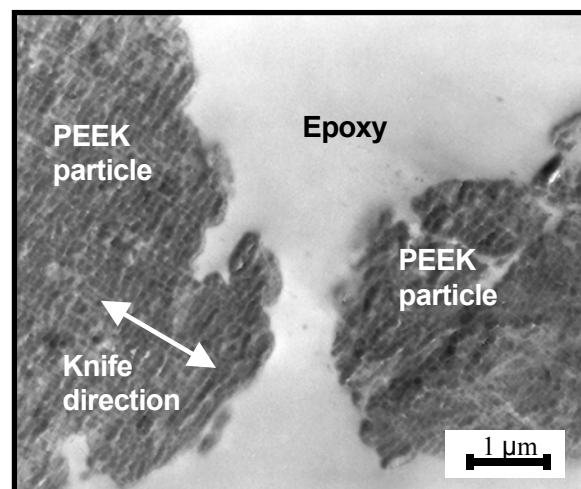


Figure 6.18: TEM micrograph PC CMM 10h.

A micrograph of Unmilled PEEK cross-section is shown in Figure 6.19. The PEEK particles are labeled, along with the mounting epoxy and the direction of the microtoming knife. Knife marks are visible within the particles, along with a sample preparation artifact known as chatter. Chatter occurred here perpendicular to the knife direction because the microtoming knife cannot cut through the PEEK phase as easily as the epoxy phase due to hardness differences; this results in the phenomena of “stick-slip” as the knife passes across the surface. Chatter is a common artifact of microtoming sample preparation for polymers, and generally is more apparent in hard phases compared to softer phases. Contrasting areas of light and dark are also visible in the Unmilled PEEK particles. This effect could be due to slight thickness differences within the sample due to chatter.



**Figure 6.19:** TEM micrograph of Unmilled PEEK.

An examination of the PEEK CMM 10h sample (Figure 6.20) reveals knife marks and chatter within the particle, as well as contrast differences within the PEEK CMM 10h sample.

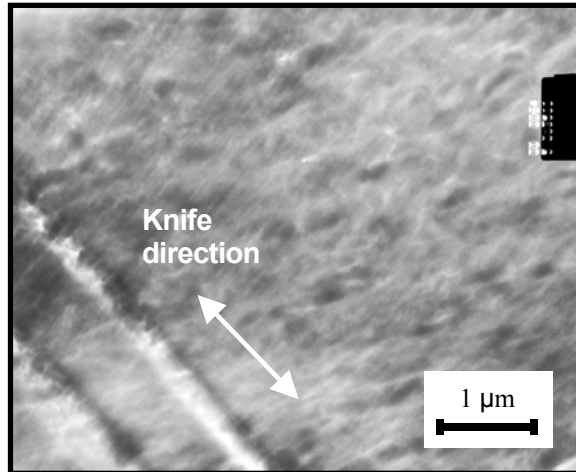


**Figure 6.20:** TEM micrograph of PEEK CMM 10h.

After characterization of the individual materials in powder form that make up the PC-PEEK system in this study, attention was turned to the characterization and testing of Mixed and Control samples (Chapter 7).

## 7. RESULTS FROM MIXED AND CONTROL SYSTEMS

### 7.1 Characterization of Powders

Mixed powder samples, consisting of a 50/50 volume ratio of Unmilled PC and Unmilled PEEK were characterized via thermogravimetric analysis and differential scanning calorimetry. Particle size characterization was performed on Control samples, consisting of a 50/50 volume ratio of PC and PEEK cryogenically mechanically alloyed for one hour with two milling balls. In addition, these powders were characterized thermally and their microstructure was examined using TEM.

#### 7.1.1 Particle Size Analysis

A representative particle size histogram of the Control sample is shown in Figure 7.1. The mean and median particle size values calculated from three replicates are shown in Table 7.1.

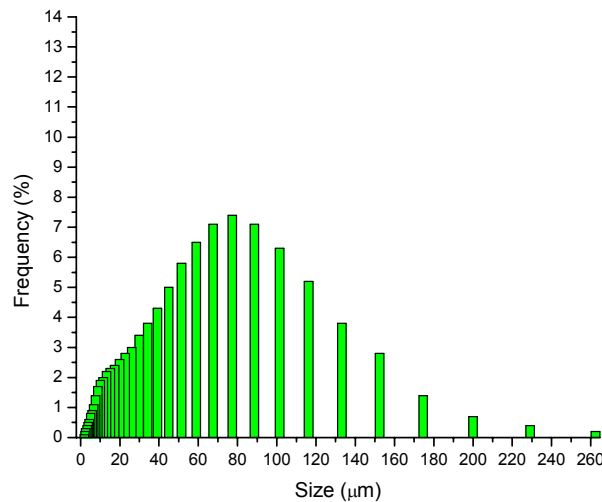


**Figure 7.1:** Particle size histogram for Control sample.

Material	Mean (μm)	Median Particle Size (μm)
Unmilled PC	89.00 ± 4.50	79.40 ± 4.44
Unmilled PEEK	56.26 ± 1.03	46.58 ± 0.57
Control	60.37 ± 0.75	50.30 ± 0.74

**Table 7.1:** Particle size data for Unmilled and Control materials.

The particle size histograms for Control samples indicated a shoulder in the distribution of sizes. Mean particle size values for the CMA 10 h samples are between those of Unmilled PC and Unmilled PEEK.

### 7.1.2 Thermogravimetric Analysis

Typical weight loss vs. temperature data for Unmilled PC, Unmilled PEEK, and Mixed PC-PEEK samples are shown in Figure 7.2 through Figure 7.4 along with derivative curves for each, which were used to define the degradation temperature value for each sample.

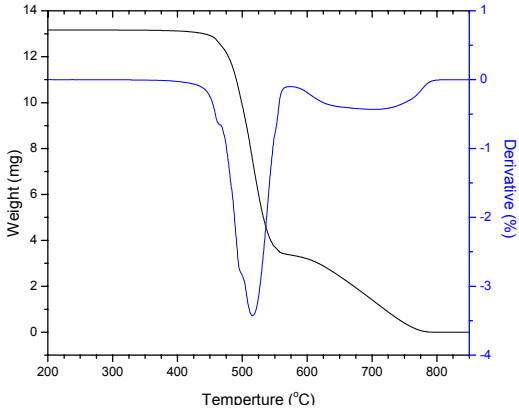


**Figure 7.2:** Unmilled PC TGA raw data and derivative plot.

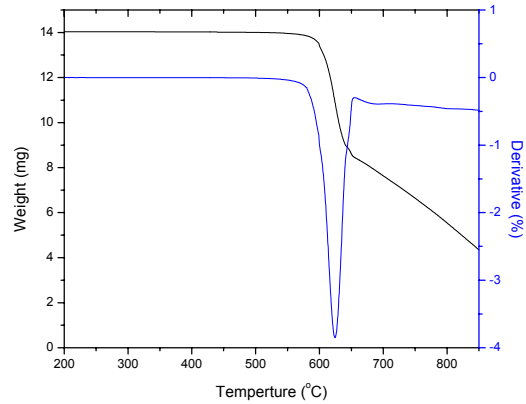


**Figure 7.3:** Unmilled PEEK TGA raw data and derivative plot.

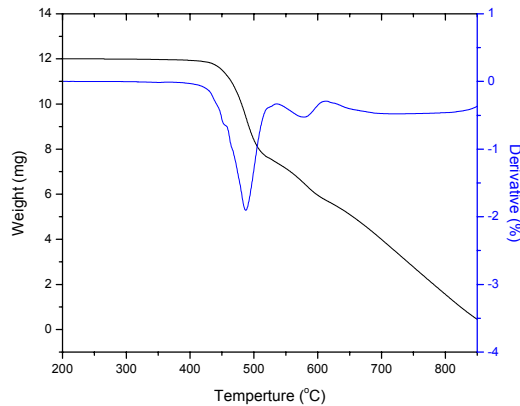


**Figure 7.4:** Mixed sample TGA raw data and derivative plot.

The derivative plot for the Mixed sample exhibits two separate peaks, one corresponding to the degradation of PC and one corresponding to degradation of PEEK in the sample. Degradation temperatures for Mixed and Control samples are shown in Figure 7.5. The values shown are the temperatures

corresponding to the peak in the derivative of the weight vs. temperature curve and represent the average value from three experiments, shown with standard deviation error bars.

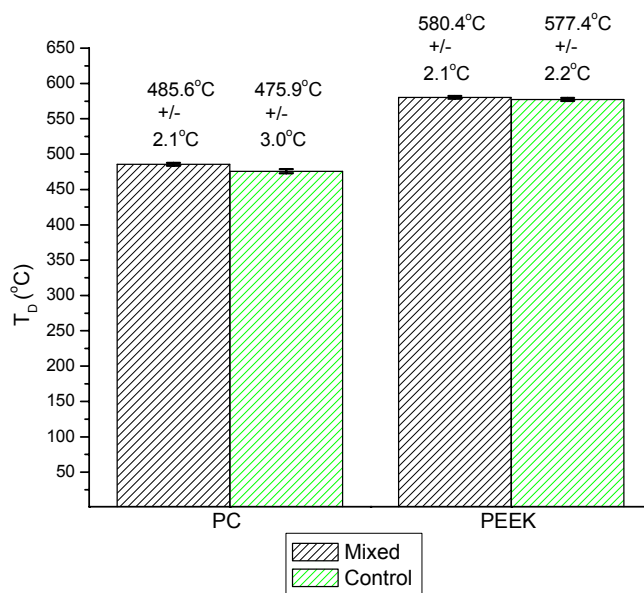


**Figure 7.5:** Degradation temperatures measured for Mixed and Control samples.

The  $T_D$  values measured for PEEK in the Mixed and Control samples are not significantly different. The  $T_D$  value of PC is slightly lower for the Control sample compared to the Mixed sample. The degradation temperatures of each component in both of these systems are significantly lower than those measured in tests of the Unmilled materials ( $T_{D,PC}=517.9\pm 2.5^\circ\text{C}$ ,  $T_{D,PEEK}=623.7\pm 1.6^\circ\text{C}$ ), however, indicating that the presence of PEEK accelerates the degradation temperature of PC and vice versa.

### 7.1.3 Differential Scanning Calorimetry

Differential scanning calorimetry tests were performed on Mixed and Control samples. Following the first heat, samples were allowed to cool to room temperature and a second heat was performed. Raw data is shown in Figure 7.6.

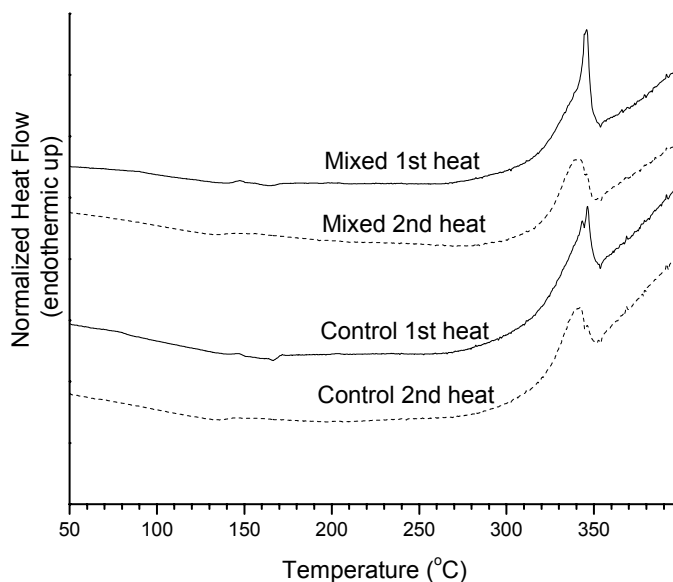


**Figure 7.6:** DSC curves performed at 10°C/minute for Mixed and Control samples. Curves have been shifted vertically for comparison.

As expected, crystallization peaks are smaller in Mixed and Control samples compared to PEEK samples, because the Mixed and Control samples consist of 50% PEEK by volume. No crystallization peaks are present in the curves corresponding to the second heating, as PEEK phase of the samples becomes fully crystalline upon cooling from melt. The melt peak (reflecting melting of the PEEK phase in each sample) is different for Control samples compared to Mixed samples; the Control samples exhibit a double melting peak, while the Mixed samples exhibit a single melting peak.

#### 7.1.4 Transmission Electron Microscopy

Transmission electron micrographs of Control powder particle cross-sections are shown in Figure 7.7.

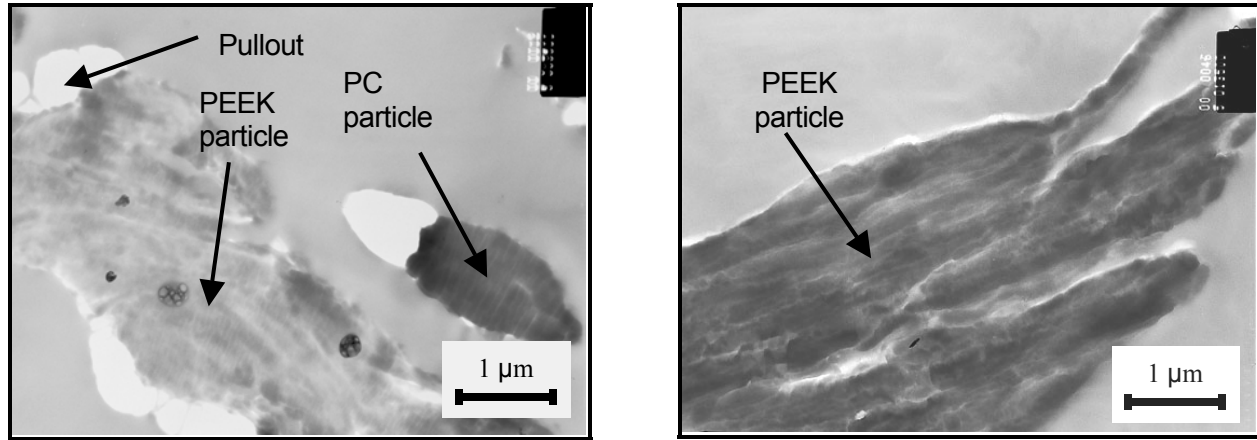


**Figure 7.7:** TEM micrographs of Control powder particles.

An examination of these micrographs reveals that processing this PC-PEEK system under Control conditions (cryogenic temperature for 1 hour with 2 milling balls) does not result in powder particles that consist of two phases, but rather results in particles whose microstructure is not drastically altered from their unmilled state.

These results lead to the designation of this system as the Control system. The thermal properties are not significantly different than those of the Mixed system, and each particle does not consist of two phases. The Control particles do not exhibit microstructures very different than those of the initial components, yet some differences may exist due to exposure to milling media and cryogenic temperature, which may result in changes in particle size and surface area in CMA 10h powders. The aim of selecting this system as a control is to separate the effects of initial microstructure prior to injection molding into test bars from any potential effects caused by mechanical processing in the ball mill. By comparing the CMA 10h sample to the Control sample, any differences observed will be the result of changing milling parameters, not simply exposure to cryogenic temperature, the ball mill, or milling media. So far, results have been reported for the Mixed and Control systems in the powder state. In order to investigate the mechanical properties and morphology of parts made from these powders, the powders were injection molded into coupons, each consisting of four bars suitable for testing.

## 7.2 Testing Molded Bars

After heating the Mixed and Control samples in the injection molder barrel for 5 minutes at 350°C, these samples did not flow well enough to completely fill the mold during every shot. The 360°C injection molded samples also had problems filling the mold, although this temperature seemed to improve the flow of materials. Visual inspection determined that 370°C was the lowest molding temperature that would fill the mold well every time for these systems, consistently producing quality coupons for testing. During heating and molding at 390°C, smoke was observed rising up from the barrel, accompanied by a strong odor. Sample coupons processed at 390°C showed black areas on the surface indicating degradation. The smoke and odor were observed during molding of Unmilled PC but not during molding of Unmilled PEEK at the same temperature. It was therefore assumed that these occurrences during molding of the Mixed and Control samples were due to thermal degradation of the PC phase in the Mixed and Control samples.

Because the polymer was injected into a room-temperature mold, a skin-core morphology developed for samples molded at 370°C and higher. Below 370°C, the crystalline portion of the semi-crystalline PEEK phase did not fully melt, and the molded coupons had a chalky appearance, with visible agglomerations of powder. Coupons molded at 370°C appeared darker (like the Unmilled PEEK coupons) and the skin-morphology was visible upon fracture, with the outer “skin” of the bars being quenched into a translucent-looking skin as it was quickly cooled in the room temperature mold. The PEEK phase present in the inner “core” is likely semi-crystalline, as this material cooled more slowly, allowing crystallization to occur from the melt.

### 7.2.1 Differential Scanning Calorimetry

DSC tests were performed on bars injection molded at 350°C, 360°C, and 370°C from Mixed and Control samples. Results from the first and second heating are shown in Figure 7.8.

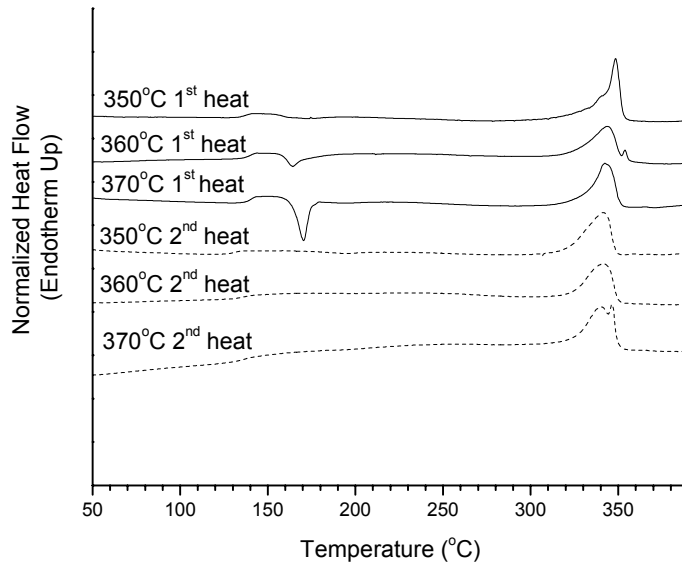


**Figure 7.8:** DSC curves performed at 10°C/minute for injection molded bars Control samples. Curves have been shifted vertically for comparison.

Bars molded at 350°C do not exhibit a crystallization peak during the first heat scan in the DSC. The lack of crystallization upon heating means that the samples are fully crystalline prior to the DSC test. If melting had been achieved during the molding process, one would expect a crystallization peak to be present in subsequent DSC first heats because some of the melted crystals would be quenched in the molding process. Bars molded at 360°C and 370°C exhibit a crystallization peak during the first heat scan in the DSC. The presence of a crystallization peak in bars molded at 360°C indicates that, during heating in the barrel, PEEK crystals were at least partially melted and partially quenched during molding. The crystallization endotherm is larger for bars molded at 370°C, indicating that more melting took place in the molding process for samples molded at 370°C compared to those molded at 360°C. This result is confirmed by the appearance of the molded bars; samples molded at 370°C and above exhibited skin-core morphology. Crystallization peaks are not present in second heat scans of any samples because the samples fully crystallize as they are cooled to room temperature between tests.

## 7.2.2 Dynamic Mechanical Analysis

Representative isochronal DMA results are shown in Figure 7.9 through Figure 7.18. Storage modulus and loss modulus are plotted as a function of temperature for Mixed and Control samples. Inner (i) and outer (o) bars were tested from the same injection molding shot, along with replicates of each injection molding condition. As bars were heated during the DMA test, a residual stress caused a shoulder or peak in storage modulus (for example, Figure 7.13). As the material goes through its glass transition, the storage modulus decreases as the material softens. After the glass transition is complete, the material flows under the weight of the probe (therefore changing dimensions), and the sample becomes indented. Because the DMA was employed with constant displacement controls, the machine compensates by applying less force as the material flows under the probe, making the material appear “stiffer” to the machine and causing reported modulus values to increase at high temperatures.

### 7.2.2.1 Sample Effects- Inner vs. Outer bars, Mixed vs. Control Samples

Dynamic mechanical data was recorded for coupons molded at each injection molding temperature. Storage modulus curves for bars molded at 350°C are shown in Figure 7.9. Loss modulus curves for bars molded at 350°C are shown in Figure 7.10.

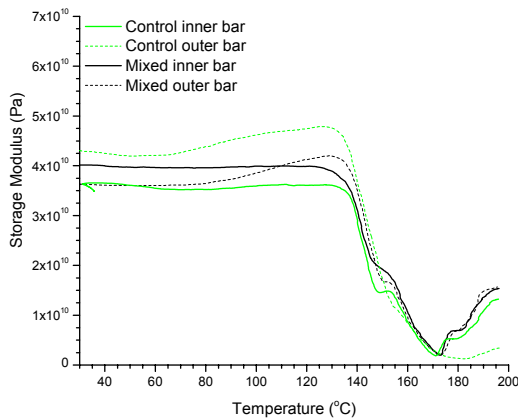


**Figure 7.9:** Representative storage modulus curves for Mixed and Control samples injection molded at 350°C.

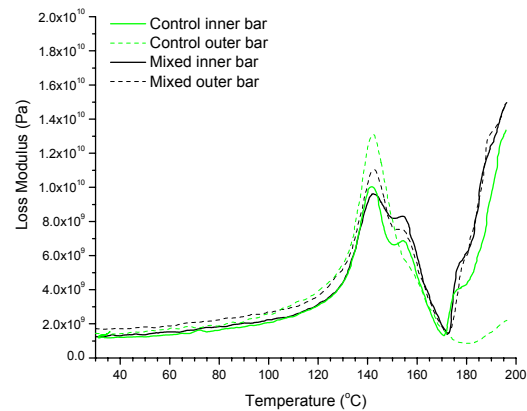


**Figure 7.10:** Representative loss modulus curves for Mixed and Control samples injection molded at 350°C.

For these samples, the outer bars exhibit a shoulder in the storage modulus, while the inner bars do not display a shoulder (Figure 7.9). Modulus differences between sample sets or replicates within one set may exist due to dimensional variations within coupons. In addition, some experimental error may exist from taring (zeroing) the probe weight prior to starting the test.

A peak in the loss modulus is generally considered to represent the glass transition of a viscoelastic material, and can be used as a measure of a material's  $T_g$ . A two-phase material would usually be expected to exhibit two peaks (or a double peak) in the loss modulus. In the case of PEEK and PC, the glass transitions are so close together that, depending upon the time scale of the experiment, two separate peaks may not be revealed. There is an additional shoulder present in the drop of the storage modulus at approximately 155°C that also is revealed as a double peak or peak with a shoulder in the loss modulus (Figure 7.10). In addition to this double peak in the loss modulus, it is noted that the loss peak for Mixed and Control samples have similar magnitudes. Representative storage and loss modulus curves for samples injection molded at 360°C are shown in Figure 7.11 and Figure 7.12.

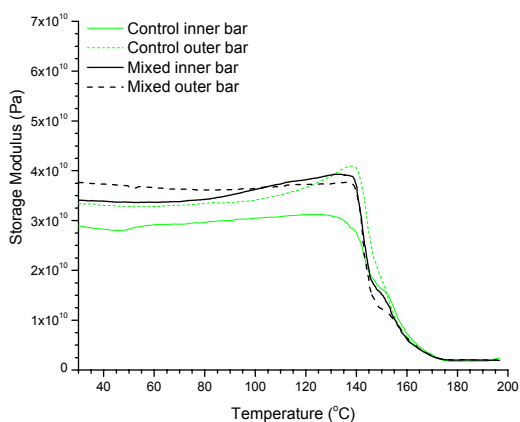


**Figure 7.11:** Representative storage modulus curves for Mixed and Control samples injection molded at 360°C.

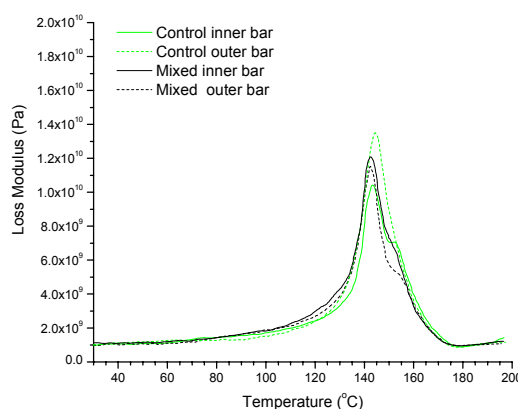


**Figure 7.12:** Representative loss modulus curves for Mixed and Control samples injection molded at 360°C.

Like the bars molded at 350°C, a double peak is exhibited in the loss modulus for samples molded at 360°C. A small shoulder is exhibited during the glass transition of the storage modulus in the bars molded at

360°C. Storage and loss modulus curves for samples injection molded at 370°C are shown in Figure 7.13 and Figure 7.14.

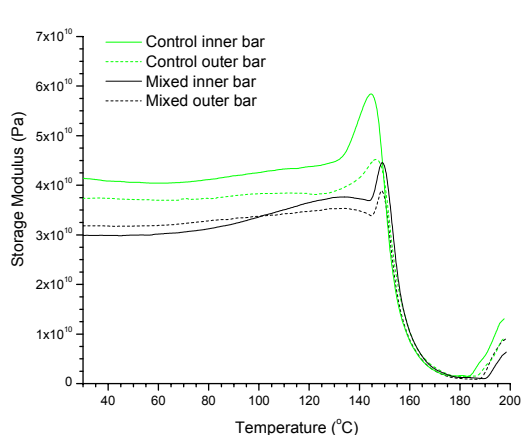


**Figure 7.13:** Representative storage modulus curves for Mixed and Control samples injection molded at 370°C.

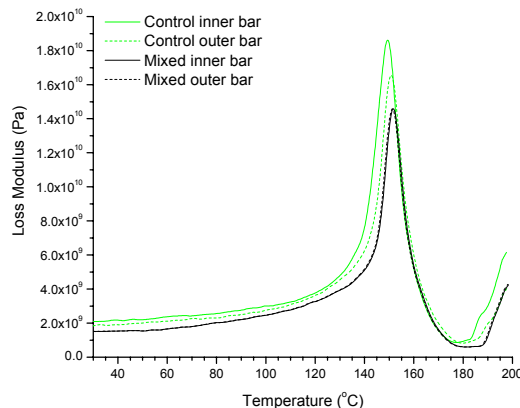


**Figure 7.14:** Representative loss modulus curves for Mixed and Control samples injection molded at 370°C.

While samples molded at 350°C and 360°C exhibit a shoulder in the storage modulus, samples molded at 370°C exhibit a peak prior to the decrease in storage modulus during the glass transition. Additionally, the loss curves exhibit a single peak for all samples molded at 370°C, with the peak located at a temperature in between the double peaks in the 350°C and 360°C samples. Likewise, no small shoulder exists in the storage modulus during the glass transition. Additional tests of the samples molded at 370°C performed at a slower rate (2°C/minute) indicate a lower  $T_g$  (133.1°C at 2°C/minute vs. 135.5°C at 10°C/minute), as expected. Dynamic mechanical data for Mixed samples molded at 380°C are not reported due to machine malfunction. Figure 7.15 and Figure 7.16 show representative storage and loss modulus curves for bars molded at 380°C.

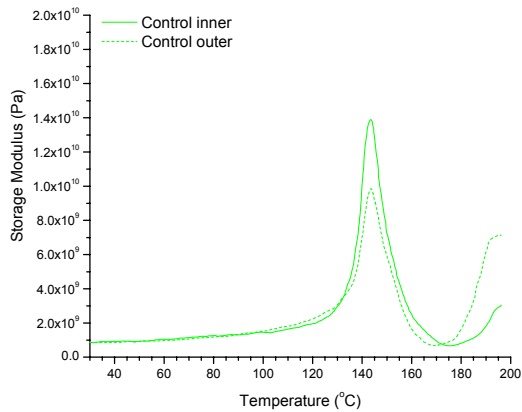


**Figure 7.15:** Representative storage modulus curves for Control samples injection molded at 380°C.

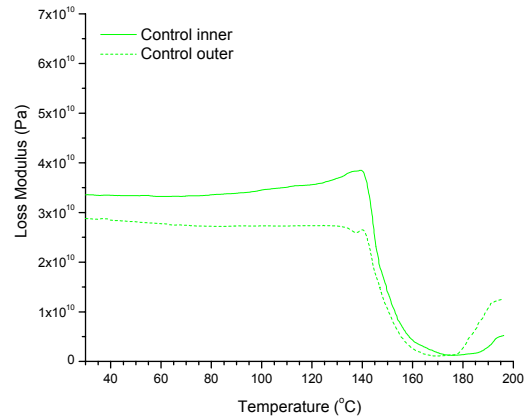


**Figure 7.16:** Representative loss modulus curves for Control samples injection molded at 380°C.

The peak present in the storage modulus of the Mixed and Control bars molded at 370°C appears as a shoulder for bars molded at 380°C. As with the 370°C samples, a single loss peak is observed in samples molded at 380°C. Representative storage and loss modulus curves for samples injection molded at 390°C are shown in Figure 7.17 and Figure 7.18.

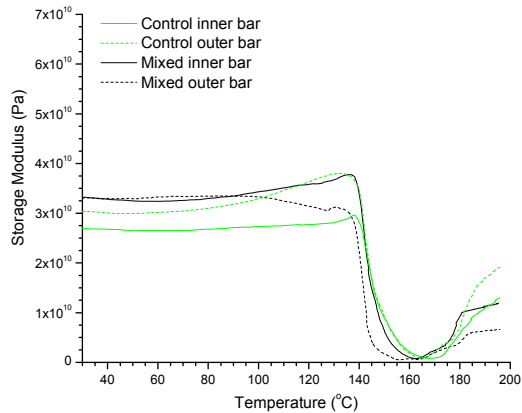


**Figure 7.17:** Representative storage modulus curves for Mixed and Control samples injection molded at 390°C.

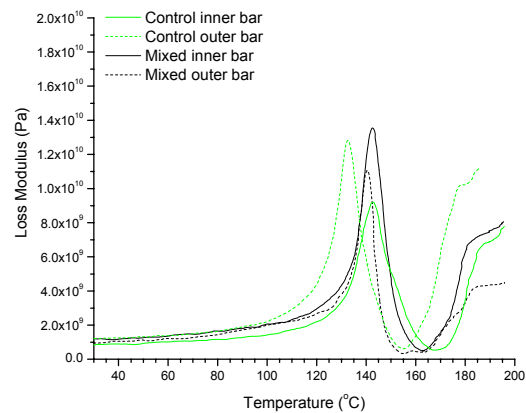


**Figure 7.18:** Representative loss modulus curves for Mixed and Control samples injection molded at 390°C.

For samples molded at 390°C, a shoulder exists in the storage modulus prior to the glass transition, indicating a relaxation in these samples as they are heated during the test. While the storage modulus curves look similar for each sample, the loss modulus curves exhibit peaks at a variety of temperatures and

magnitudes. This variation is possibly due to degradation of material during molding at this upper limit temperature.

These data show that some differences between inner and outer bars exist, especially at 350°C and 360°C molding temperatures; therefore, inner vs. outer bars will be distinguished in subsequent measurements. Differences observed between Mixed and Control samples as well as inner vs. outer bars diminish at molding temperatures of 370°C and above, when the material flows well enough to easily fill the mold during processing.

#### *7.2.2.2 Effect of Injection Molding Temperature on Loss Modulus Peak ( $T_g$ )*

To examine the effect of injection molding temperature on the loss modulus peak associated with the glass transition temperature, loss modulus curves are plotted below for each sample type, with bars molded at various injection molding temperatures shown on the same plot (Figure 7.19-Figure 7.22). Data for Mixed and Control samples molded at 370°C and for Mixed samples molded at 380°C are not reported due to machine malfunction.

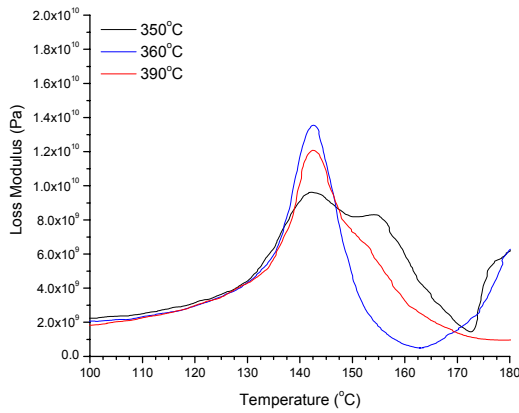


**Figure 7.19:** Mixed inner samples Loss modulus curves.

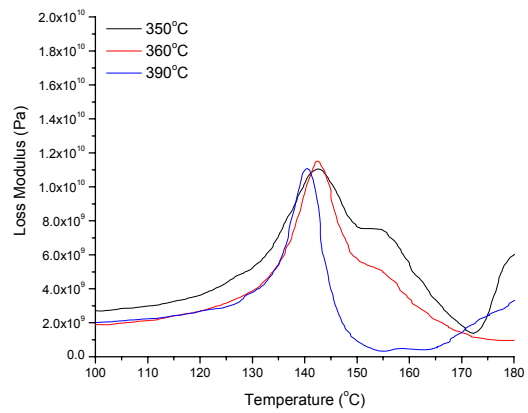


**Figure 7.20:** Mixed outer samples Loss modulus curves.

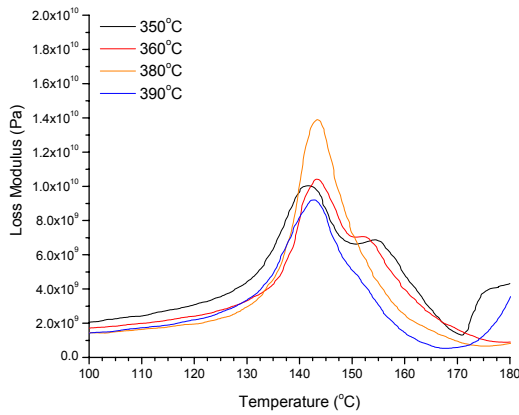


**Figure 7.21:** Control inner samples Loss modulus curves.

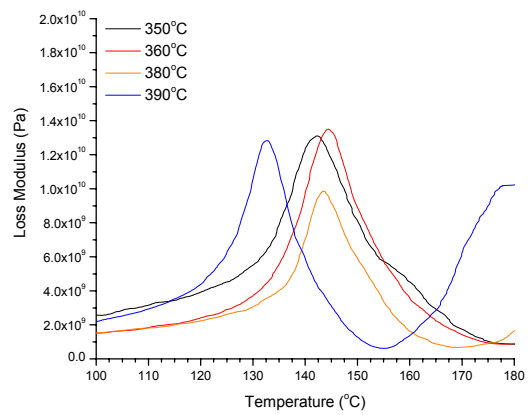


**Figure 7.22:** Control outer samples Loss modulus curves.

For Mixed inner bars, a double peak exists in the bar molded at 350°C. For the Mixed bar molded at 360°C, the double peak is present but less pronounced. The Mixed bars molded at 380°C and 390°C exhibit a single peak. The same trend is seen for the Mixed outer samples. The Control inner bars exhibit double peaks for samples molded at 350°C, 360°C, and a peak with a shoulder for the sample molded at 390°C. The Control outer samples are the most varied, exhibiting peaks at varying temperatures.

### 7.2.3 Quasi-Static Three-Point Bend Testing

Three replicates of inner and outer bars were tested using the TA.XT2i in 3-point bend mode at 0.1mm/s. The resulting stress/strain plots for all replicates are shown in Figure 7.23 through Figure 7.32. Results are plotted to 40% strain, at which point the test was stopped.

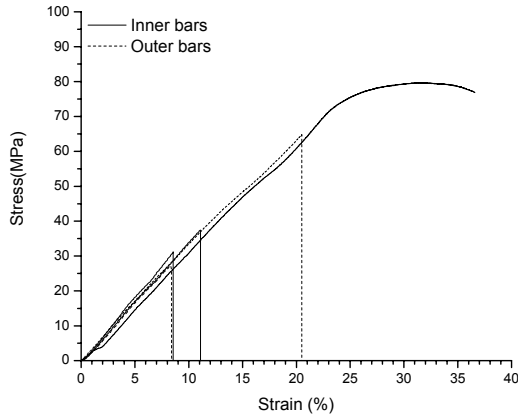


**Figure 7.23:** 3-point bend data for replicate Mixed samples injection molded at 350°C.

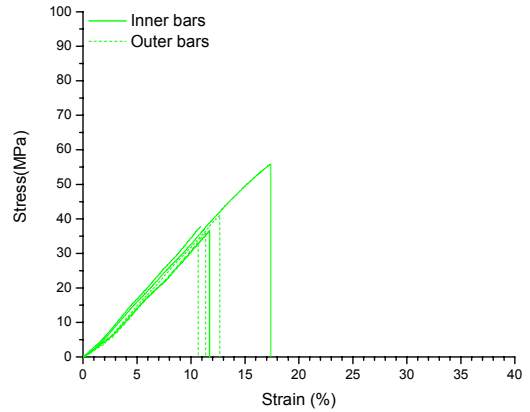


**Figure 7.24:** 3-point bend data for replicate Control samples injection molded at 350°C.

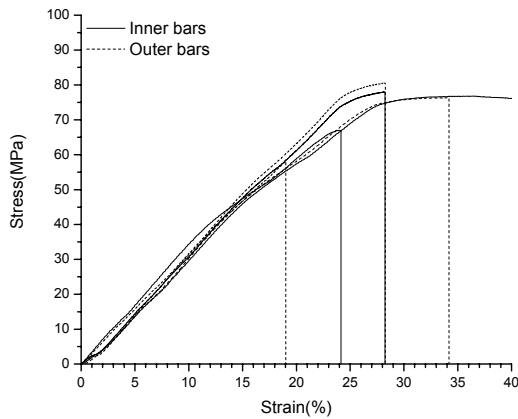


**Figure 7.25:** 3-point bend data for replicate Mixed samples injection molded at 360°C.

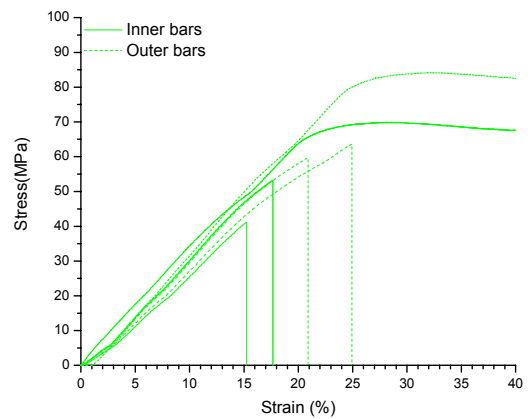


**Figure 7.26:** 3-point bend data for replicate Control samples injection molded at 360°C.

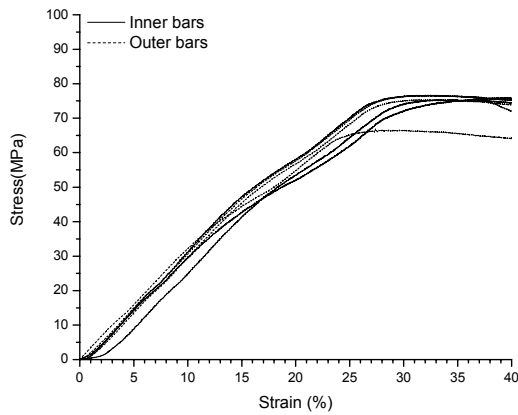


**Figure 7.27:** 3-point bend data for replicate Mixed samples injection molded at 370°C.

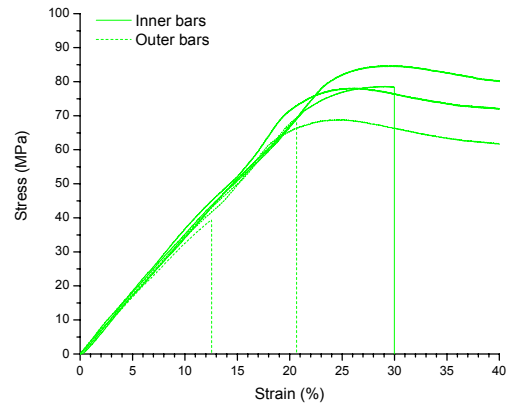


**Figure 7.28:** 3-point bend data for replicate Control samples injection molded at 370°C.

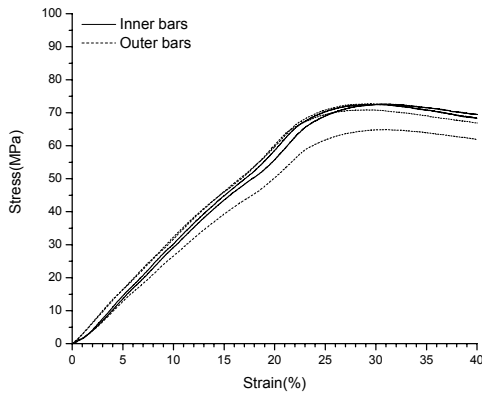


**Figure 7.29:** 3-point bend data for replicate Mixed samples injection molded at 380°C.

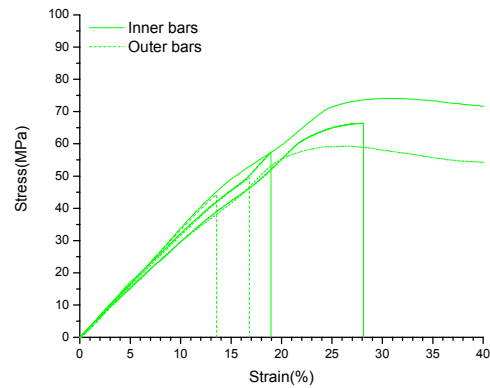


**Figure 7.30:** 3-point bend data for replicate Control samples injection molded at 380°C.

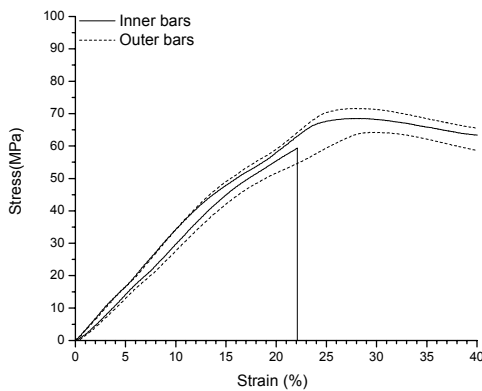


**Figure 7.31:** 3-point bend data for replicate Mixed samples injection molded at 390°C.

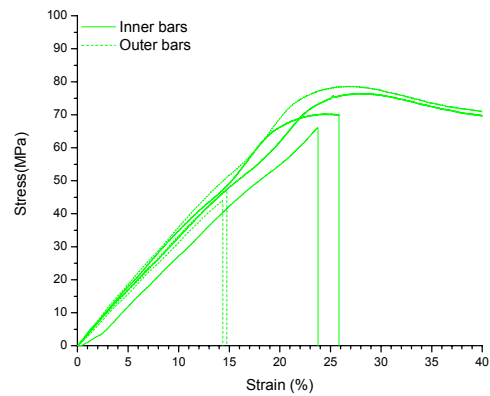


**Figure 7.32:** 3-point bend data for replicate Control samples injection molded at 390°C.

Energy to break values were calculated by integrating the area under the stress-strain curves to fracture or 40% strain, whichever occurred first. Values obtained for Mixed and Control samples at each injection molding temperature are shown in Figure 7.33. Bars that did not break during this test actually have a higher energy to break, strength, and strain to break than is reported because the test was stopped at 40%. For samples where this occurred to most of the bars tested, this is indicated by an arrow next to the plotted point. Standard deviation for each sample is shown as error bars. Because the load distribution in the 3-point bend test results in a point stress concentration in the sample, any flaw resultant from molding may greatly influence the probability of failure. The scatter exhibited by the data is therefore higher than might be the case for a tensile test, which distributes the load over the entire sample cross-section.

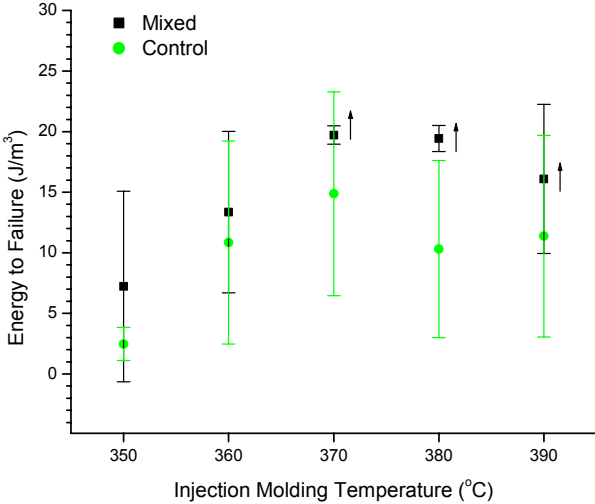


**Figure 7.33:** Energy to failure values calculated from 3-point bend data. Arrows indicate samples where actual values are higher than measured values because the test was stopped at 40% strain.

Failure strength values (defined as the measured strength at either fracture or 40% strain when the test was stopped) were determined from each stress-strain plot, and are shown in Figure 7.34. The standard deviation for each sample is shown as error bars. Strain at failure values are shown in Figure 7.35.

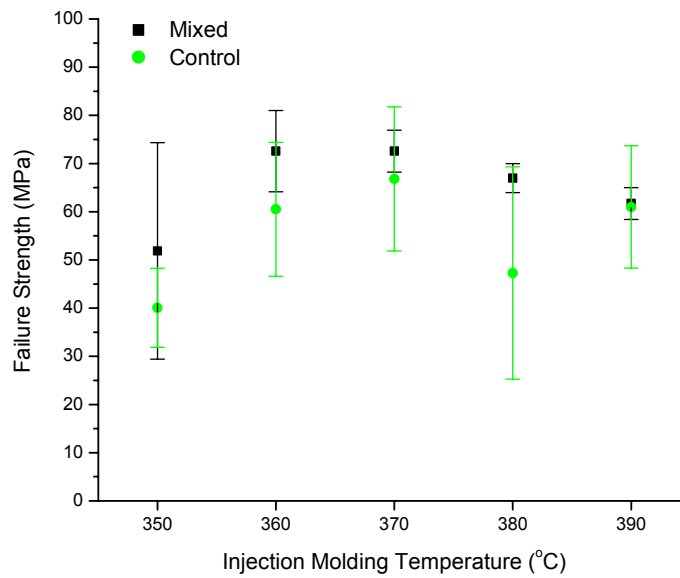


**Figure 7.34:** Failure strength values determined from 3-point bend data.

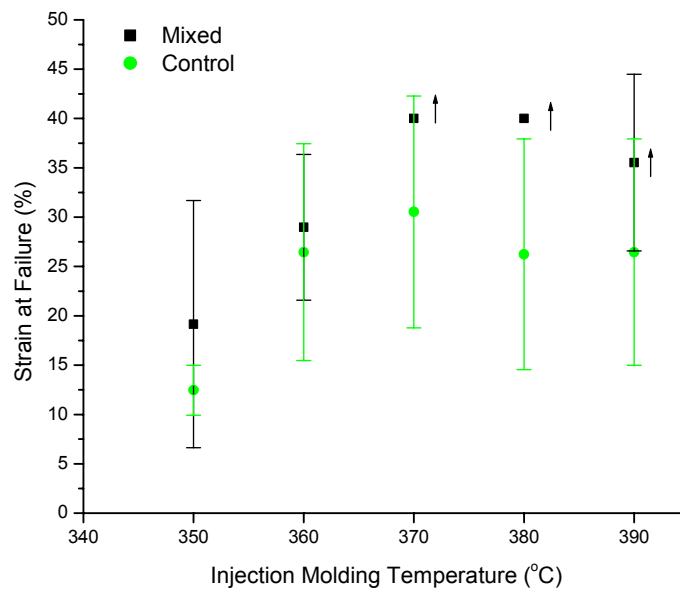


**Figure 7.35:** Strain at failure values determined from 3-point bend data. Arrows indicate samples where actual values are higher than measured values because the test was stopped at 40% strain.

As injection molding temperature increases from 350°C to 360°C, the energy to break (area under stress-strain curve) of the Mixed and Control samples increases. These data supports the observation that it is easier to fill the mold at 360°C than 350°C due to improved flow. Average energy to break values are

equivalent for molding temperatures of 360°C and above. Comparing the Mixed and Control samples, the Mixed samples have somewhat higher energy to break and strain at failure values. Statistical T-tests on the two populations at each molding temperature revealed that differences in measured energy to break and strain at failure values were only significant at 380°C, where Mixed samples exhibited notably more ductile behavior. Note that some failure strain data points do not show error bars for Mixed samples, as the test was stopped for each of these samples at 40% strain before the sample fractured.

The effect of molding temperature on mechanical properties is evident from examination of these data. Mixed and Control samples become more ductile (increased elongation at break) as molding temperature is increased from 350°C to 370°C. At 360°C, the polymer barely filled the mold, often resulting in short shots; it was even more difficult to fill the mold at 350°C. At molding temperatures of 370°C and above, the polymer flowed as the PEEK melted, generally producing samples that, when tested, exhibited ductile behavior and continued to elongate until the sample slid down into the fixture and the test stopped. For the 350°C molding condition, the Mixed and Control samples demonstrated very similar brittle behavior. At molding temperature of 360°C, the Control samples exhibited more brittle behavior than the Mixed samples, breaking before yield. Unlike the results from 3-point bend dynamic mechanical testing, the results from static mechanical testing (with a similar span width) do not reveal differences in inner and outer bars. After mechanical testing was completed, the fracture surfaces of the Control samples were imaged via scanning electron microscopy and a microtomed surface was cut from the center of the bar for morphology examination with the atomic force microscope.

### 7.3 Imaging Molded Bars

The morphology of Control bars molded at 350°C, 370°C, and 390°C was imaged using TappingMode™ atomic force microscopy. Representative micrographs taken from the center of each bar are shown in Figure 7.36.

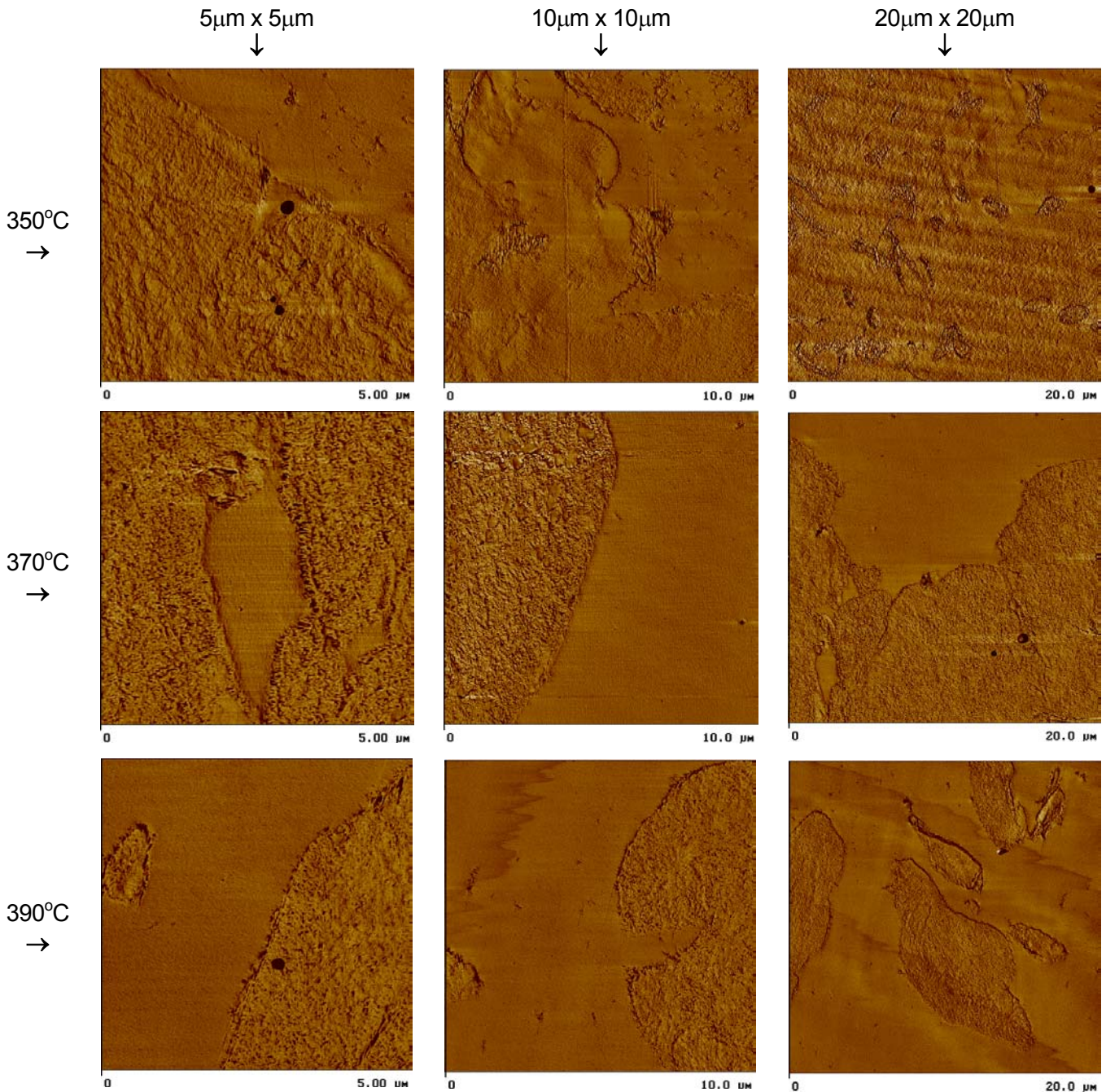


**Figure 7.36:** AFM images of injection molded Control bars.

The two phases are readily distinguishable: the amorphous PC appears featureless in the phase-image AFM mode, while the semi-crystalline appears “rough.” These micrographs show agglomerations of PEEK within a PC matrix. It appears that the PC is able to flow around the semi-crystalline PEEK phase at these molding temperatures, as would be expected from molding 200°C above the  $T_g$  of PC. An examination of these micrographs leads to the following observations: bars molded at 350°C contain areas of both PEEK and PC within the PC matrix or areas of PEEK which contain both semi-crystalline and amorphous regions. At this temperature, it is believed that the PEEK does not flow easily, as the crystals are not completely melted, hindering flow of both the PEEK phase and some of the PC phase. Bars molded at 370°C appear to consist of a PC matrix containing PEEK phases with some PC areas trapped inside. It is believed that the PEEK phase becomes molten at this temperature and flows easily. The bar molded at 390°C shows PEEK phases in a PC matrix.

## **7.4 Imaging Tested Bars**

### **7.4.1 Scanning Electron Microscopy**

Fracture surfaces of samples tested in 3-point bend mode at 0.1mm/s using the TA.XT2i were imaged at three magnifications using scanning electron microscopy and are shown in Figure 7.37. The skin-core morphology is visible in the lowest magnification micrographs. Bars injection molded at each temperature are shown in rows, with the scales shown above each column.

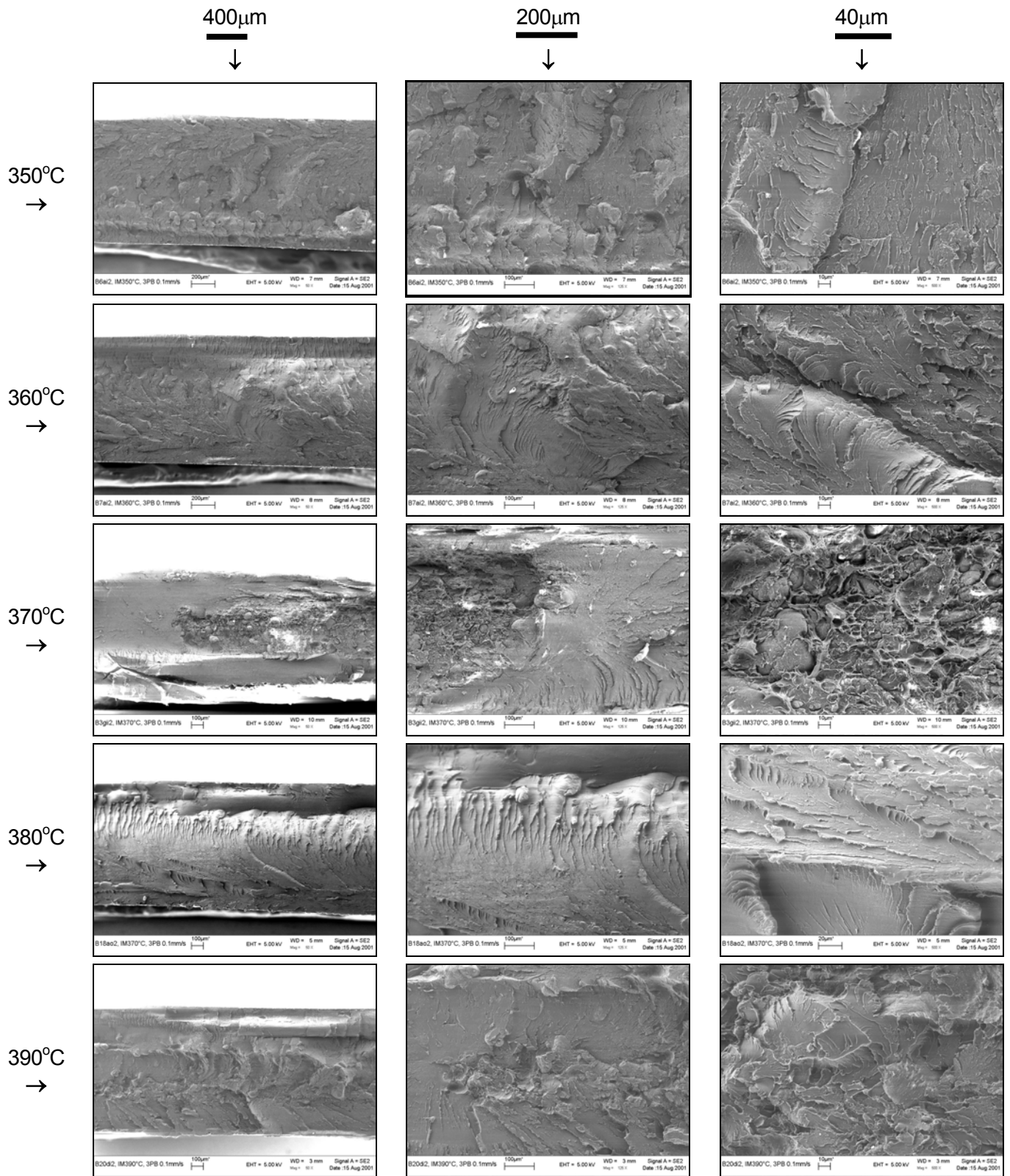


**Figure 7.37:** SEM micrographs of Control fracture surfaces tested at 0.1mm/s.

The most notable observation is that the center of the 370°C bar appears to have fractured in a ductile manner, with particles visible within the matrix.

## 7.5 Testing Annealed Bars

Mixed and Control bars were annealed to determine if the relaxations present in the storage modulus plots of the dynamical mechanical tests could be erased by holding the bars at a temperature above  $T_g$  for a short time. In general, as a polymer ages, the free volume of a polymer decreases. Annealing above the polymer's  $T_g$  speeds the process, and possibly allows residual stresses or relaxations present in a sample to be relieved by annealing. In addition, annealing a polymer blend may cause thermodynamic demixing to occur as the polymer chains gain mobility to overcome being trapped in a non-equilibrium arrangement.

### 7.5.1 Dynamic Mechanical Analysis

Storage and loss modulus DMA results are plotted in the same figure for annealed and as-molded bars in Figure 7.38 through Figure 7.44. Mixed samples are shown in the first column, and Control samples are shown in the second column.

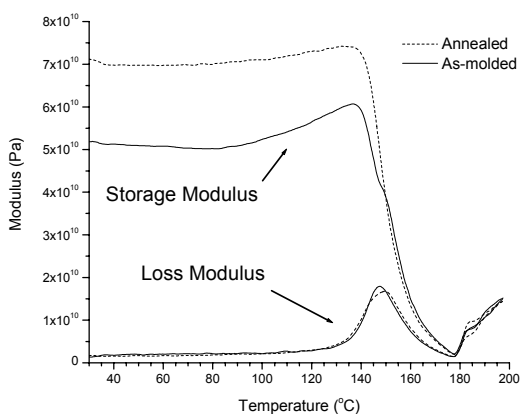


**Figure 7.38:** Annealed (dotted) vs. as-molded (solid) Mixed samples, molded at 350°C.

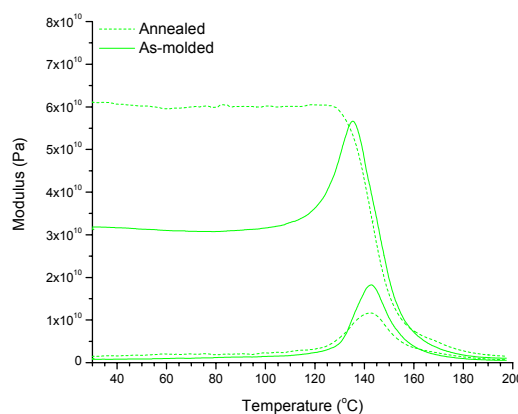


**Figure 7.39:** Annealed (dotted) vs. as-molded (solid) Control samples, molded at 350°C.

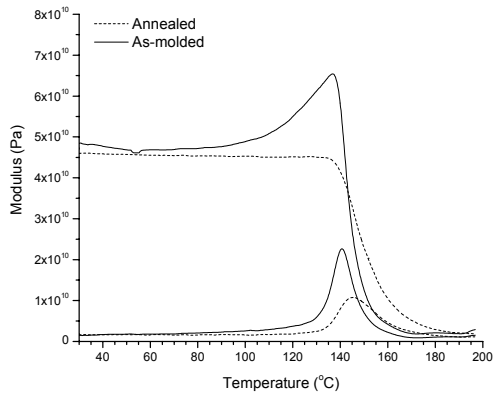


**Figure 7.40:** Annealed (dotted) vs. as-molded (solid) Mixed samples, molded at 360°C.

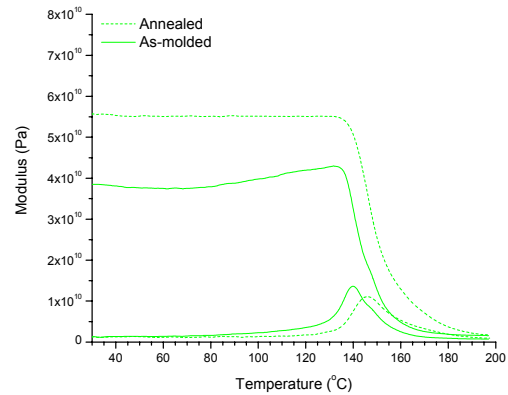


**Figure 7.41:** Annealed (dotted) vs. as-molded (solid) Control samples, molded at 360°C.

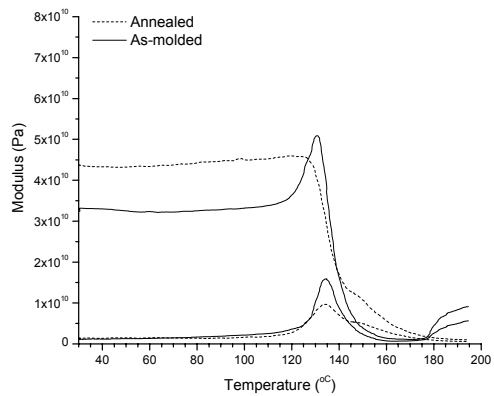


**Figure 7.42:** Annealed (dotted) vs. as-molded (solid) Mixed samples, molded at 370°C

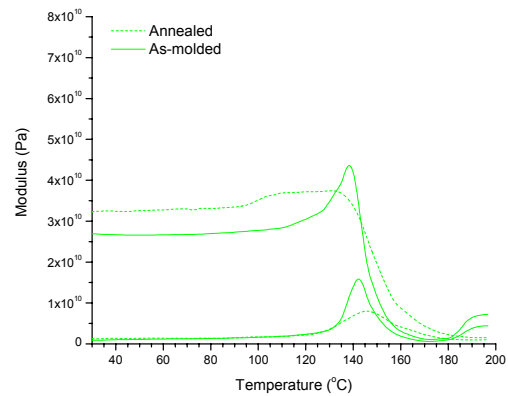


**Figure 7.43:** Annealed (dotted) vs. as-molded (solid) Control samples, molded at 370°C

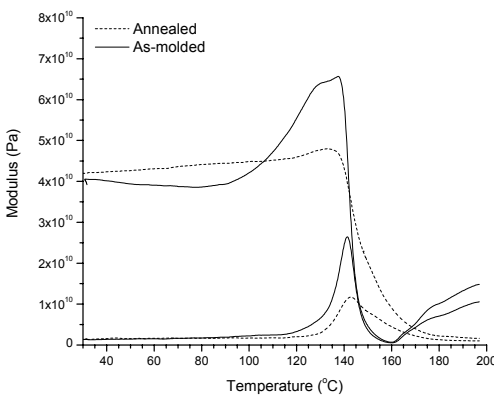


**Figure 7.44:** Annealed (dotted) vs. as-molded (solid) Mixed samples, molded at 390°C.

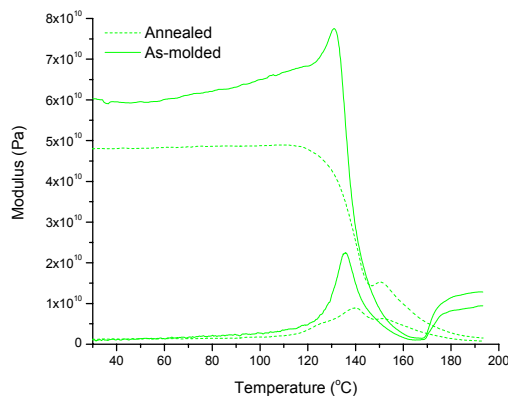


**Figure 7.45:** Annealed (dotted) vs. as-molded (solid) Control samples, molded at 390°C.

Perhaps the most notable feature of the annealed samples is the lessening or complete disappearance of a shoulder or peak in the storage modulus prior to the glass transition. This effect implies that annealing molded bars just above  $T_g$  for 20 minutes prior to DMA testing gives the system sufficient energy to erase the relaxation that occurs in as-molded bars. The annealed bars for Mixed samples generally exhibited a higher storage modulus than as-molded bars, with the exception of the Mixed bars molded at 360°C and 390°C, for which the annealed and as-molded samples exhibit approximately the same initial storage modulus values. Annealed Control bars generally exhibited higher initial storage modulus than as-molded Control bars. The shape of storage modulus peak in as-molded bars is a combination of at least two factors: a stiffness change that occurs prior to the glass transition, and the drop in the modulus as the transition occurs at similar temperatures.

In general, the loss modulus peaks of annealed bars appear at the same or higher temperature as the as-molded bars, and are broader (both wider and smaller in magnitude) than the corresponding peaks in loss modulus of as-molded bars. The Mixed bar molded at 350°C showed no change in the temperature at which the loss modulus peak occurred ( $T_g$ ), although the bars molded at higher temperatures showed an increase in  $T_g$  with annealing. Similarly, the Control samples showed the same trend.

## 8. RESULTS FROM THE CMA 10H SYSTEM

### 8.1 Powder Characterization

#### 8.1.1 Particle Size Analysis

Representative particle size histograms of Unmilled PC and PEEK are shown in Figure 8.1 and Figure 8.2. A histogram is shown for the CMA 10h sample in Figure 8.3. The mean and median particle size values calculated from three replicates are shown in Table 8.1. In addition, mean particle size values are shown graphically in Figure 8.4.

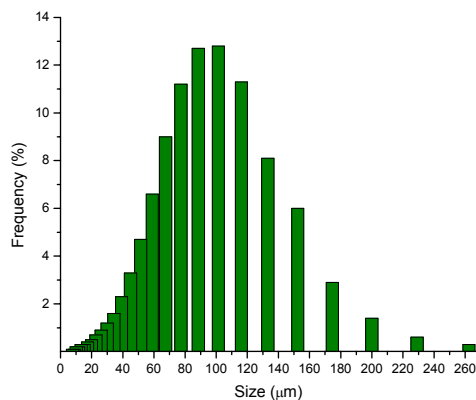


Figure 8.1: Particle size histogram for Unmilled PC.

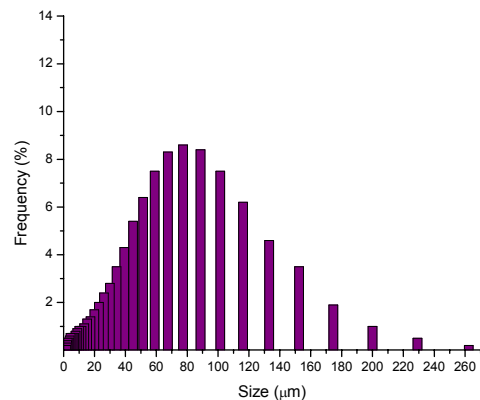


Figure 8.2: Particle size histogram for Unmilled PEEK.

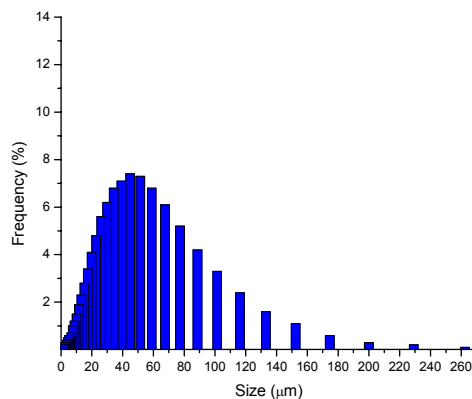
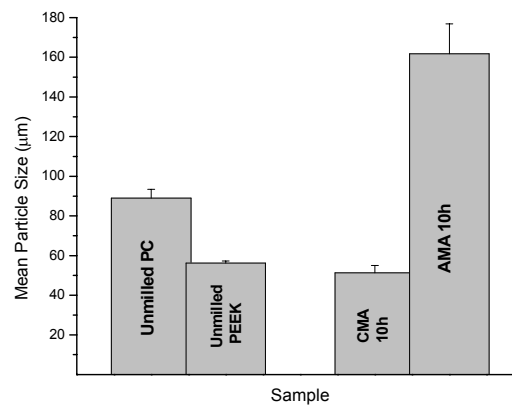


Figure 8.3: Particle size histogram for CMA 10h sample.

Material	Mean ( $\mu\text{m}$ )	Median Particle Size ( $\mu\text{m}$ )
Unmilled PC	$89.00 \pm 4.50$	$79.40 \pm 4.44$
Unmilled PEEK	$56.26 \pm 1.03$	$46.58 \pm 0.57$
CMA PC-PEEK 10h	$51.27 \pm 3.74$	$38.76 \pm 2.39$
AMA PC-PEEK 10h	$161.79 \pm 15.09$	$162.89 \pm 28.67$

**Table 8.1:** Particle size data for Unmilled and mechanically alloyed materials.



**Figure 8.4:** Mean particle size values for Unmilled, CMA 10h and AMA 10h powders.

Mean particle size values for the CMA 10h samples are lower than Unmilled PC and approximately the same as Unmilled PEEK. Mean particle size values for AMA 10h are substantially higher than the Unmilled samples. In fact, the mean particle size may actually be higher than reported because the upper detectable limit of the particle size analyzer is 200  $\mu\text{m}$ . Particle size histograms of the AMA 10h powder varied greatly from sample to sample, probably because the large flake-like particles agglomerated and stuck to the sample holder in the particle size analyzer.

### 8.1.2 Thermogravimetric Analysis

Degradation temperatures of CMA and AMA samples processed up to 10 hours are shown in Figure 8.5 and Figure 8.6. The values shown represent the value of the peak in the derivative of the weight percent vs. temperature curve obtained. Each mechanically alloyed sample exhibited two separate degradation

temperatures, corresponding to each of the components. The lower degradation temperature corresponds to the degradation of the PC phase, and the upper temperature corresponds to the PEEK phase degradation. These values are averages from three experiments, shown with standard deviation error bars.

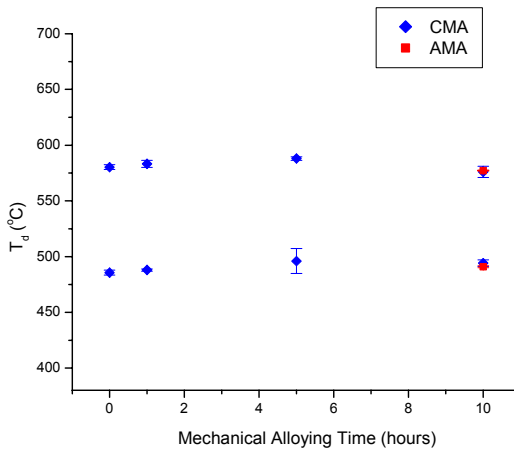


**Figure 8.5:** Effect of mechanical alloying time on degradation temperature of CMA and AMA samples.

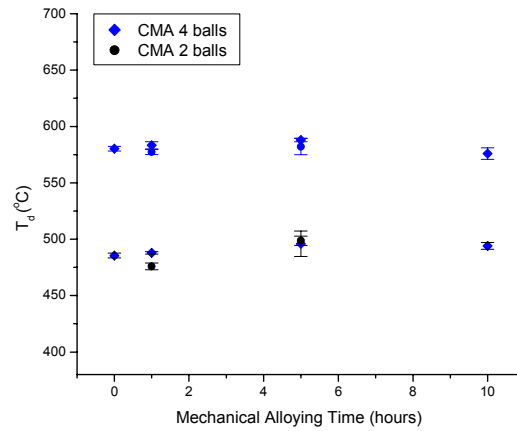


**Figure 8.6:** Effect of number of milling balls (charge ratio) on degradation temperature of CMA samples.

No significant differences in degradation temperatures are observed in samples mechanically alloyed up to 10 hours at either ambient or cryogenic temperatures. The number of milling balls used likewise does not seem to change the measured degradation temperature for the CMA PC-PEEK samples. The values presented here represent the degradation temperature of the samples in a nitrogen environment. Select experiments were also conducted in an air environment. These tests indicated a slightly lower (approximately 20°C) degradation temperature in air due to oxidative degradation.

### 8.1.3 Differential Scanning Calorimetry

Differential scanning calorimetry results for the first and second heats of the CMA 10h sample are shown in Figure 8.7.

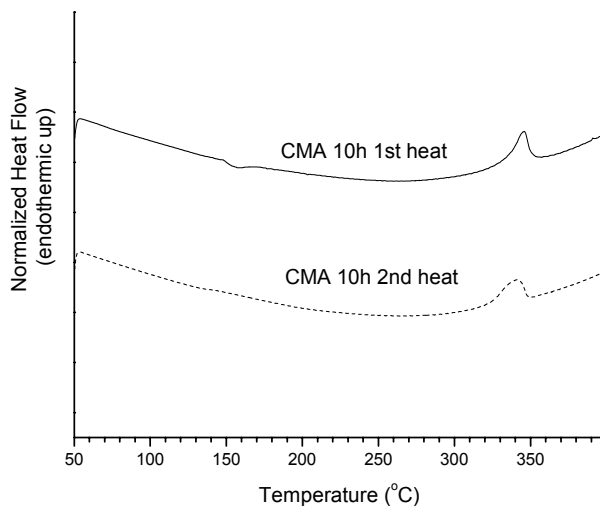


**Figure 8.7:** DSC curves performed at 10°C/minute for the CMA 10h sample. Curves have been shifted vertically for comparison.

Upon heating, the CMA 10h sample exhibits a crystallization peak corresponding to crystallization of the PEEK phase, followed by a single PEEK melting peak. Upon cooling and reheating, a  $T_g$  is observed, followed by a melting peak.

### 8.1.4 Fourier Transform Infrared Spectroscopy

Infrared spectra of CMA 10h powder and Unmilled samples are shown in Figure 8.8 and Figure 8.9. While peak intensity may vary from sample to sample due to variations in powder contact with the stage, no additional peaks are observed in the CMA 10h sample that are lacking in the spectra of the individual components, and no existing peaks from the Unmilled samples disappear in the spectra of the CMA 10h sample.

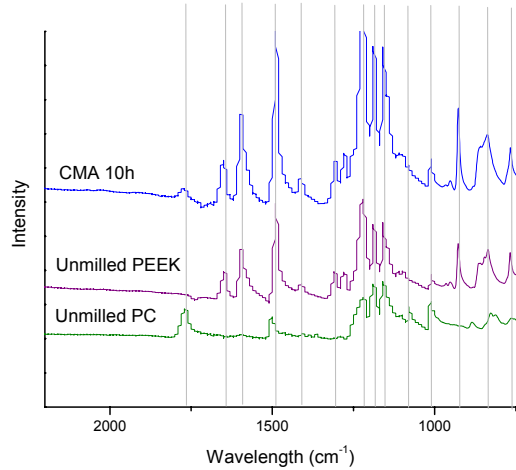


**Figure 8.8:** FTIR spectra of Unmilled and CMA 10h samples. Spectra have been shifted vertically for comparison.

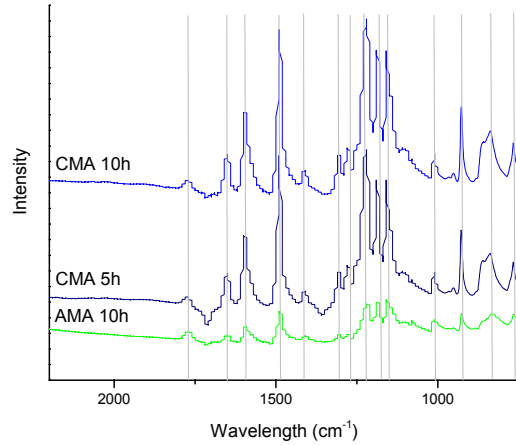


**Figure 8.9:** FTIR spectra of cryogenically and ambiently mechanically alloyed samples. Spectra have been shifted vertically for comparison.

### 8.1.5 Scanning Electron Microscopy

Example micrographs of CMA 10h particles are shown in the Figure 8.10. The micrographs were taken at two magnifications, and 10 $\mu$ m bars are shown for each.

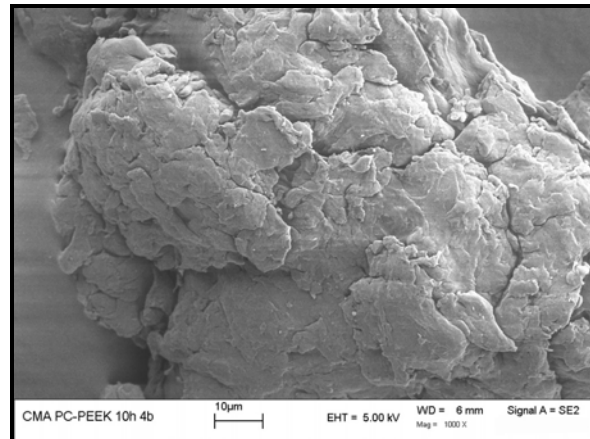
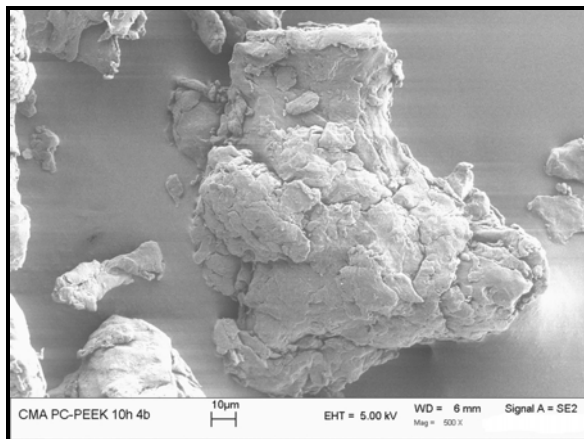


**Figure 8.10:** SEM micrographs of PC-PEEK CMA 10h particles.

The AMA and CMA powders consist of layers of material which have been fractured and then cold welded during the mechanical alloying process, resulting in a layered, flake-like appearance. It is not apparent from these scanning electron micrographs which layers consist of PC and which consist of PEEK.

This differentiation is possible, however, by utilizing transmission electron microscopy and scanning transmission X-ray microscopy.

### 8.1.6 Transmission Electron Microscopy

Transmission electron micrographs of CMA 10h powder particles are shown in Figure 8.11.

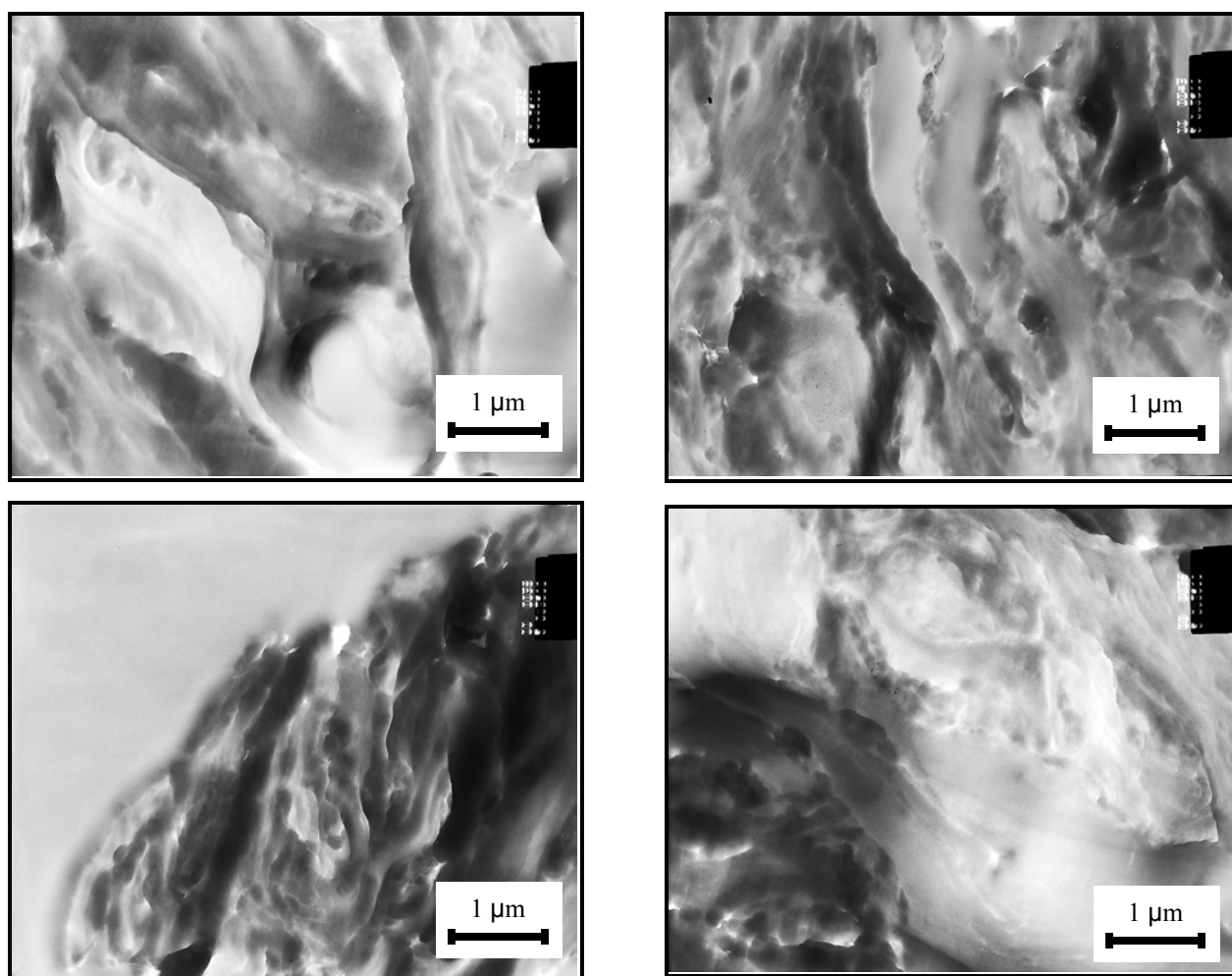


**Figure 8.11:** Transmission electron micrographs of CMA 10h powder.

Darker areas in the cross-sectioned powder particles shown in these micrographs are PEEK-rich phases, whereas PC-rich areas and possibly amorphous regions of PEEK appear lighter because electrons are more easily transmitted through these areas. Upon examination of these micrographs, there is a notable difference between images of CMA 10h powders and the Unmilled or the Control (Figure 7.5) samples, namely the presence of both PC and PEEK within each powder particle, along with the swirled appearance

of the phases, assumed to be a result of repeated fracturing and cold welding during the MA process. Intimately mixed, submicron phase domains are visible from these micrographs as a result of the mechanical alloying process. Another notable difference between CMA 10h samples and Unmilled or Control samples is the absence of microtoming artifacts such as chatter.

### 8.1.7 Scanning Transmission X-Ray Microscopy

The STXM image of CMA 10h powder, collected at 286.2eV, is shown in Figure 8.12.

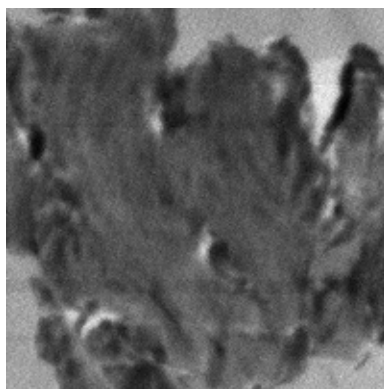


**Figure 8.12:** STXM image of CMA 10h powder collected at 286.2eV.

Individual components cannot be discerned due to their intimate level of mixing and closely related X-ray spectra. A spectral stack was performed, collecting images at a series of energies in order to use the stack spectra to calculate a spatial map of the composition thickness. In principle, one could use absorption spectra from uniform thin films of epoxy, PC, and PEEK to obtain quantitative maps of the distribution of these three components in the image sequence; however, there appears to have been a slight shift in the monochromator calibration between the recording of the thin film standard spectra and the image sequence, rendering the quantitative analysis of this particular dataset untrustworthy. It is not possible therefore to use this data to obtain a composition map of the CMA 10 powder. Principal component analysis performed by Dr. Chris Jacobsen at Brookhaven National Labs revealed the presence of two different phases within the CMA 10h powder particle, confirming TEM images showing an intimately mixed two-phase material. Principal component analysis also corroborated with FTIR data, which indicated that a third phase was not

formed upon mechanical alloying PC and PEEK. X-ray spectra (absorption coefficient,  $\mu$ , vs. X-ray energy) of Unmilled PC and PEEK are shown in Figure 8.13.

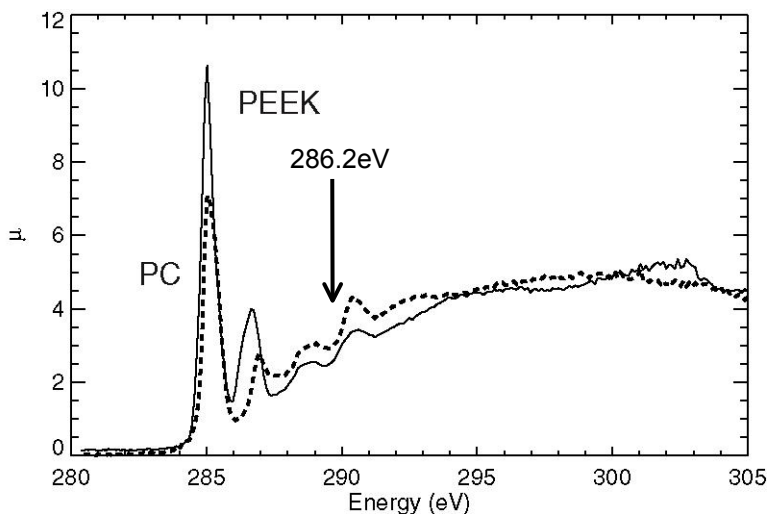


**Figure 8.13:** X-ray spectra of Unmilled PC and PEEK.

## 8.2 Testing Molded Bars

### 8.2.1 Dynamic Mechanical Analysis

Representative isochronal DMA results are shown in Figure 8.14 through Figure 8.23. Storage modulus and loss modulus are plotted as a function of temperature for Mixed and Control samples. As with Mixed and Control samples, inner (i) and outer (o) bars were tested from the same injection molding coupon, along with replicates of each injection molding condition.

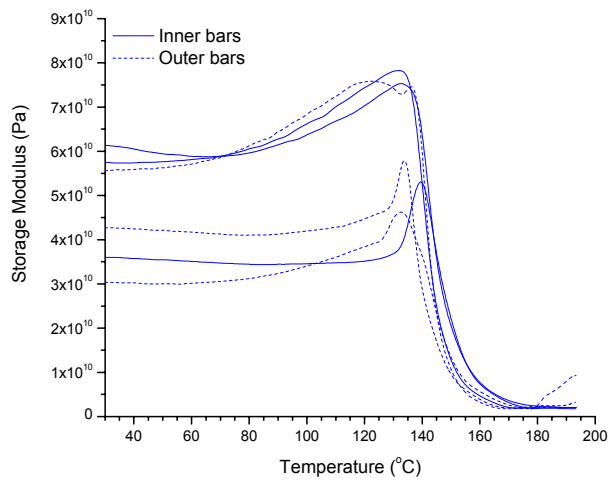


**Figure 8.14:** Storage Modulus data for CMA 10h samples injection molded at 350°C.

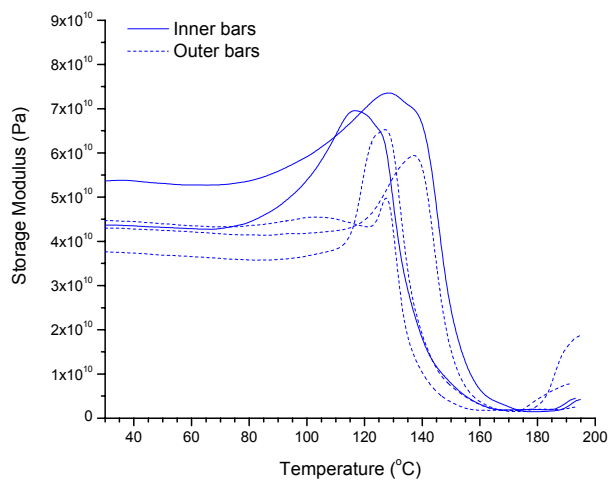


**Figure 8.15:** Storage Modulus data for CMA 10h samples injection molded at 360°C.

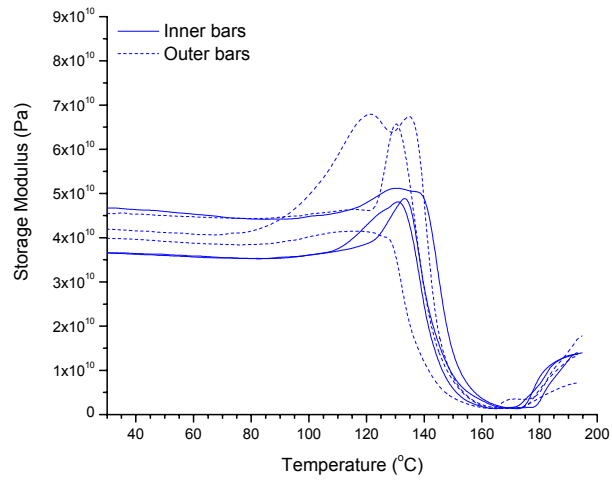


**Figure 8.16:** Storage Modulus data for CMA 10h samples injection molded at 370°C.

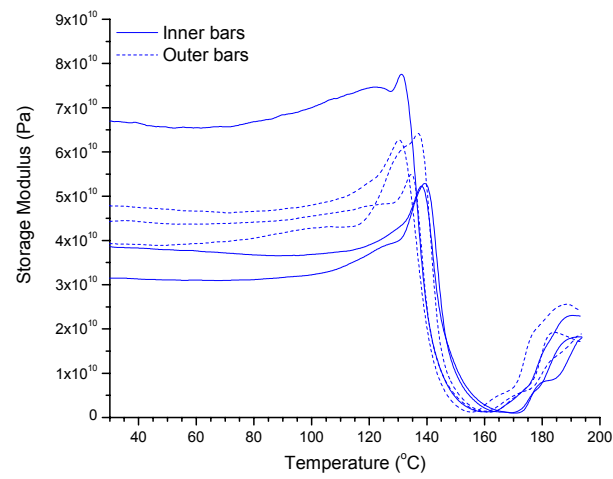


**Figure 8.17:** Storage Modulus data for CMA 10h samples injection molded at 380°C.

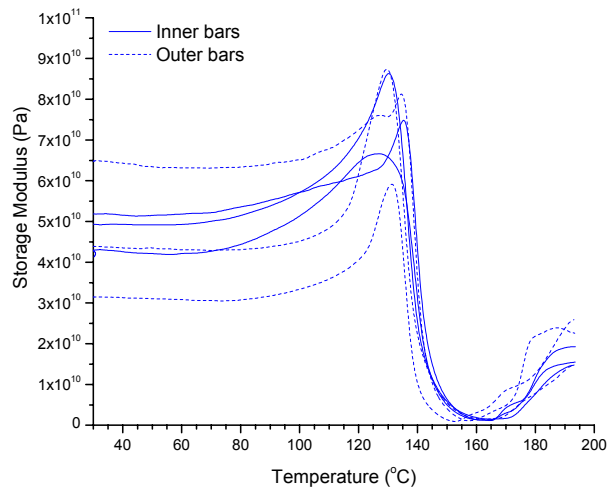


**Figure 8.18:** Storage Modulus data for CMA 10h samples injection molded at 390°C.

CMA 10h bars molded at 350 °C exhibit a shoulder or peak in the storage modulus prior to the glass transition, and this peak is present in bars injection molded at all other temperatures. The shape and magnitude of the peak/shoulder varies greatly from sample to sample.

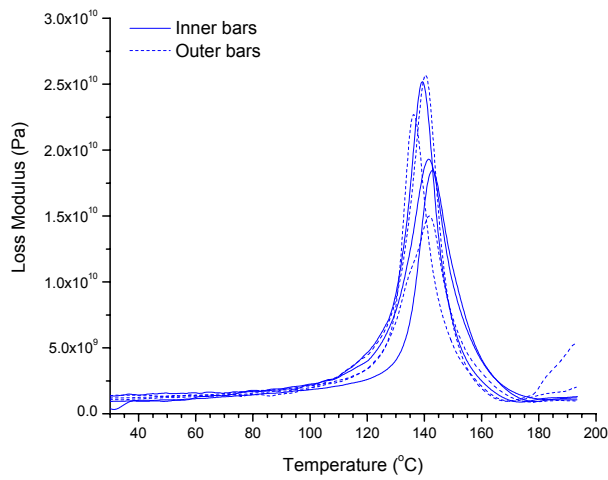


**Figure 8.19:** Loss Modulus data for CMA 10h samples injection molded at 350°C.

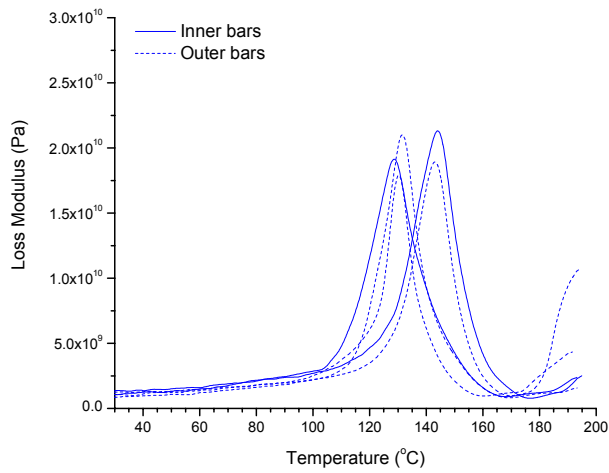


**Figure 8.20:** Loss Modulus data for CMA 10h samples injection molded at  $360^{\circ}\text{C}$ .

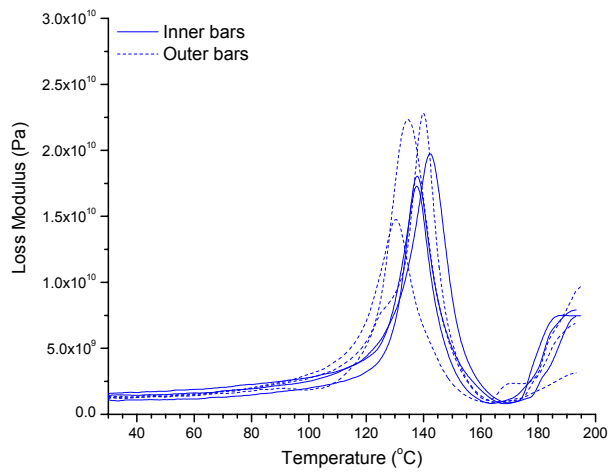


**Figure 8.21:** Loss Modulus data for CMA 10h samples injection molded at  $370^{\circ}\text{C}$ .

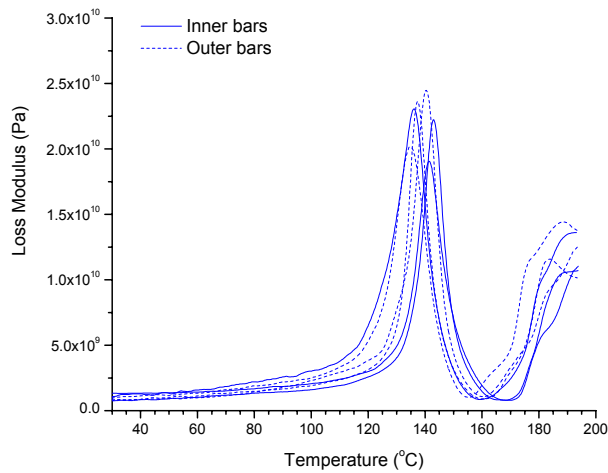


**Figure 8.22:** Loss Modulus data for CMA 10h samples injection molded at 380°C.

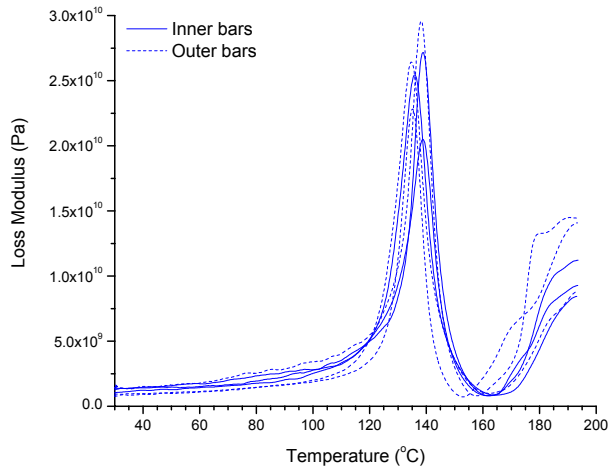


**Figure 8.23:** Loss Modulus data for CMA 10h samples injection molded at 390°C.

A single loss peak is observed for CMA 10h bars molded at all temperatures, whereas Mixed and Control samples molded at 350°C and 360°C exhibited double loss peaks. The CMA 10h sample molded at all temperatures exhibit considerable coupon-to-coupon variation in the  $T_g$ , as measured by DMA. Considerable variation also exists between inner and outer bars molded as part of the same injection molding coupon. Less variation exists in  $T_g$  for bars molded at 350°C and 390°C (the lower and upper limits of processing temperatures).

To ensure that discrepancies in loss peak temperature ( $T_g$ ) for CMA 10h samples were not due to machine variation or temperature calibration errors, the Indium temperature calibration standard was tested between two replicate samples (CMA 10h injection molded at 360°C ). The  $T_g$  measured for the first CMA 10h bar injection molded at 360°C equaled 144°C. The melting temperature measured for the indium standard was 156.8°C (0.2°C off from the calibrated value), but the second replicate of the CMA 10h bar injection molded at 360°C exhibited a melting temperature of 129°C (a 14°C difference from the previous test). One possible explanation for some of the discrepancies in DMA data between replicate samples is inhomogeneity of the CMA 10h powder itself. The ball mill used in this work is believed to be a very inefficient compared to commercial mills, and the design allows for some powder to settle at the bottom of the vial during milling, which may cause the resulting mechanically alloyed powder to be two-phase, yet inhomogeneous within a batch. More discussion of the importance of ball mill design for mechanical alloying follows in Chapter 9. The other major contributing factor to the inconsistencies in DMA data from coupon to coupon (and inner vs. outer bars from the same coupon) is the fact that the microstructure of these bars is phase separating (demixing) as the bar is heated during the DMA test. Once additional (thermal) energy is added to these samples by testing in the DMA, thermal events begin to occur due to the kinetics of demixing, and all measured dynamic mechanical transitions are affected. These effects may occur at different rates in replicate bars.

### **8.2.2 Quasi-Static Three-Point Bend Testing**

Stress-strain plots from quasi-static 3-point bend testing conducted at 0.1mm/sec using the TA.XT2i are shown in Figure 8.24 through Figure 8.33. Tests were also conducted at 1.0mm/s to determine if rate effects exist which may indicate a change in interface properties. For samples that did not fracture before 40% strain was reached, the test was stopped. Results from replicate bars tested at 0.1mm/s are shown in the first column, while results from bars tested at 1.0mm/s are shown in the second column.

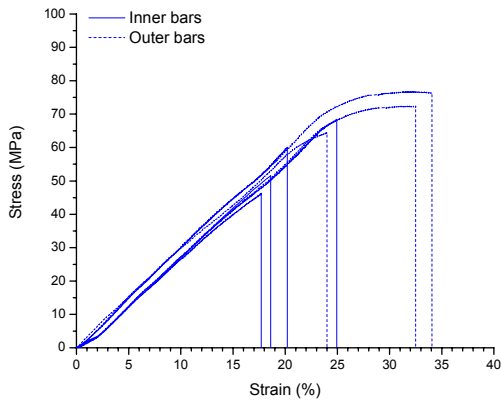


**Figure 8.24:** 3-point bend data for replicate bars molded at 350°C, tested at 0.1mm/sec.

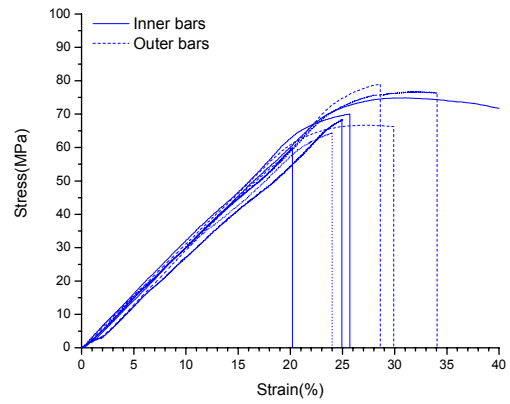


**Figure 8.25:** 3-point bend data for replicate bars molded at 350°C, tested at 1.0mm/sec.

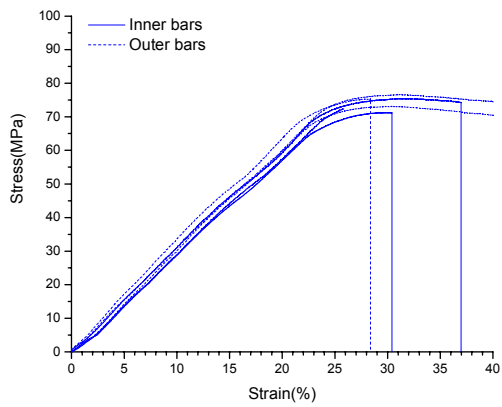


**Figure 8.26:** 3-point bend data for replicate bars molded at 360°C, tested at 0.1mm/sec.

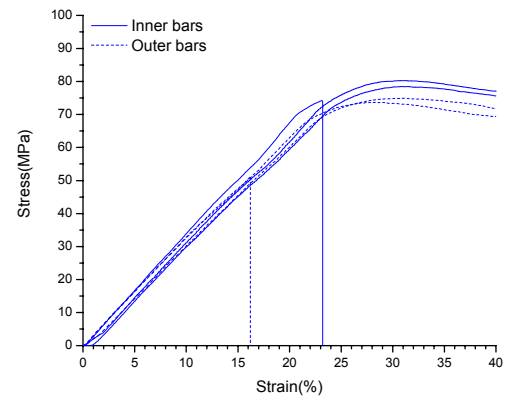


**Figure 8.27:** 3-point bend data for replicate bars molded at 360°C, tested at 1.0mm/sec.

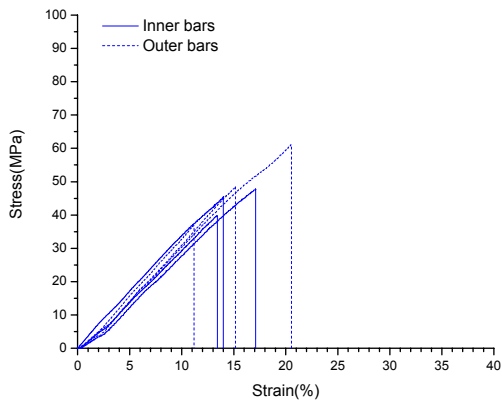


**Figure 8.28:** 3-point bend data for replicate bars molded at 370°C, tested at 0.1mm/sec.

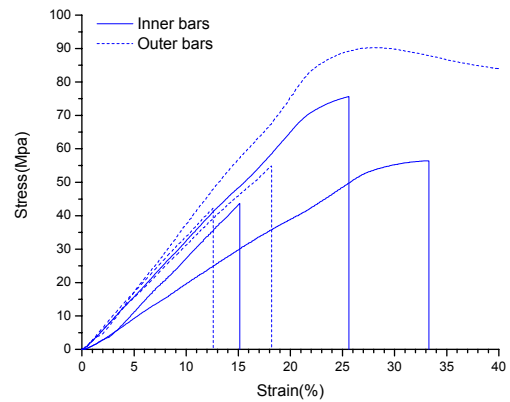


**Figure 8.29:** 3-point bend data for replicate bars molded at 370°C, tested at 1.0mm/sec.

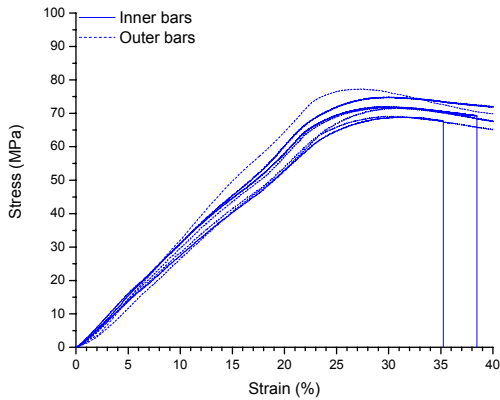


**Figure 8.30:** 3-point bend data for replicate bars molded at 380°C, tested at 0.1mm/sec.

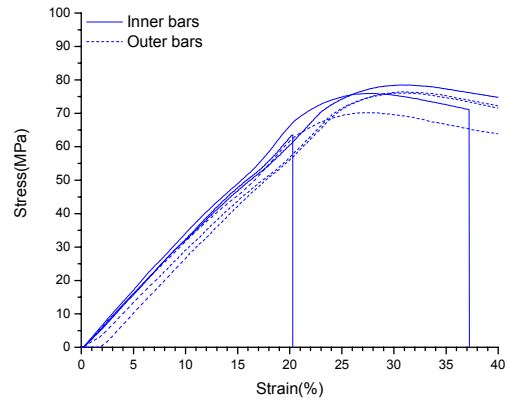


**Figure 8.31:** 3-point bend data for replicate bars molded at 380°C, tested at 1.0mm/sec.

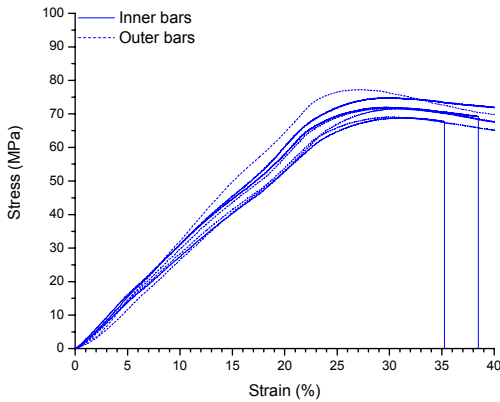


**Figure 8.32:** 3-point bend data for replicate bars molded at 390°C, tested at 0.1mm/sec.

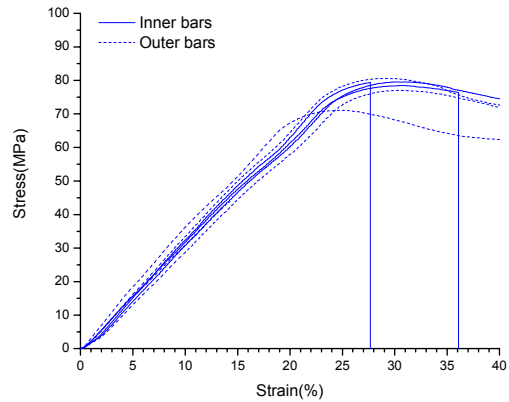


**Figure 8.33:** 3-point bend data for replicate bars molded at 390°C, tested at 1.0mm/sec.

Energy to failure values were calculated by integrating the area under the stress-strain curves. Values calculated for CMA 10h samples injection molded at each temperature and tested at 0.1mm/s and 1.0mms are shown in Figure 8.34. In addition, energy to failure values for CMA 10h samples and Control samples tested at 0.1mm/s are compared in Figure 8.35. The standard deviation for each sample type is shown as error bars.

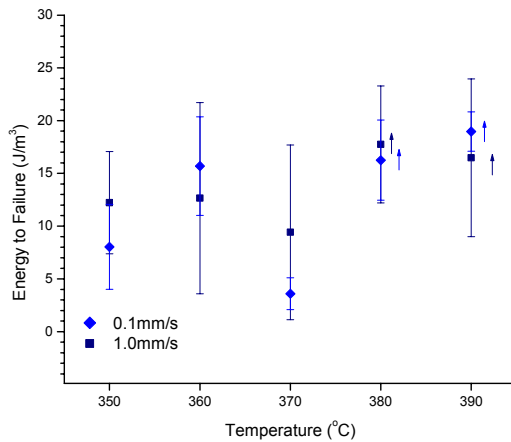


**Figure 8.34:** Energy to failure values for CMA 10h samples tested at 0.1mm/s and 1.0mm/s. Arrows indicate samples where actual values are higher than measured values because the test was stopped at 40% strain.

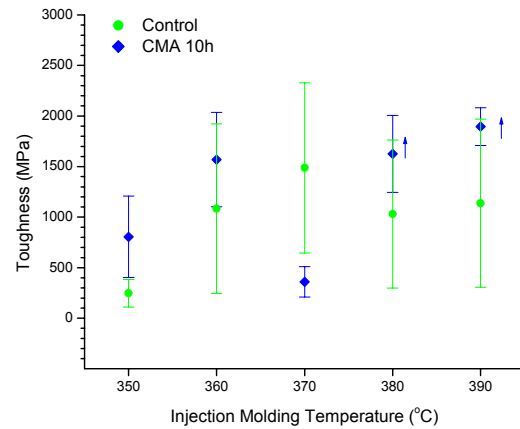


**Figure 8.35:** Energy to failure values for Control and CMA 10h samples tested at 0.1mm/s. Arrows indicate samples where actual values are higher than measured values because the test was stopped at 40% strain.

For Mixed and Control samples (Figure 7.32), samples exhibited an increase in average energy to failure values between 350°C and 360°C as the ability to fill the mold improved, then the energy to failure values essentially leveled off. In the case of the CMA 10h samples tested at both rates, average energy to failure values increase as injection molded temperature increased from 350°C to 360°C even though the polymer flowed well enough to fill the mold at 350°C; then energy to failure essentially remains constant for 360°C, 380°C, 390°C samples, with a noticeable dip in the energy to failure of the 370°C sample. There is no statistically significant difference (according to T-tests performed at a 95% confidence level) between the energy to failure values of samples tested at 0.1mm/s and those tested at 1.0mm/s, indicating that no rate effect is observed for these test speeds. The standard deviation is greater for the higher test speed (1.0mm/s). Except for the 370°C molding temperature, CMA 10h samples exhibited energy to failure values that were approximately the same as the Control samples.

The failure strength (the stress at which the sample either breaks or reaches 40% strain) was determined for each sample. Average failure strength values for CMA 10h samples tested at both speeds are shown in Figure 8.36. Additionally, failure strength values for CMA 10h samples and Control samples tested at 0.1mm/s are compared in Figure 8.37. Strain at failure values are shown for CMA 10h tested at 0.1mm/s

and 1.0mm/s in Figure 8.38 and for Control and CMA 10h in Figure 8.39. Standard deviations shown as error bars.

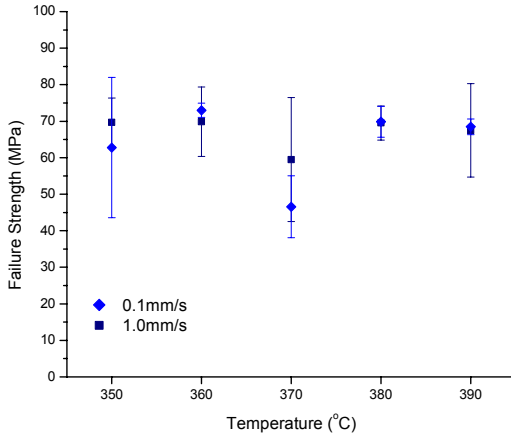


**Figure 8.36:** Failure strength values for CMA 10h samples tested at 0.1mm/s and 1.0mm/s.

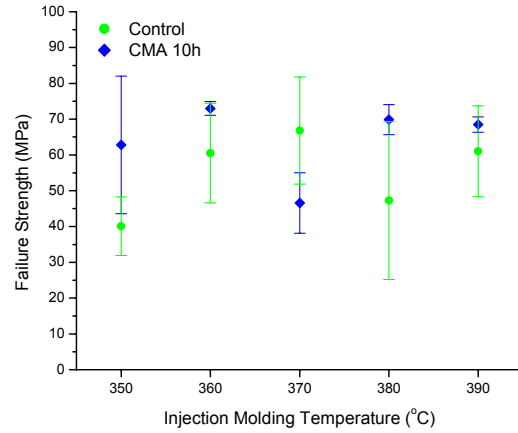


**Figure 8.37:** Failure strength values for Control and CMA 10h samples tested at 0.1mm/s.

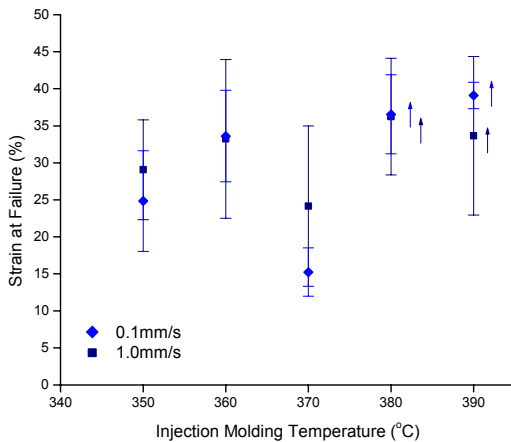


**Figure 8.38:** Strain at failure values for CMA 10h samples tested at 0.1mm/s and 1.0mm/s. Arrows indicate samples where actual values are higher than measured values because the test was stopped at 40% strain.

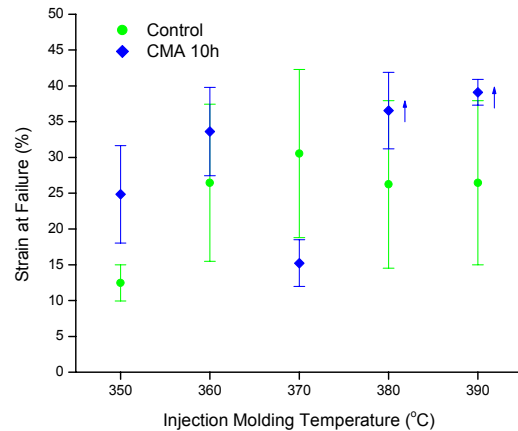


**Figure 8.39:** Strain at failure values for Control and CMA 10h samples tested at 0.1mm/s. Arrows indicate samples where actual values are higher than measured values because the test was stopped at 40% strain.

Similar to the trend observed for average energy to failure values, average failure strength values are essentially equivalent for bars tested at 0.1mm/s compared to 1.0mm/s. In addition, the strength values for samples molded at different temperatures and tested at both 0.1mm/s and 1.0mm/s are equivalent with the exception of the bars molded at 370°C, which possess a lower strength than bars molded at all other temperatures. Based on these data, no rate effect was found between these test speeds. While a rate effect

may exist by testing at a much slower or faster rate, the lower limit of the equipment has been reached, so testing at a slower rate was not possible. While testing at a faster test speed is possible, preliminary tests conducted at 10mm/s were discontinued because the test finished too quickly to obtain sufficient data points for analysis. Furthermore, average strength at failure values were generally higher for the CMA 10h samples than the Control samples, with the exception of the 370°C molding temperature.

### **8.3 Imaging Molded Bars**

At 350°C, the CMA 10h powder filled the mold sufficiently after 5 minutes of heating in the barrel and resulted in a quality coupon during every shot. This is in contrast to the Mixed and Control samples, which did not flow well enough to completely fill the mold at 350°C. During heating and molding at 370°C and higher temperatures, smoke was observed rising up from the barrel, accompanied by an odor which worsened as injection molding temperature was increased to 390°C. These phenomenon indicate that some thermal degradation occurred during heating at these temperatures. In addition, blackened areas appeared on the surface of some molded coupons for samples injection molded at 380°C and 390°C, and this occurrence was more prevalent on outer bars compared to inner ones. A skin-core morphology formed for these samples due to injection into a room temperature mold; this is visible in the first column of scanning electron micrographs presented in Figure 8.10.

#### **8.3.1 Atomic Force Microscopy**

The morphology of CMA 10h bars molded at 350°C, 360°C, 370°C, and 390°C were imaged using tapping mode atomic force microscopy. Representative micrographs taken from the center of each bar are shown in Figure 8.40. Images taken from bars molded at designated temperatures are shown in rows, with columns representing 5, 10 and 20 square micron scans.

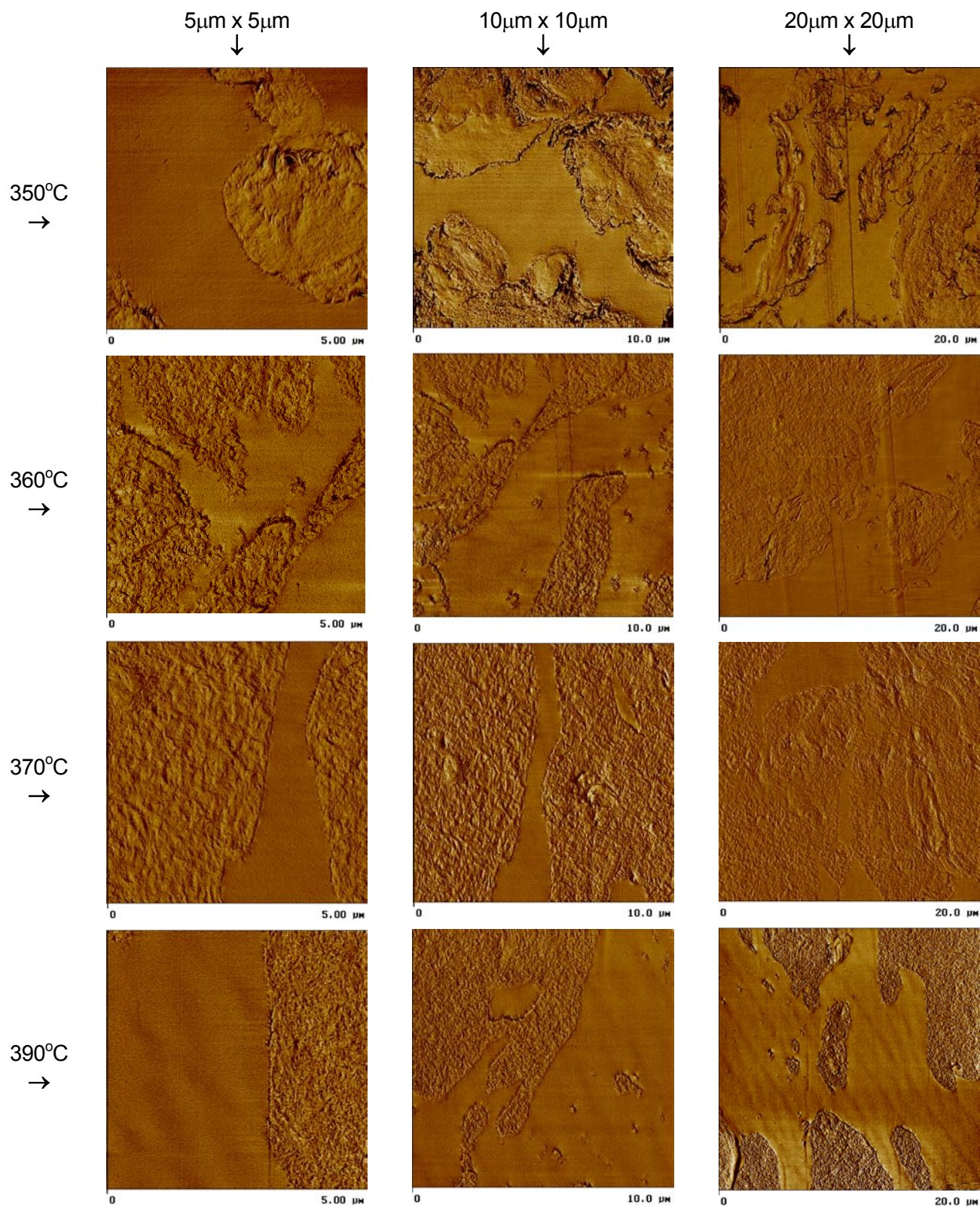
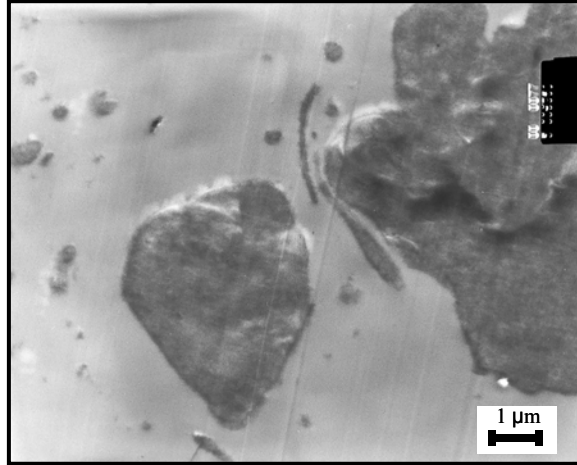


Figure 8.40: AFM images of injection molded MA 10h bars

An examination of these micrographs reveals that the morphology of CMA 10h injection molded bars is very similar to bars injection molded from Control powder, despite the difference in powder morphology of the Control and CMA 10h powder samples prior to injection molding. These micrographs demonstrate that a great deal of demixing occurred to the previously submicron phase domains present in the CMA 10h powder upon post-MA injection molding using these conditions. PC and PEEK phases are sized on the order of microns (or tens of microns) in these samples rather than the sub-micron phase domains present in the CMA 10h powders. An examination of these micrographs also reveals some differences in the microstructure of the CMA 10h bars injection molded at different temperatures. The bar molded at 350°C appears to consist of both PEEK and PC phases within a PC matrix or regions of semi-crystalline and amorphous PEEK, while the bars injection molded at 360°C and higher temperatures appear to consist of PEEK phases within a PC matrix, and may contain some areas of “trapped” PC present within the large PEEK phases.

### **8.3.2 Transmission Electron Microscopy**

Transmission electron microscopy was used to corroborate results obtained via atomic force microscopy regarding the microstructure of molded bars. The CMA 10h sample injection molded into a test bar at 360°C was examined using TEM (micrograph shown in Figure 8.41), revealing darker PEEK-rich phases of varying size and shape within a (lighter) PC continuous matrix. In addition, knife marks are visible (indicating the microtoming direction); these show that no microstructural directionality results from sample preparation.



**Figure 8.41:** TEM micrograph showing cross-section of bar injection molded at 360°C.

### 8.3.3 Scanning Transmission X-Ray Microscopy

Scanning transmission X-ray microscopy was used to obtain X-ray images of a molded bar (CMA 10h molded at 380°C) at two energies. Individual spectra of PC and PEEK revealed that at 286.2eV, PEEK absorbs energy, and thus appears dark while PC does not and thus appears light. At 287.2eV, however, the opposite is true, as the PEEK phase appears lighter than the PC, but the contrast is not sufficient. Images collected at these energies are shown in Figure 8.42.

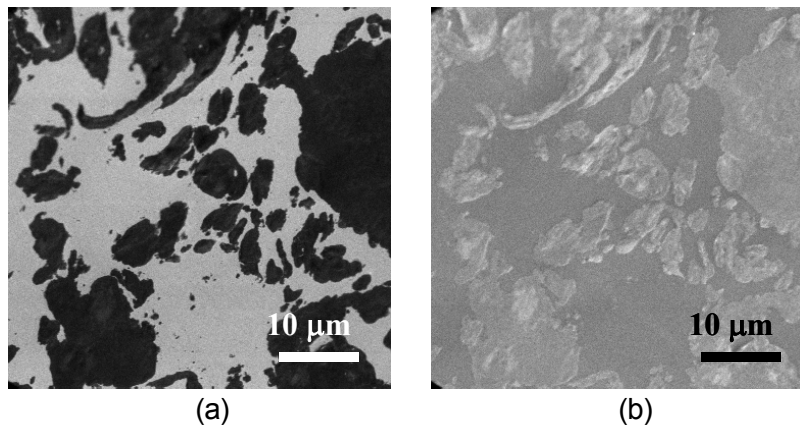


**Figure 8.42:** STXM images of CMA 10h bar molded at 380°C, taken at (a) 286.2 eV and (b) 287.2eV.

Because STXM provides unambiguous phase distinction, these results confirm the interpretation presented previously of the micrographs obtained via AFM and TEM: bars consist of a continuous PC matrix

with PEEK phases of varying size and shape. Because TEM and STXM data also offered proof of intimate mixing in CMA 10h powder prior to injection molding, gross phase separation occurred to the CMA 10h powder upon post-MA processing in this manner.

## **8.4 Imaging Tested Bars**

### **8.4.1 Scanning Electron Microscopy**

Fracture surfaces of samples tested in 3-Point bend mode at 0.1mm/s using the TA.XT2i were imaged at three magnifications using scanning electron microscopy. In Figure 8.40, bars injection molded at designated temperatures are shown in rows, with columns corresponding to different magnifications (scales are shown).

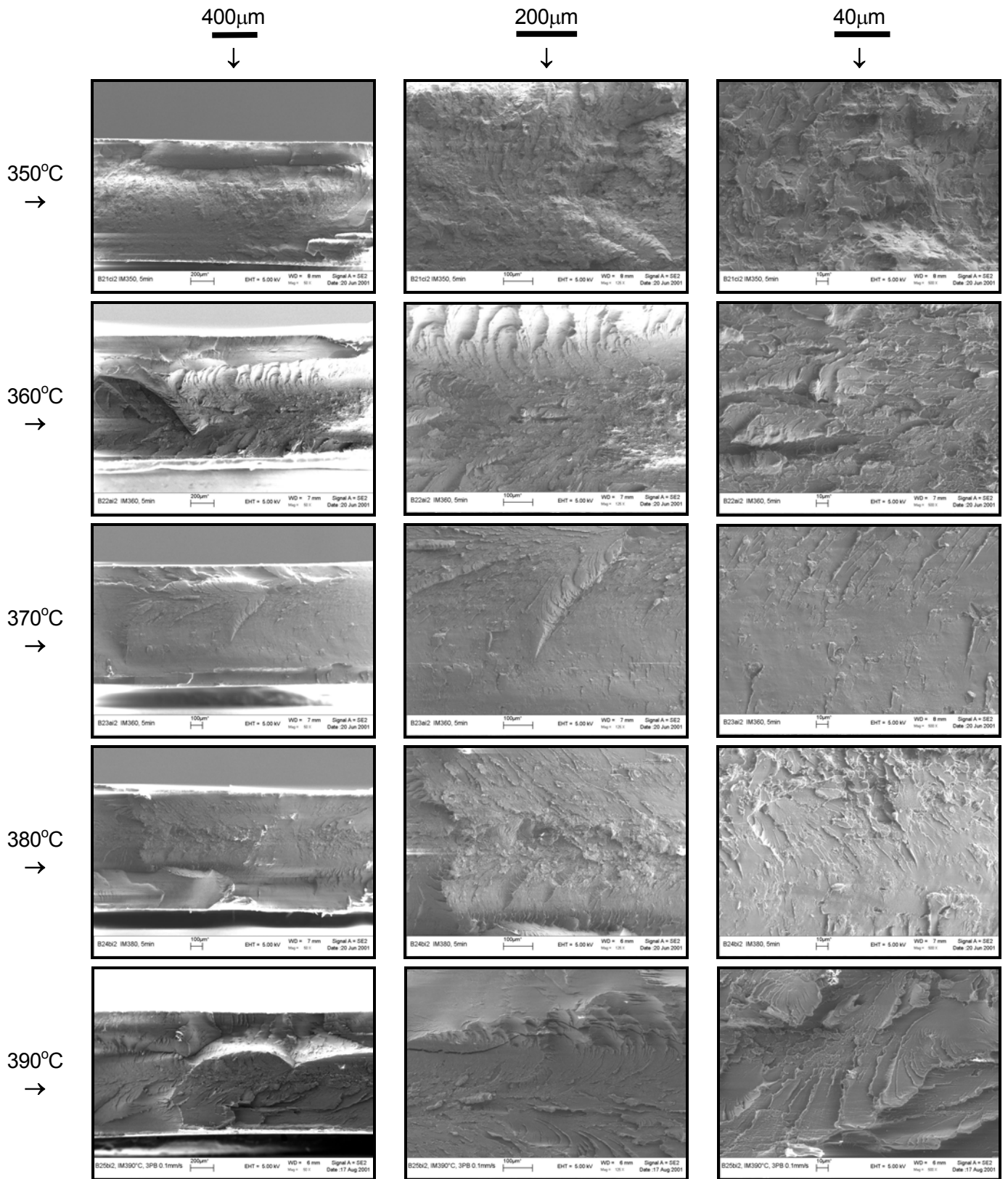


Figure 8.43: SEM micrographs of CMA 10h fracture surfaces tested at 0.1mm/s.

The skin-core morphology formed upon injection into a room temperature mold is visible in the lowest magnification images. The topology of the CMA 10h molded bars tested at 0.1mm/s resemble those of the Control bars. Fracture surfaces of samples tested in 3-Point bend mode at 1.0mm/s using the TA.XT2i were also imaged at three magnifications using scanning electron microscopy. These images are not shown, as they exhibited no noticeable differences from the samples tested at 0.1mm/s.

### 8.5 Testing Annealed Bars

Additional CMA 10h bars were annealed at 160°C for 20 minutes prior to subsequent testing. Dynamic mechanical and static 3-point bend tests were performed on annealed bars using the same testing parameters as the as-molded bars.

#### 8.5.1 Dynamic Mechanical Analysis

Dynamic mechanical results for annealed and as-molded Mixed and Control bars are shown in Figure 8.44 through Figure 8.48

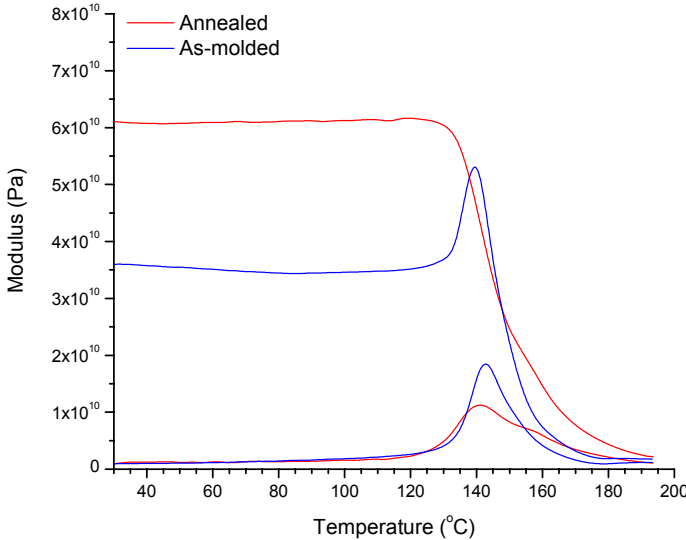


**Figure 8.44:** Comparison plot of annealed vs. as-molded CMA 10h samples, molded at 350°C.

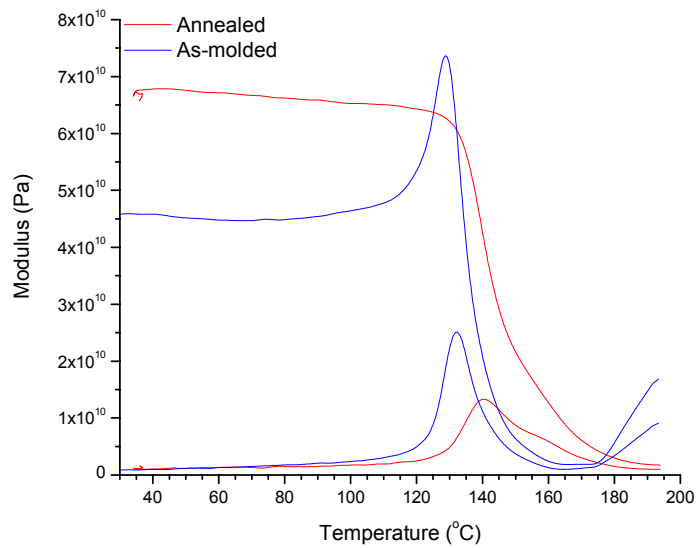


**Figure 8.45:** Comparison plot of annealed vs. as-molded CMA 10h samples, molded at 360°C.

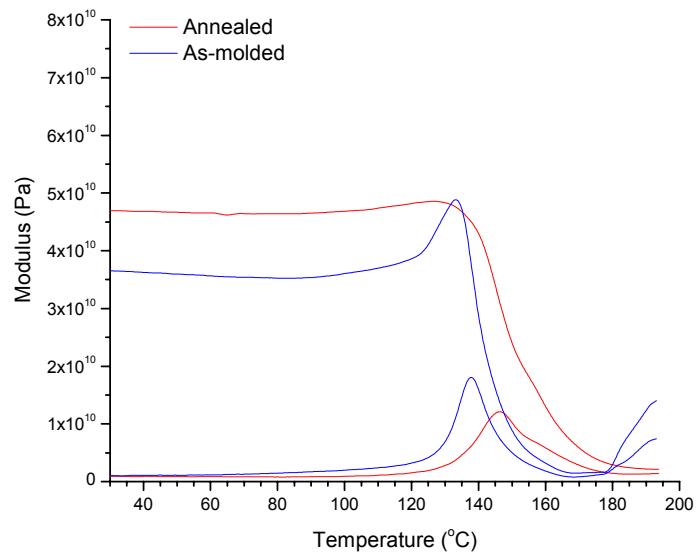


**Figure 8.46:** Comparison plot of annealed vs. as-molded CMA 10h samples, molded at 370°C.

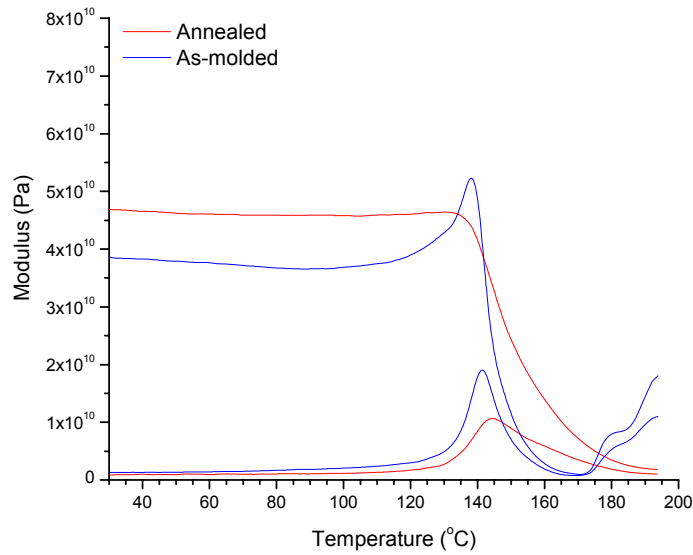


**Figure 8.47:** Comparison plot of annealed vs. as-molded CMA 10h samples, molded at 380°C.

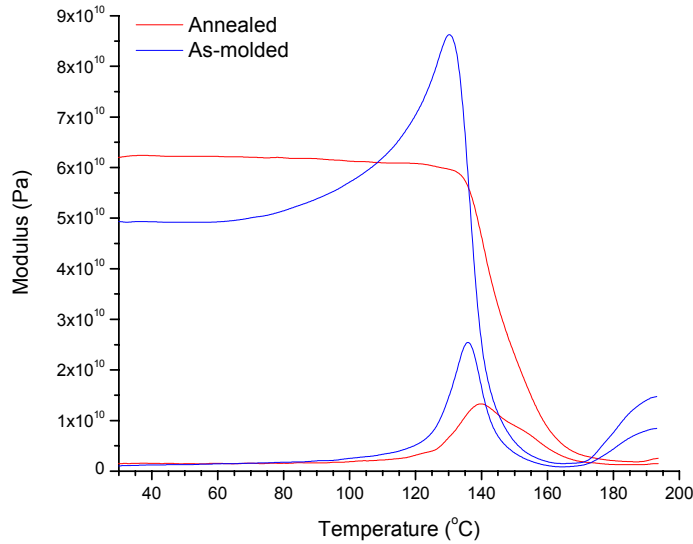


**Figure 8.48:** Comparison plot of annealed vs. as-molded CMA 10h samples, molded at 390°C

For bars injection molded at each temperature, the annealed bar exhibited a higher initial storage modulus than the as-molded bars. A similar trend was observed for the Mixed and Control samples reported in Chapter 7. In addition, the peak present in the storage modulus prior to the glass transition of all CMA 10h as-molded bars is absent in all CMA 10h annealed bars. This trend is also similar to the one observed for Control samples. Likewise, CMA 10h samples exhibit a similar trend as the one observed for

Mixed and Control samples in that the loss modulus peaks are broader for CMA 10h annealed bars. The loss modulus peak for all CMA 10h annealed bars is located at a higher temperature than the corresponding loss modulus peak for as-molded CMA 10h bars. It is unclear why the annealed samples show a shoulder in the loss modulus peak. This trend differs slightly from the one observed for Mixed and Control samples, where the peak was located at the same temperature for bars molded at some temperatures, while it was located at a higher temperature for bars molded at others.

### 8.5.2 Quasi-Static Three-Point Bend Testing

Results from 3-point bend testing performed at 0.1mm/s on annealed bars are shown in Figure 8.49 through Figure 8.53. For samples that did not fracture by the time 40% strain was reached, the test was stopped.

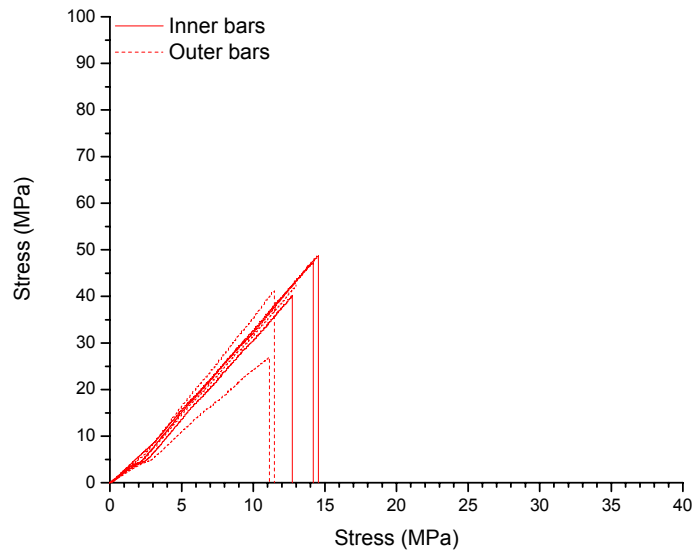


**Figure 8.49:** 3-point bend data for bars molded at 350°C, then annealed.

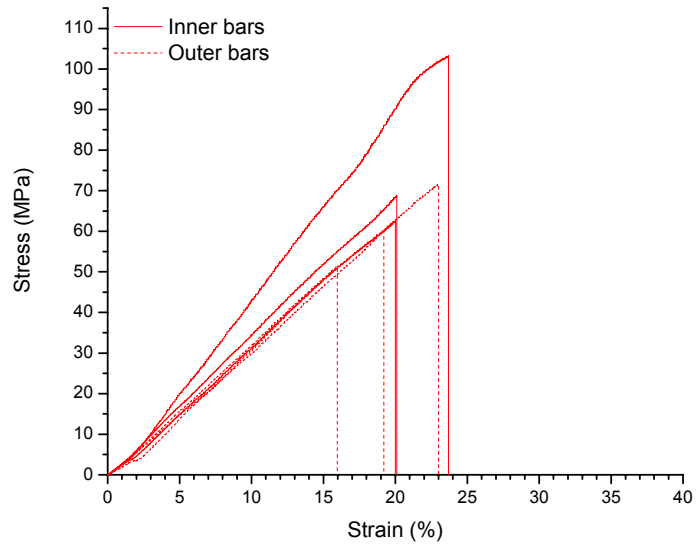


**Figure 8.50:** 3-point bend data for bars molded at 360°C, then annealed.

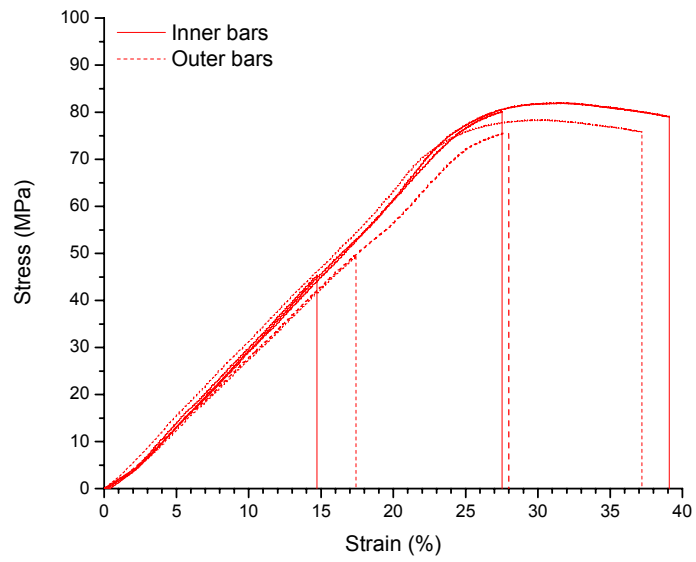


**Figure 8.51:** 3-point bend data for bars molded at 370°C then annealed.

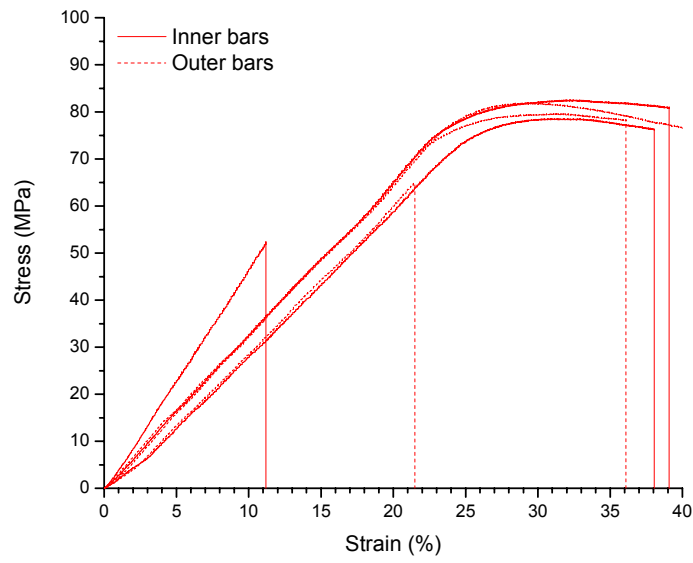


**Figure 8.52:** 3-point bend data for bars molded at 380°C then annealed.

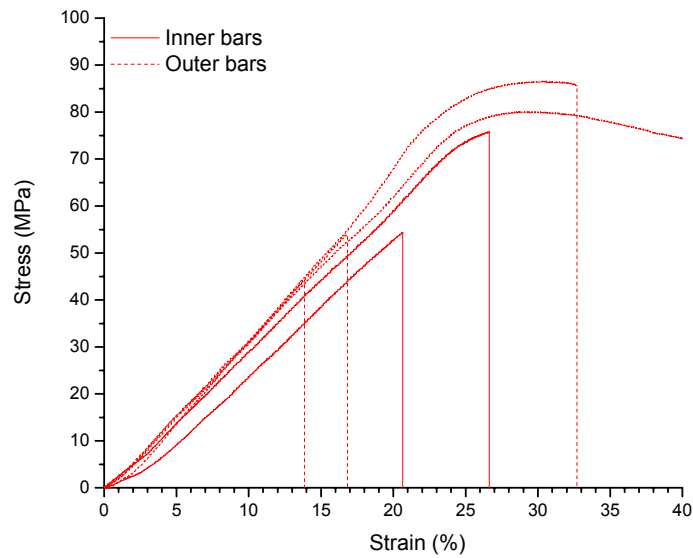


**Figure 8.53:** 3-point bend data for bars molded at 390°C then annealed.

Energy to failure and failure strength values were determined from 3-point bend test results. Results from CMA 10h as-molded and CMA 10h annealed samples are summarized in Figure 8.54 through Figure 8.56.

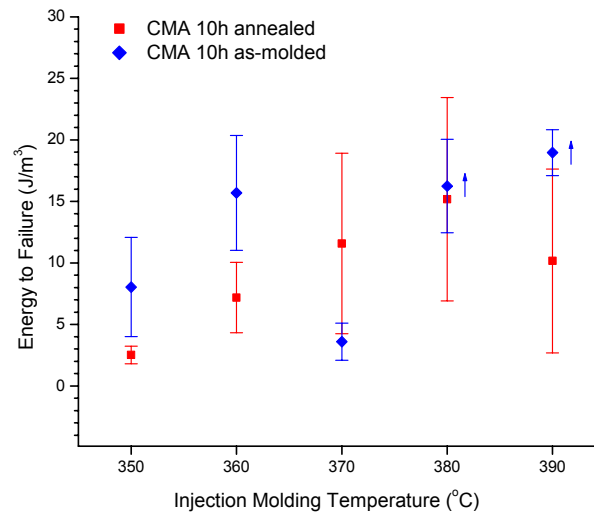


**Figure 8.54:** Energy to failure values for CMA 10h as-molded and CMA 10h annealed samples tested at 0.1mm/s. Arrows indicate samples where actual values are higher than measured values because the test was stopped at 40% strain.

Energy to failure values generally increased as injection molding temperature increased for CMA 10h annealed bars, similar to Mixed and Control samples tested at the same rate. Whereas the CMA 10h as-molded samples exhibited a sharp decrease in both strength and energy to failure at the 370°C injection molding temperature, the CMA 10h annealed samples continued to increase in energy to failure until the injection molding temperature reached 390°C, when the average energy to failure value dropped slightly. This drop at 390°C is possibly due to degradation during injection molding at 390°C. Compared to CMA10h as-molded samples, CMA 10h annealed samples exhibited lower energy to failure values compared to as-molded samples with the exception of the 370°C molding temperature. This discrepancy in energy to failure between CMA 10h as-molded and CMA 10h annealed bars is smaller for at 380°C and 390°C molding temperatures than it is for bars molded at lower temperatures (350°C and 360°C). Figure 8.55 shows failure strength values for CMA 10h annealed and CMA 10h as-molded samples.

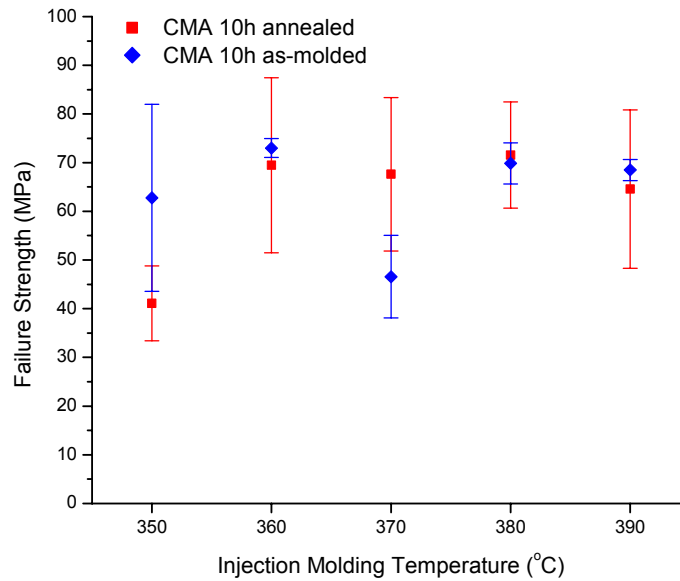


**Figure 8.55:** Failure strength values of CMA 10h as-molded and CMA 10h annealed samples tested at 0.1mm/s.

For CMA 10h samples, average failure strength values remained approximately constant regardless of injection molding temperature with the exception of the 370°C sample. This drop in strength at 370°C molding temperature is not observed for CMA 10h annealed bars, however. In this case, the failure strength increases as injection molding temperature is raised from 350°C to 360°C, then remains constant for higher injection molding temperatures. Average failure strength values for CMA 10h annealed samples are approximately the same as average failure strength values for CMA 10h as-molded samples with the exception of the 350°C molding temperature (where it is lower), and again, the anomalous 370°C temperature. There is a noticeable difference in the number of samples which fractured prior to 40% strain being reached in the CMA 10h annealed bars compare to the CMA 10h as-molded bars. These data are shown in Figure 8.56.

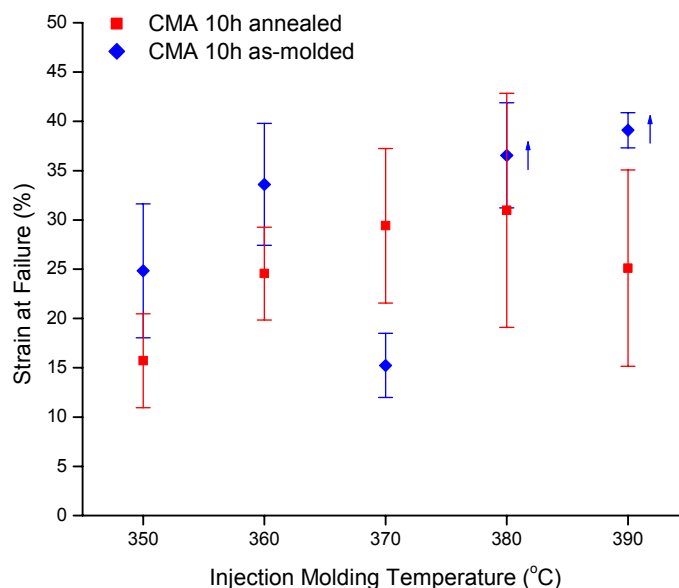


**Figure 8.56:** Strain at failure values of CMA 10h as-molded and CMA 10h annealed samples tested at 0.1mm/s. Arrows indicate samples where actual values are higher than measured values because the test was stopped at 40% strain.

For bars molded at 350°C, the CMA 10h annealed samples all fractured at lower strains than the as-molded samples. Likewise, for bars molded at 360°C, the CMA 10h annealed samples all fractured at lower strains than the as-molded samples. For bars molded at 370°C, the CMA 10h annealed samples all fractured at higher strains than the as-molded samples, contributing to the anomalous behavior of the CMA 10h as-molded bars at this temperature. For bars molded at 380°C, the majority of the bars tested did not fracture prior to test cutoff, whereas the majority of the CMA 10h annealed bars did fracture at strains less than 4%. The same trend is observed for bars molded at 390°C.

## 8.6 Imaging Annealed Bars

### 8.6.1 Atomic Force Microscopy

The morphology of CMA 10h bars molded at 350°C and 390°C was imaged using TappingMode™ atomic force microscopy. Representative micrographs taken from the center of each bar are shown in Figure 8.57.

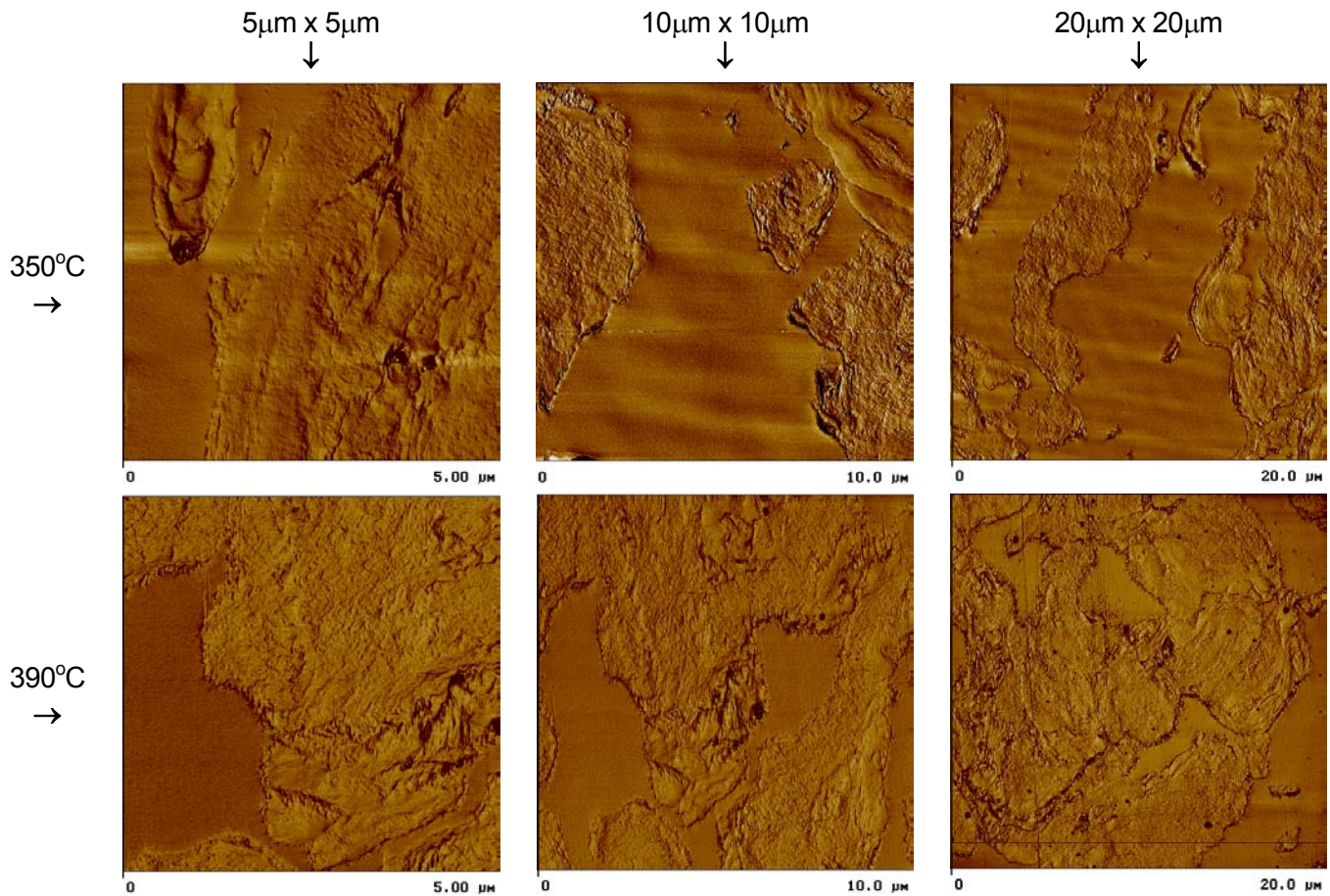


**Figure 8.57:** AFM phase images of annealed samples.

The two phases present in the CMA 10h annealed bars are readily distinguishable: the amorphous PC appears “smooth” in the phase-image AFM mode, while the semi-crystalline PEEK appears “rough”. Bars molded at 350°C and subsequently annealed contain large areas of both PEEK and either PC or amorphous regions of PEEK within the PC matrix. Bars molded at 390°C appear to consist of a PC matrix containing PEEK phases with some PC areas trapped inside or adjacent to PEEK phases. The morphology of the CMA 10h annealed bar molded at 350°C appears to be very similar to the CMA 10h as-molded sample shown in the first row of Figure 8.40. In other words, very little effect from the annealing is visible in the images of the CMA 10h annealed sample. At the other end of the injection molding temperature range, however, the morphology of the CMA 10h annealed bar molded at 390°C looks quite different from the images of CMA

10h as-molded sample injection molded at the same temperature. The annealed bar appears to have regions of PEEK with PC dispersed within it in the PC matrix. A summary of the data presented in Chapters 6-8 is shown in Table 8.2.

<b>Sample Technique</b>	<b>CMM 10 PEEK or PC</b>	<b>Mixed</b>	<b>Control</b>	<b>CMA 10h</b>	<b>Annealed CMA 10h</b>
<i>Powder Characterization</i>					
Particle Size	CMM ↓ particle size & ↑ dispersity			CMM ↓ particle size & ↑ dispersity	
TGA	CMM does not affect measured $T_d$	Presence of other phase ↓ measured $T_d$	Control $T_d$ not different than Mixed	CMA does not lower measured $T_d$ Weight loss ↑ with ↑ mold temperature	
DSC	$T_c$ ↓ for PEEK CMM 10h compared to Unmilled, no change in other transitions with MM	Exhibits single melting peak	Exhibits double melting peak		
GPC	CMM lowers measured $M_w$ , $M_n$ , $M_z$ of PC				
FTIR	CMM does not affect measured IR peaks in PEEK			CMA 10h sample spectra equivalent to Unmilled powders	
WAXD	CMM ↓ measured crystallinity in PEEK				
<i>Injection Molding Observations</i>		350°C, 360°C molding temperatures does not fill mold well	350°C, 360°C molding temperatures does not fill mold well	Mold fills well at all temperatures, some degradation observed	
<i>Testing</i>					
DMA		Some differences between inner and outer bars	Relaxation present prior to $T_g$	Relaxation present prior to $T_g$	No relaxation present prior to $T_g$
TA.XT2 3-Point Bend		↑ energy to failure, $\sigma_f$ , $\epsilon_f$ as mold fills, then properties remain same for higher molding temperature	Trend similar to Mixed samples, slightly more brittle behavior than Mixed	Energy to failure, $\sigma_f$ , $\epsilon_f$ approx. equal except for bars molded at 370°C (properties much lower)	Trend similar to Control samples
<i>Imaging</i>					
SEM	CMM particles are flake-like		Fracture surfaces show some dependence on molding temperature	Fracture surfaces very similar Control samples	
TEM	PEEK particles exhibit chatter		Control powder particles are not two-phase	CMA 10h powders are two-phase, Injection molded bars also two-phase but grossly de-mixed	
AFM			Injection molded bars consist of PEEK phase domains within PC continuous matrix	Injection molded bars also two-phase but grossly de-mixed	
STXM			Injection molded bars consist of PEEK phase domains within PC continuous matrix	CMA 10h powders are two-phase, Injection molded bars also two-phase but grossly de-mixed	

**Table 8.2:** Summary of data.

## 9. DISCUSSION AND CONCLUSIONS

### 9.1 Discussion of Results

The thesis statement guiding this work posed three important questions about the process of mechanically alloying a model polymer system:

1. Is the microstructure created via mechanical alloying retained when mechanically alloyed powders are post-processed into a testable coupon?
2. Does mechanical alloying cause changes in measured mechanical properties compared to Mixed and Control systems?
3. Is the extra processing step of mechanical alloying warranted for this model system?

In order to answer these questions, it first had to be proven that the CMA 10h samples consisted of two-phase powders. Once this was accomplished, the next steps were to select a post-MA processing technique (in this case, injection molding), process the mechanically alloyed powder into a testable geometry (bars), and compare both the microstructure and mechanical properties of the molded bars from Control and CMA 10h powders.

The first question was answered by imaging the microstructure of powders and molded bars using TEM, STXM, and phase image AFM: the mechanically alloyed microstructure was not retained when the powders were post-processed using these conditions. A comparison of the quasi-static three-point bend properties indicated different trends in energy to failure, strain at failure, and failure strength as a function of injection molding temperature for the sample sets. These tests also answered the second question: in this model system, the properties of the mechanically alloyed material were not improved over Mixed or Control samples, and the extra processing time and expense required to mechanically alloy the powders was not warranted if this system is to subsequently injection molded. A discussion of these results is presented here.

#### 9.1.1 Mechanical Testing Trends

As consolidation and flow of a polymer improves with increased molding temperature, one would expect the mechanical properties of an injection molded coupon to improve. Additionally, one would expect that if

thermal degradation occurs upon heating at higher mold temperatures, mechanical properties would suffer. The combination of these effects results in a limited temperature processing window guided by lack of flow on the lower end and degradation on the upper end. Such behavior can be represented in a generalized plot such as Figure 9.1 for mechanical properties vs. temperature.

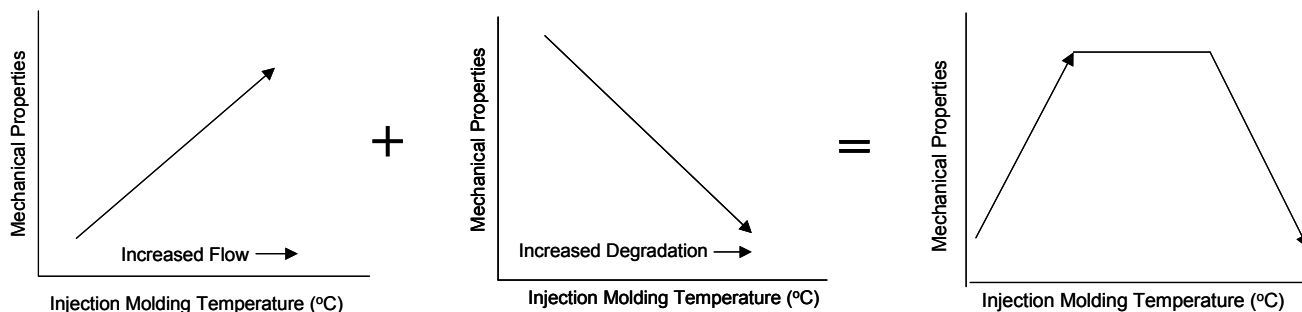


**Figure 9.1:** Generalized schematic of expected property variation with injection molding temperature.

The trend observed during molding of Mixed and Control samples in this work resembles the expected variation of mechanical properties with temperature depicted in the last schematic in Figure 9.1. The Mixed and Control materials did not fill the mold well at or below 350°C, and an improvement in properties occurred between 350°C (when the mold barely fills) and 360°C, when mold filling improves. A plateau was observed at intermediate molding temperatures, until the point where thermal degradation began to decrease measured properties at 390°C. The relevant temperature window for this system was, therefore, determined to be 350°C- 390°C. The schematic of expected properties vs. injection molding temperature for the Mixed and Control samples resembles Figure 9.2. Data for these systems are shown in Figure 9.2b-d.

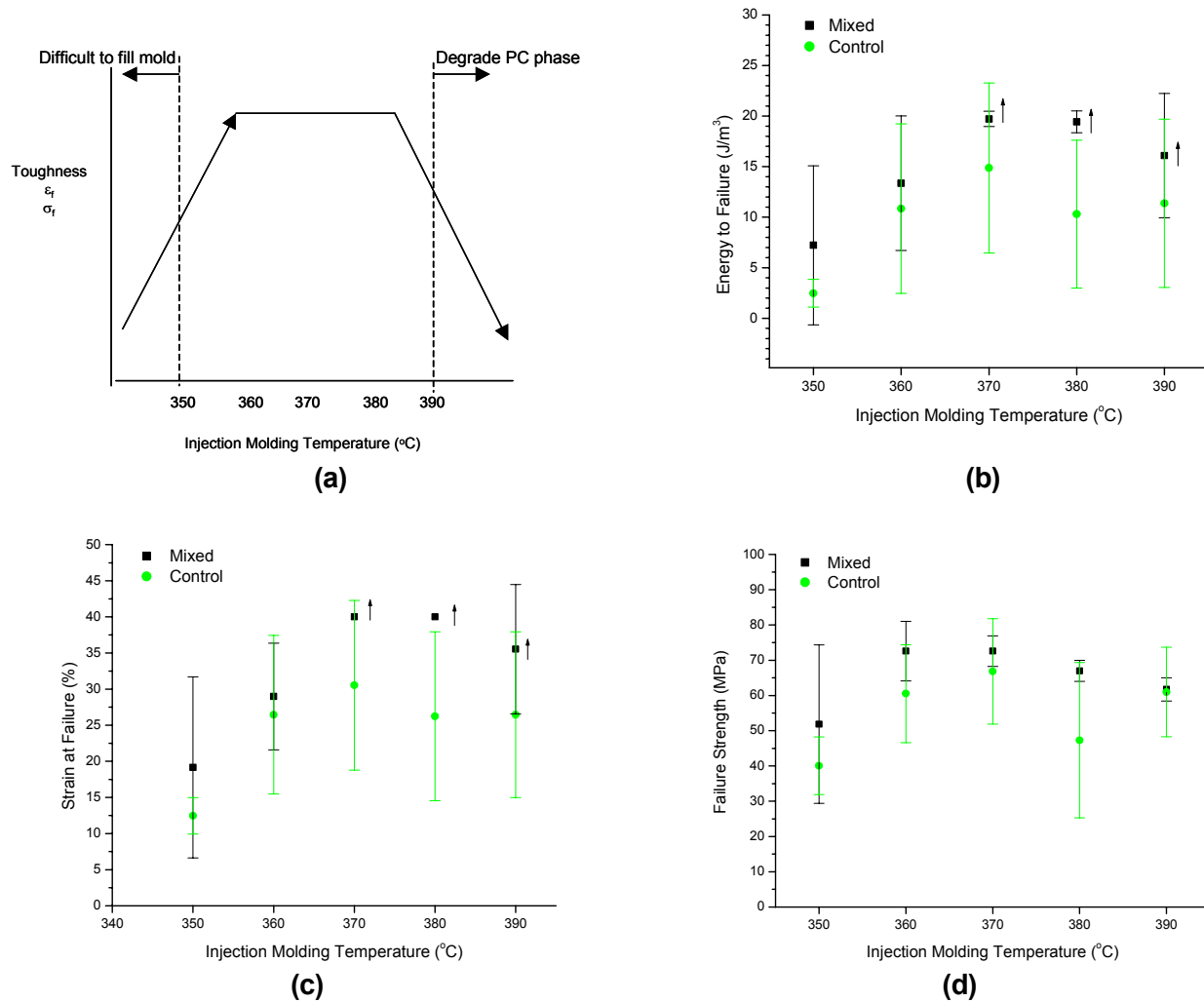
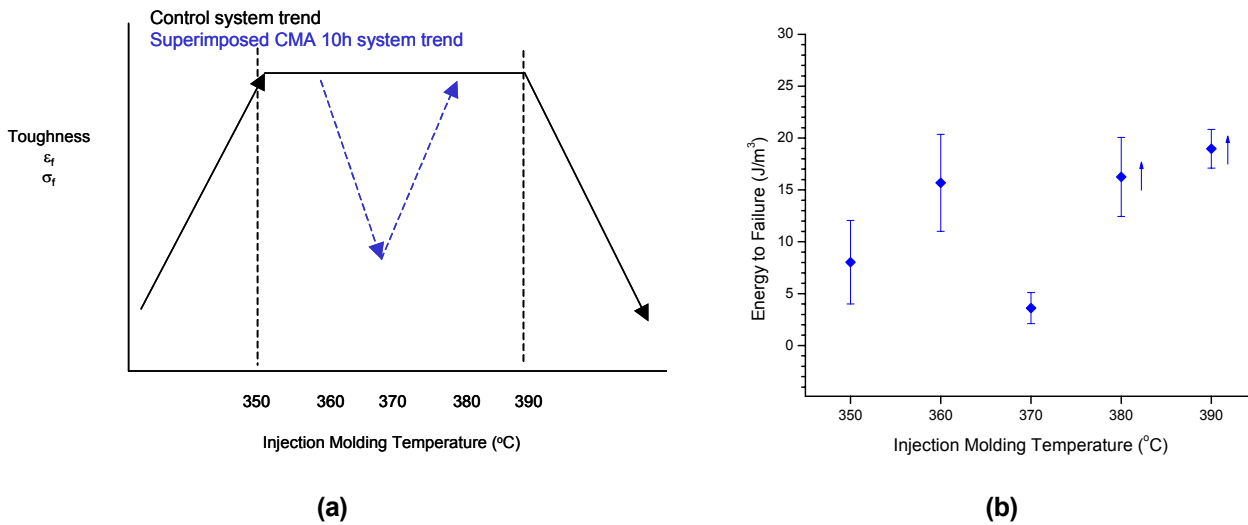


**Figure 9.2:** Property change with injection molding temperature for the Control system: (a) schematic of observed trend (b) energy to failure, (c) strain at failure and (d) failure strength. Arrows indicate samples where actual values are higher than measured values because the test was stopped at 40% strain.

While similar trends were observed overall for Mixed and Control samples, the Control samples exhibited lower average properties at all injection molding temperatures compared to the Mixed samples. In order to determine if the differences in measured properties were statistically significant, T-tests (at a 95% confidence level) were performed on sample populations at each molding temperature. The differences in toughness and strain at failure values are only statistically significant for the 370°C and 380°C molding temperatures, where Mixed samples exhibited superior properties. Differences in failure stress values are not statistically

significant at any molding temperature. In addition, standard deviations for the Control samples are generally greater than those for the Mixed samples, indicating that the Control powders may not be as uniform as the Mixed samples due to prior mechanical alloying, or that residual stresses may be present in coupons made from Control powders. While the system processed in the ball mill for 1 hour with 2 milling balls was chosen as the “Control” group, it cannot be ignored that the mechanical properties of these samples were either equivalent to or lower than those of samples that were simply “hand-mixed” prior to mixing.

The mechanical property trend observed for the CMA 10h samples is different from that observed for the Mixed and Control samples. The trend described in Figure 9.2a occurs in CMA 10h samples, but a new trend is superimposed on the previous one, resulting in a sharp decrease in properties in the samples molded at 370°C. This drop in measured properties was reproducible, occurring at both testing speeds for all samples molded at 370°C. The schematic of property variation with temperature for CMA 10h samples resembles Figure 9.3a. Energy to failure, strain at failure, and failure strength data are shown in Figure 9.3b-d.



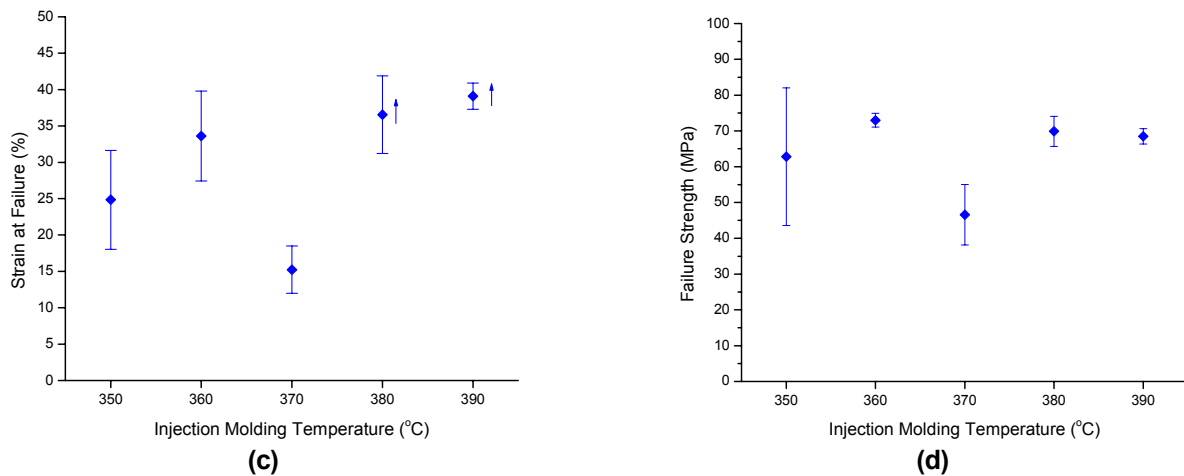
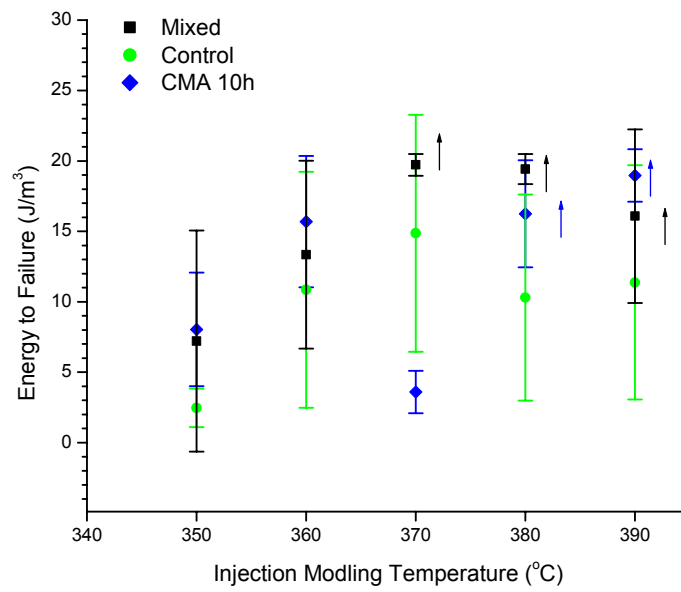
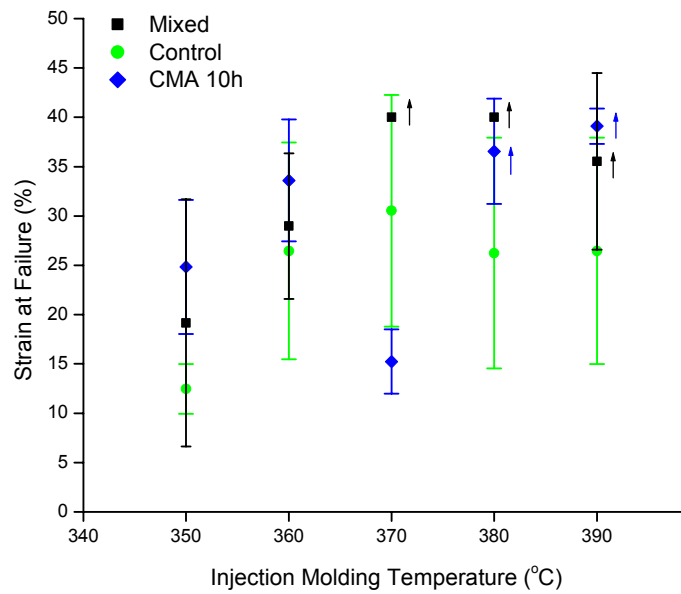


**Figure 9.3:** Property change with injection molding temperature for CMA 10h samples: (a) schematic of trend observed (b) energy to failure, (c) strain at failure and (d) failure strength. Arrows indicate samples where actual values are higher than measured values because the test was stopped at 40% strain.

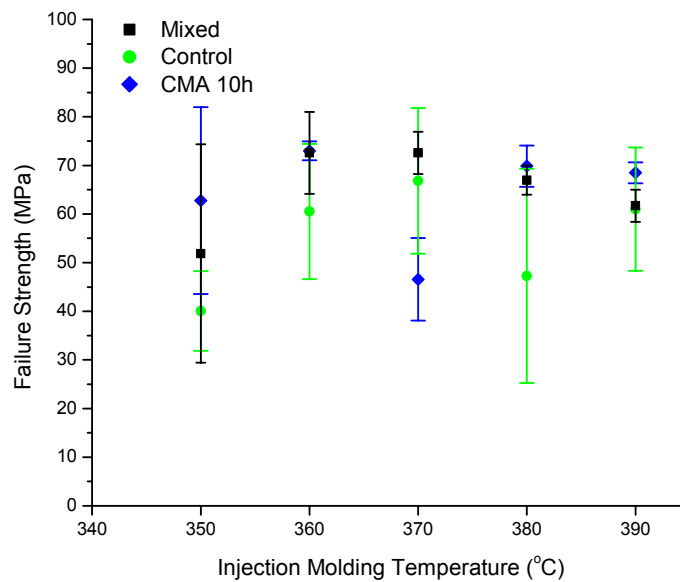
The first clue that the CMA 10h samples differed from Mixed or Control samples came from observations during molding: the CMA 10h powders easily filled the mold at 350°C, whereas the Mixed and Control samples were very difficult to mold at 350°C. The crystalline portion of the PEEK component of the Mixed and Control samples does not melt at 350°C, so the viscosity was higher than that of an amorphous material. Wide angle X-ray diffraction data showed that after 10h hours of MM, the PEEK phase becomes essentially amorphous. The CMA 10h powders are, therefore, essentially amorphous prior to molding, and have a lower viscosity at 350°C than the other samples, in which the PEEK phase is semi-crystalline. It is likely that some improvement in flow is realized in CMA 10h samples by raising the molding temperature to 360°C, as improvement in average property values was observed. As injection molding temperature increased, properties reached a plateau with the exception of a sharp decrease in properties at the 370°C molding temperature, followed by a continuation of the plateau at 380°C. A comparison of the measured properties of all three systems is shown in Figure 9.4.



(a)



(b)



(c)

**Figure 9.4:** Property change with injection molding temperature for Mixed, Control, and CMA 10h samples (a) energy to failure, (b) strain at failure and (c) failure strength. Arrows indicate samples where actual values are higher than measured values because the test was stopped at 40% strain

CMA 10h samples exhibited mechanical property differences that were statistically significant (according to T-tests) from the Control group at 350°C and 370°C. The explanation for improved properties in CMA 10h samples at 350°C lies in improved flow due to decreased viscosity (see Section 9.1.4). Comparing CMA 10h samples to Mixed samples, no significant differences were measured except for samples molded at 370°C, where the CMA 10h sample properties were inferior to those of the Mixed samples. These data are important because they demonstrate that the time and expense expended to cryogenically mechanically alloying this system did not result in a significant improvement in properties over samples which were “hand-mixed” prior to injection molding. (For example, liquid nitrogen for one 35g batch costs approximately \$120.) Processing these materials in the ball mill (regardless of time or number of balls used) does not positively influence the properties of the subsequently injection molded bars. The decline in mechanical properties with mechanical alloying could be due to a number of factors, including changes in molecular weight distribution, thermal

degradation, molding residual stresses, viscosity, and non-equilibrium microstructure. A discussion of differences in these systems, and possible explanations for their different behavior follows.

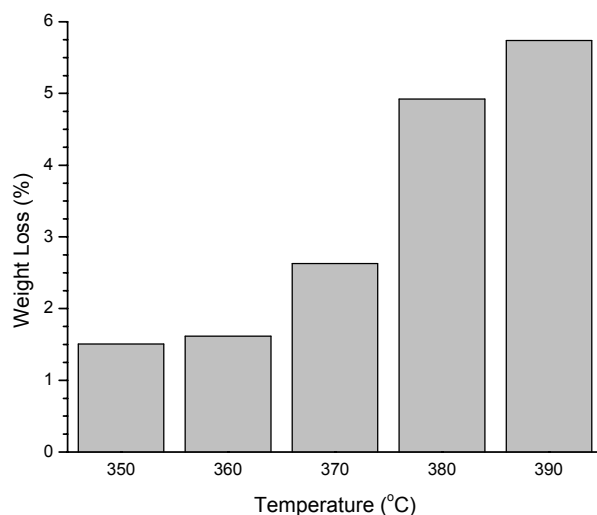
### 9.1.2 Degradation Issues

CMA 10h samples injection molded at 370°C exhibit a decrease in measured mechanical properties compared to samples molded at all other temperatures. Because the trend is not observed for Mixed and Control samples, one might speculate that the CMA 10h samples were degraded during the CMA process. However, if degradation were the only contributing factor for decreased properties, one would not expect to see the subsequent improvement of properties that is observed at 380°C and 390°C molding temperatures. Therefore, degradation is not the sole reason for the decrease in properties at 370°C. Infrared spectroscopy and thermogravimetric analysis data support this claim. Figure 8.9 shows IR data that indicate that no detectable chemical changes occur in the CMA 10h sample after 10 hours of MA compared to Unmilled samples. Gel permeation chromatography data suggests that the molecular weight of the PC phase is slightly lowered by cryogenic mechanical milling for 10 hours, while increasing the polydispersity index of the distributions. Wide angle X-ray patterns of PEEK CMM 10h suggest that mechanical milling amorphizes PEEK at long milling times. Melt rheology data obtained for Unmilled PEEK and PEEK CMM 10h samples, indicate that the molecular weight distribution of the PEEK phase is significantly lowered by long milling times.

Figure 8.8 shows TGA results for cryogenic mechanical alloying times up to 10 hours, with no decrease in the measured degradation temperature of either phase. A drastic decrease in molecular weight would be expected to decrease degradation temperature. The values reported here are approximately 125°C above the highest injection molding temperature employed in this work. Additional tests conducted in an air environment indicated that the presence of oxygen lowers the measured degradation temperature by approximately 25°C. The values measured during the TGA temperature scan differ from the onset of degradation during molding for several reasons. First of all, the values reported are not onset values. In addition, the molding process includes a 5 minute hold at the injection molding temperature. Since

degradation is a kinetic process, additional degradation may occur during this temperature hold. Lastly, the existence of the shear force used during molding may cause additional degradation that is not measured in TGA tests.

In order to elucidate the effects of time spent at the molding temperature on CMA 10h material during heating in the barrel, TGA simulations of the molding process were conducted in air. These tests consisted of heating the powder to each injection molding temperature, followed by a 5 minute hold, during which weight loss was recorded. The weight loss results (shown in Figure 9.5) reveal that thermal degradation increases with temperature during heating in the mold barrel. During the 390°C molding condition, nearly 6% of weight is lost during the heating step. Even more degradation may occur due to shear exposure during molding, which may cause chain scission. Specific degradation mechanisms for PC have been reviewed by Robertson,<sup>56</sup> and subsequent molecular weight and property changes resulting from thermal degradation in this temperature range have been reported.

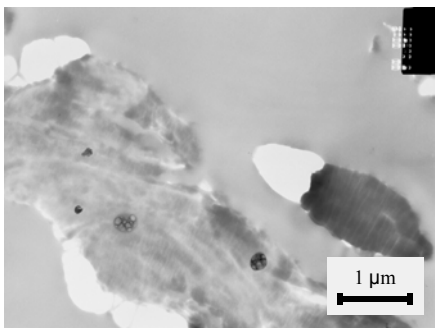
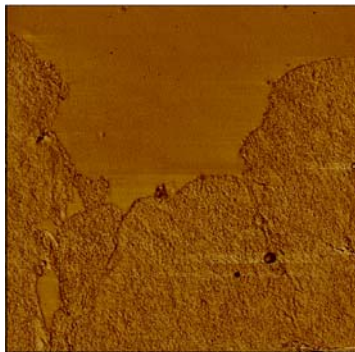
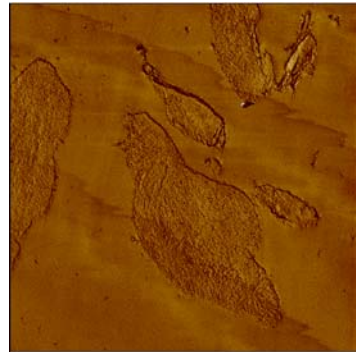
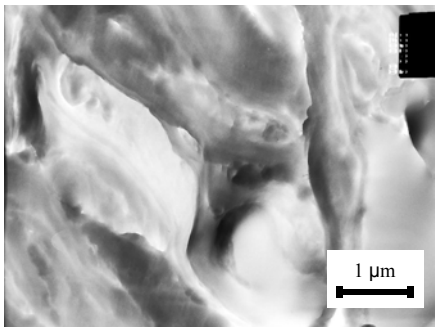
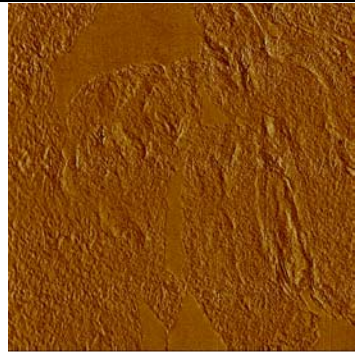
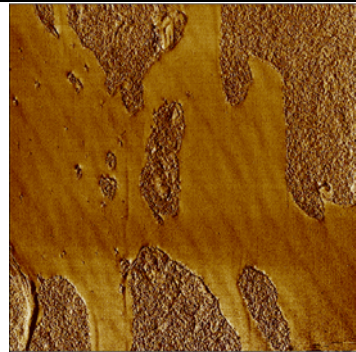


**Figure 9.5:** Weight loss results for CMA 10h powders held at temperature for 5 minutes.

While degradation or chemical changes cannot explain the decrease in mechanical properties measured for the CMA 10h samples injection molded at 370°C, these data suggest that some degradation of the mechanically alloyed material does occur during heating and molding. In industrial practice, this problem could be partially addressed by the use of antioxidants or other protective additives.

### 9.1.3 Microstructural Issues

While it may be assumed that the microstructure of the Mixed and Control powders does not change during heating in the barrel or injection into the mold, the CMA 10h powders have the added issue of possessing a highly non-equilibrium microstructure. Due to the fact that Control samples were exposed to milling conditions for a short period of time, these samples also are likely to exhibit some degree of non-equilibrium behavior. Microscopy revealed that the Control powders consist mainly of individual PEEK and PC particles (Table 9.1), while the CMA 10h powders are intimately mixed. The microstructure in the CMA 10h powders is lost upon heating and molding, as the Control and CMA 10h injection molded coupons both exhibit PEEK phases in a continuous PC matrix, with phase domains on similar scales. While quantification of phase domain sizes may be possible, many more samples would have to be imaged for statistical analysis. Micrographs presented here serve the purpose of demonstrating that the coupons molded from CMA 10h powders have substantially demixed during molding.

	Before Injection Molding <i>Powder sample</i>	After Injection Molding at 370°C <i>Molded bar sample</i>	After Injection Molding at 390°C <i>Molded bar sample</i>
Control			
CMA 10h			

**Table 9.1:** Microstructure comparison before and after injection molding for Control and CMA 10h samples.

In addition to differences in the degree of mixing present in the powders, the amount of crystallinity in the PEEK phase is different in Mixed, Control, and CMA 10h powders. Wide angle X-ray diffraction data revealed that, after exposure to Control conditions, the crystallinity index of the PEEK phase is reduced compared to the PEEK present in the Mixed samples (Figure 6.15). These data also showed that the PEEK phase within the CMA 10h powders, however, is essentially amorphous. These findings are corroborated by results from differential scanning calorimetry (DSC). The area of the crystallization peaks exhibited by cryogenically mechanically milled PEEK samples is larger than those of Unmilled PEEK samples, indicating that mechanically milled samples are less crystalline prior to heating during the DSC test. It may also be noted that the area of the crystallization peaks of Mixed samples are approximately half those of the Unmilled PEEK samples because the Mixed samples consist of 50% PEEK by volume. For the samples molded at 350°C, melting is not fully achieved, leaving some unmelted crystals in the sample. The difference in the amount of crystallinity present in Mixed, Control, and CMA 10h powders affects viscosity, which may affect the formation of residual stresses during molding.

In addition to differences in the amount of crystallinity present in the samples, analysis of DSC data also reveals that the crystallization temperature ( $T_c$ ) of PEEK samples changes with cryogenic mechanical milling time (Figure 6.13). The measured  $T_c$  decreases with increased MM because the PEEK chains are increasingly strained by the mechanical milling process, reducing the thermal activation energy required for crystallization to occur. No change in glass transition temperature was measured with cryogenic mechanical milling of PEEK, however.

The microstructure of the tested coupons is not revealed in scanning electron micrographs of the fracture surfaces (Figure 7.37 and Figure 8.45). If drastic differences existed between mechanically alloyed samples and non-mechanically alloyed ones, SEM might be useful for determining differences the mode of failure. Because Mixed, Control, and CMA 10h samples behaved similarly, no conclusions can be drawn from scanning electron micrographs.

#### 9.1.4 Molding Issues

The highly non-equilibrium microstructures resultant from the mechanical alloying process may contain stored energy from the CMA process.<sup>1,57</sup> This stored energy contributes to phase demixing during the molding process and subsequent heating during DMA tests. Dynamic mechanical data give some insight into differences in Mixed and Control injection molded bars and CMA 10h bars. This analysis is complicated by the fact that two events may occur simultaneously during the DMA test. First, residual stresses locked into the molded coupons during molding may be relaxed when the coupons are subsequently heated. Secondly, demixing of the phases may be occurring during heating, especially in the CMA 10h coupons, where the microstructure is believed to be in a non-equilibrium state. Shoulders or peaks were observed in the DMA storage modulus prior to  $T_g$  for most Mixed and Control samples. In CMA 10h samples, peaks were observed in the storage modulus at all injection molding temperatures. In order to determine if this was a reversible phenomenon, bars from each sample set were annealed above  $T_g$ . The annealing step also allowed some degree of additional demixing to occur prior to the DMA test, presumably more so in the CMA 10h samples than in the others. This annealing step relieved the non-equilibrium stresses resulting from injection molding. Proof lies in examination of the storage modulus curves before and after annealing, where a peak or shoulder is present in the storage modulus of as-molded bars, but is absent in annealed bars. Figure 9.6 shows DMA curves for an as-molded CMA 10h sample and a CMA 10h annealed sample.

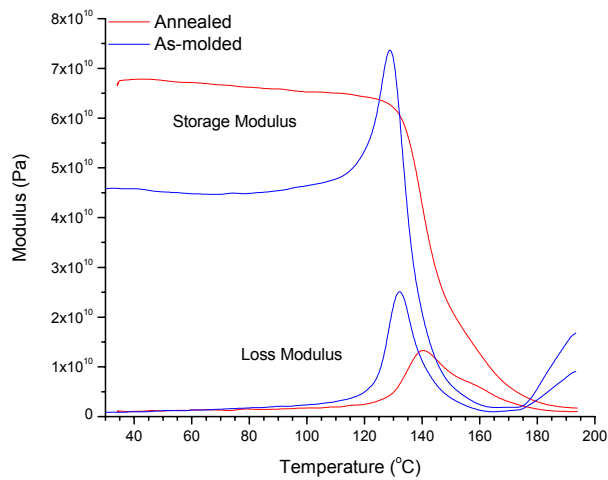
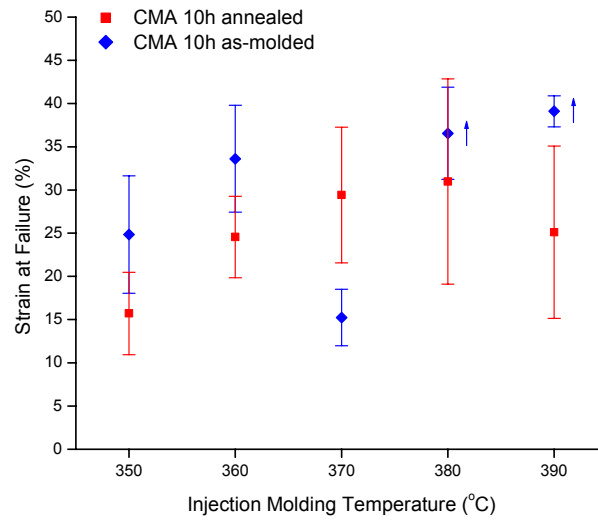


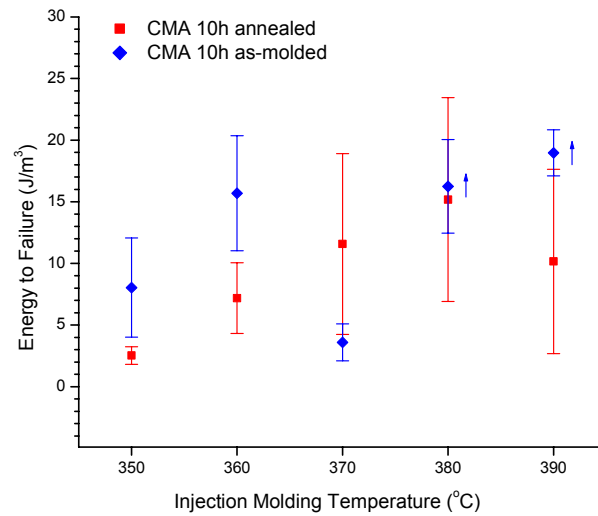
**Figure 9.6:** Annealed vs. as-molded CMA 10h samples, molded at 360°C.

In addition, the annealed bars have higher initial storage modulus values as well as higher loss peaks and broader transitions, which may be a consequence of free volume reduction. CMA 10h annealed bars showed no decrease in properties at 370°C compared to other temperatures, indicating that the drop in properties at 370°C in as-molded coupons was due to residual stresses locked in during molding at this temperature. The presence of residual stresses means that the polymer chains in this sample will fail at a lower applied stress because the chains are already experiencing some stress prior to applying a load during testing. T-tests revealed that annealed samples failed at significantly lower strains than the as-molded ones at all molding temperatures except at 370°C, where the annealed samples exhibited significantly higher strains at failure (Figure 9.7a). The lower strain values contributed to lower toughness values (Figure 9.7b) at all molding temperatures except 370°C. Once the residual stresses in as-molded samples were relieved via annealing, the properties returned to values comparable to CMA 10h as-molded properties at other injection molding temperatures. The failure strengths of annealed samples were not statistically different than those of the CMA 10h as-molded samples except at 350°C and 370°C molding temperatures. At the lowest molding temperature (350°C), it is likely that the most non-equilibrium microstructure is locked into the CMA 10h molded bar, so the most demixing is likely to occur upon annealing. In the case of the CMA 10h annealed bars, it is possible that this sample demixed so much during annealing that the strength is decreased below

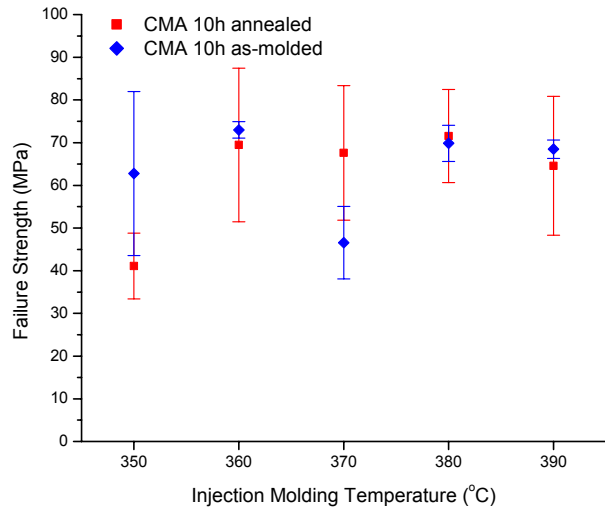
that of the CMA 10h as-molded sample. An expected improvement in strength occurs for CMA 10h annealed samples at the 370°C molding temperature with the relaxation of residual stresses from molding. Figure 9.7a-c shows a comparison of CMA 10h annealed and as-molded samples.



(a)



(b)

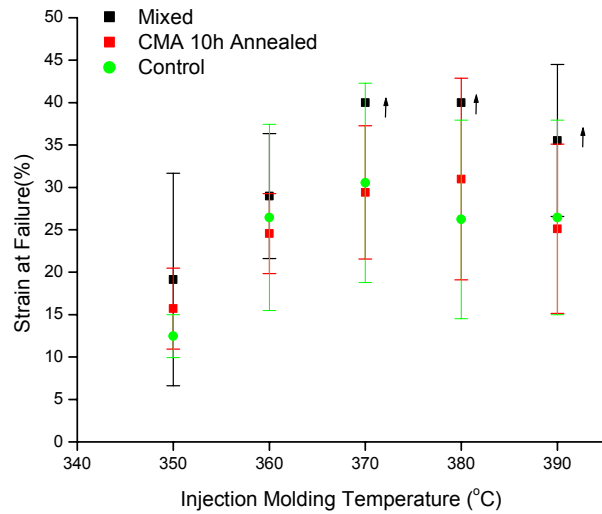


(c)

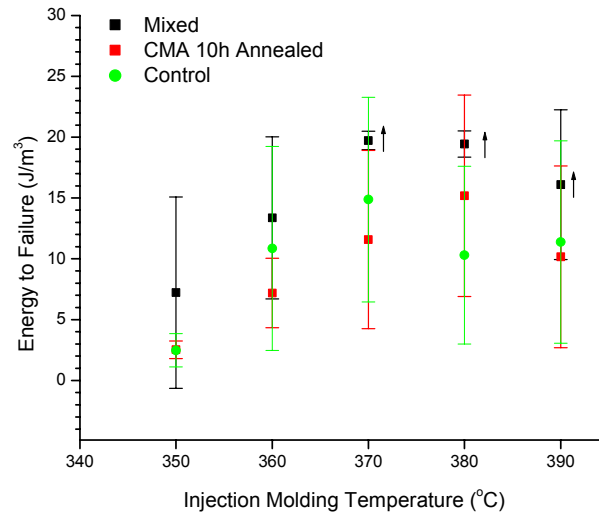
**Figure 9.7:** Property change with injection molding temperature for CMA 10h annealed and CMA 10h as-molded samples (a) strain at failure, (b) energy to failure and (c) failure strength. Arrows indicate samples where actual values are higher than measured values because the test was stopped at 40% strain.

A comparison of CMA 10h annealed samples to Control and Mixed samples is shown in Figure 9.8a-c.

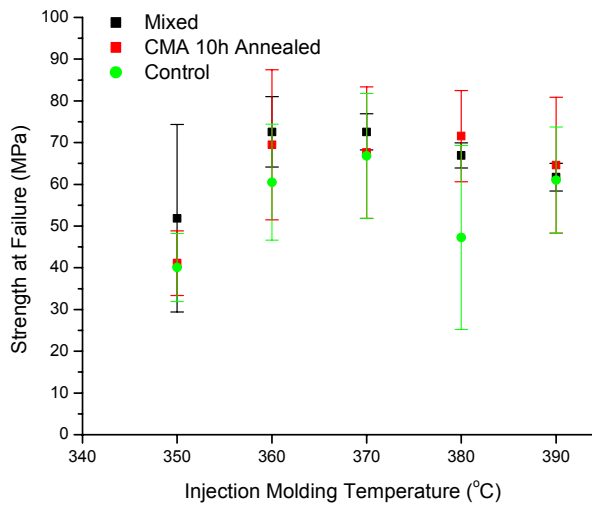
These data again point to the fact that the efforts to mechanically alloy this system (with or without subsequent annealing) did not result in superior mechanical properties compared to a hand-mixed system.



(a)



(b)



(c)

**Figure 9.8:** Property change with injection molding temperature for Mixed, CMA 10h as-molded, and CMA 10h annealed samples (a) strain at failure, (b) energy to failure and (c) failure strength. Arrows indicate samples where actual values are higher than measured values because the test was stopped at 40% strain.

While residual stresses from the molding process can be blamed for the decreased properties of CMA 10h coupons at one molding temperature, this explanation cannot account for the lack of mechanical

property improvement for the CMA 10h samples as a whole as compared to Mixed or Control samples. The CMA 10h samples do not achieve improvements in measured mechanical properties because the intimately mixed microstructure present in the powders is not retained in subsequently molded coupons. With microstructural phase domains of similar scale to those of Mixed and Control samples, the CMA 10h samples do not realize any improvement in mechanical properties. In fact, at some molding temperatures, subjecting the system to the mechanical alloying process seems to be a detriment to properties. One possible explanation for the decrease in measured properties is the decrease in molecular weight of both phases. This is not conclusive, however, since the molecular weight of a polymer only influences its properties to a significant degree if the polymer is below its critical molecular weight for entanglements. Even after cryogenic mechanical milling for 10h hours, the molecular weight averages of both phases are above their critical molecular weight for entanglement.

## **9.2 Summary and Conclusions**

Results from this study indicate these cryogenic mechanical alloying conditions result in powders that are physically mixed on an intimate level. When powders are post-processed via injection molding into testable coupons, the resulting bars exhibit different trends in measured mechanical properties as a function of injection molding temperature compared to Mixed and Control samples. The differences between CMA 10h and Mixed or Control samples (namely, the decrease in properties at 370°C) are attributed mainly to residual stresses from the molding process. Cryogenically mechanically alloying this system for 10 hours does not improve mechanical properties of injection molded coupons such as toughness, strain at failure, and failure strength compared to Mixed samples. This study has demonstrated that even with minimal post-MA processing conditions, the mechanically alloyed microstructure was not retained upon post-processing in the melt. The molded microstructure is of similar scale as that of the Control samples, and has the added complication of being a highly non-equilibrium structure. Therefore, any anticipated physical property benefit derived from the intimate phase mixing during mechanical alloying is likely to be lost upon post-MA processing. In addition, the cryogenic temperatures and long times necessary to achieve intimate mixing

using this ball mill involve a high cost of time, energy, and resources (namely liquid nitrogen). Cryogenic mechanical alloying is therefore not warranted if this system is to be subsequently processed above  $T_g$ .

### **9.3 Contribution and Impact**

Although the subject of mechanically alloying polymers has been present in the literature for almost 15 years, the ultimate goal of the majority of the published work has been an elusive improvement in mechanical properties, which researchers assumed would occur as a result of intimate mixing of phases. Until very recently, none of the published studies addressed the issue of post-MA processing, preferring to address properties of consolidated billets rather than thermally processing the materials into a useful part. Even once this issue was first addressed by a study at Virginia Tech<sup>7</sup> and then at North Carolina State University,<sup>2,3,10,11,13</sup> mechanically alloyed powders were simply pressed in a hot press, ignoring the realistic component of shear which is present in nearly all industrial processes. What is needed in this field is not additional studies promising that judicious selection of specialty or commodity materials will someday realize an improvement in mechanical properties, but nothing less than a shift in the focus of research on this topic. It should not be surprising that these novel materials cannot be successfully processed by traditional polymer processing methods. By highlighting some of the limitations of the MA process and the misleading assumptions of some previous studies, this work has the potential to refocus the energies of researchers in this area toward understanding what additional knowledge is necessary to exploit the novelty of the MA process and the resultant mechanically alloyed materials. A discussion of some of the potential applications of mechanically alloyed polymers follows.

### **9.4 The Future of Mechanically Alloying Polymers**

There are scenarios where MA of polymers has the potential to be useful for purposes other than creating polymer-polymer blends with fine microstructures or superior mechanical properties compared to blends created via other methods. These applications can be classified into one of several categories. First,

there are uses where the chemistry of the system is purposefully exploited *in situ* during the MA process. These applications may include recycling applications, the incorporation of compatibilizers, the purposeful cross-linking of a system, the creation of graft copolymers, etc. Other applications may require fine physical dispersion of one phase in another in the solid state because thermal processing is either not possible or not desirable. In these cases, the retention of the mechanically alloyed microstructure during a traditional melt processing step may not be the goal. Examples of these applications may include the mechanical alloying of a ceramic or dielectric material with a polymer, the dispersion of a solid curing agent in a solid thermoset (for future thermal processing), or the dispersion of carbon black in a polymer for the purpose of improving ultraviolet stability or electrical conductivity. A subset of this category is the use of a small amount of high temperature polymer as a filler in a lower temperature polymer. Finally, MA of polymers may prove feasible for some applications where the final post-MA processing step does not require flow on a bulk scale (such as selective laser sintering, a rapid prototyping process described later) so that retention of the mechanically alloyed microstructure is possible without inducing chemical changes or adding compatibilizers.

By using systems in which cross-linking occurs during the mechanical alloying process, phase demixing in the post-processing step can be slowed or hindered. For example, in work performed at North Carolina State University,<sup>9</sup> cross-linking of polyisoprene and PMMA during mechanical alloying afforded the opportunity to partially retain some of the intimate mixing produced by MA. Here, cross-linking during MA caused the polymer chains to become increasingly constrained, making it more difficult for them to gain mobility when processed above  $T_g$ . This study concluded that in systems where macromolecular reactions do not occur with milling, processing above the  $T_g$  of the components causes phase demixing and the intimate mixing is lost. Results from the current work indicate this may be compounded by the addition of a shear component.

Alternately, retention of the mixing produced by mechanical alloying after post-processing can also be achieved by incorporating a block copolymer.<sup>10</sup> The small additions of copolymer not only reduced the size of the phases (compared to blends formed without the copolymer), but aided in microstructural retention at temperatures above  $T_g$ . A significant improvement in impact strength was also found for this system when a

copolymer was incorporated. Although no literature was found on specific experimental techniques, it has been suggested that the creation of graft or block co-polymers via MA may be possible by careful control of chain scission and subsequent recombination.<sup>2,6,10,11</sup>

Recycling applications using MA have also shown promise. One study from North Carolina State University investigated potential recycling applications using systems consisting of scrap tire material and PMMA, scrap tire and PET, and tertiary blends of synthetic rubber (polyisoprene)/tire/PMMA.<sup>48</sup> The authors hypothesized that possible chain scission and free radical formation during the MA process may be advantageous in producing a rubber toughened polymer blend by concurrently increasing dispersion of the tire within a matrix polymer, breaking down tire material, and producing a surface which is chemically active, and thereby potentially forming new bonds. Although the tire material was more resistant to breakdown than synthetic rubber due to wear-reducing additives, sub-micron dispersions of tire materials within the matrices of other polymers were achieved and further research is ongoing. The process for this application would need to be scaled-up in an economic fashion in order to become a commercially viable process.

Mechanical alloying is also useful when thermal dispersion or processing is not desirable or possible. One study at Virginia Tech<sup>58</sup> utilized mechanical alloying to disperse a ceramic in a polymer matrix, creating a biocomposite for use in intramedullary fracture fixation devices. The composite formed consisted of a copolymer matrix (poly(hydroxybutyrate)-poly(hydroxyvalerate)) reinforced with tri-calcium phosphate, a ceramic material similar to natural bone. Mechanically alloyed powders were consolidated into rods using a die and cold press, followed by hot pressing. Thermal analysis indicated no significant changes in thermal properties due to mechanical alloying, and X-ray diffraction data indicated that no phase changes or crystallinity changes occurred, with the exception of a possible decrease in spherulite size. Mechanical testing of these rods revealed modulus and strength values closer to those of actual bone than the material currently used in this application, 316L stainless steel, but still an order of magnitude lower than actual bone. This work demonstrated successful dispersion of a ceramic reinforcing filler in a polymer matrix via MA to form a composite with superior properties.

Mechanical alloying has also been shown to be useful for dispersing ceramic fillers such as carbon black and silica clay within an elastomer matrix such as natural rubber and styrene-butadiene rubber without degradation to the rubber phase.<sup>59</sup> One study, conducted at Virginia Tech and sponsored by Michelin, investigated the use of MA for dispersing ceramic fillers in elastomer matrices in order to achieve better dispersion and more desirable properties (such as increased modulus) than current industry techniques.<sup>59</sup> Better uniformity of phases was found for melt pressed films that were mechanically alloyed first, compared to melt-pressed films that had not been previously mechanically alloyed. The mechanically alloyed systems exhibited very uniform phase distribution with no agglomerations, and higher modulus and maximum stress values than non-milled samples. Mechanical alloying could also be used to disperse other ceramic fillers such as talc or calcium carbonate in a polymeric matrix.

While these applications used the MA technique to improve mechanical properties of systems via improved dispersion of phases, other mechanical alloying applications may aim at improving electrical, optical, or dielectric properties. These improvements may be achieved by simply attaining finer dispersions of phases selected for their specific properties than is possible via other techniques. Namboodri *et al.*<sup>47</sup> studied the use of MA for creating ceramic-polymer grain boundary capacitors. In this study, mechanical alloying was used to coat BaTiO<sub>3</sub> with LaRC-TPI to make a low loss composite capacitor. This method achieved the same result as the conventional method of solution coating the polymer onto the ceramic material. Because the capacitor's dielectric properties depended on a trade-off between decreasing the size of the BaTiO<sub>3</sub> phase and fully coating the ceramic with the insulating polymer, optimum mechanical alloying conditions had to be found. The resultant composite capacitor possessed values for dielectric loss and dielectric constant that were better than the best composite capacitor formed by solution coating method, thus proving the efficacy of MA for this application. An additional category for non-mechanical property improvement involves the use of mechanically alloyed materials in sensor applications. The increased surface area created by the MA process may prove useful for creating novel materials which could be combined using low temperatures, high pressures and long consolidation times.

Other potential applications for mechanical alloying of polymers include uses in solid freeform fabrication, especially selective laser sintering (SLS), which enables parts of any geometry to be formed directly from computer CAD files. In SLS, a powder bed is rolled out, and a laser rasters across the powder, selectively “sintering” the particles into a thin layer of the desired design (Figure 9.9).

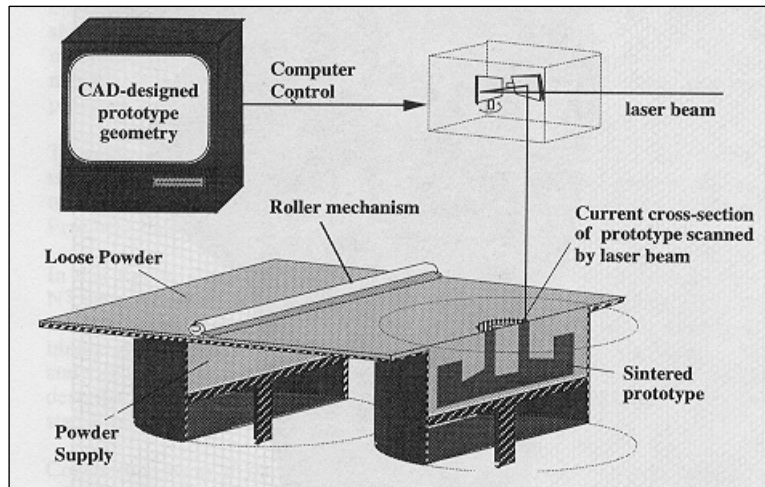


**Figure 9.9:** Selective laser sintering equipment schematic.<sup>60</sup>

More powder is then rolled onto the bed, and multiple layers are built up, eventually forming the desired geometry. This technique is a candidate technique for post-processing mechanically alloyed blends without gross phase separation because the polymers never flow in the bulk or experience shear during consolidation into parts.<sup>52,54</sup> In addition, the SLS process can be used to form any geometry, and, therefore, has an advantage over other no-shear processes such as hot pressing. If this industry is to move towards producing functional parts rather than prototypes, using a mixture of two polymers will be necessary in order to achieve a composite part with a combination of the components' desirable properties. Work has been conducted regarding the use of MA to form polymer blends for SLS applications at Virginia Tech.<sup>52,54</sup> This research reported inferior parts made from mechanically alloyed powders due to increased porosity of the mechanically alloyed parts compared to mixed combinations of the two homopolymers. Because mechanical alloying causes increased particle surface roughness, as well as producing larger, flatter particles, packing in the powder bed was less efficient for these materials. Particle shape and size are

extremely important for SLS applications, so it may be necessary to modify the design of an SLS bed system to accommodate flattened particles or reshape flattened particles.

Other work has been conducted at Virginia Tech<sup>61</sup> using mechanical alloying to create metal or ceramic SLS materials coated with a polymer binder. Currently, a spray-drying method is used to apply a polymer binder for SLS metal and ceramic parts. In order to directly sinter a metal or ceramic material during the actual SLS process, high laser power, high powder bed temperatures, and a reducing atmosphere is necessary. By coating these materials with a polymer binder, a green part can be formed during SLS, which is then sintered in a furnace where the polymer binder is burned out and densification occurs. It is possible to simply mix a polymer binder in with the ceramic or metal material prior to the SLS process, but higher part strengths were found for materials coated with a polymer binder either by spray drying or mechanical alloying because the binder is more intimately mixed. However, similar problems exist in these systems as with polymer-polymer SLS materials regarding particle shape and size, resulting in a porous green part in this case. Materials subject to milling possessed a narrower particle size distribution and larger average particle size than unmilled materials. These particle size distributions are detrimental to efficiently packing the powder bed, as small particles are necessary to fill voids during rolling. If these issues were addressed, this process could be used to augment a commercial SLS process. If a solid thermoset material and solid curing agent were desired for use in a SLS application, it would be impossible to disperse the phases thermally without causing an unwanted chemical reaction during the mixing process. Mechanically alloying the phases prior to selective laser sintering may achieve the desired dispersion in the solid state.

## 10. FUTURE WORK

Future work can be discussed in terms of extensions of the current study, or in terms of new directions for mechanically alloying polymers. Some specific experiments that may enhance this study are proposed in Section 10.1, and general directions for new or continued areas of research introduced in Section 9.4 are discussed in Section 10.2.

### 10.1 Extensions of This Study

There are a few areas where additional testing might elucidate the results obtained in the current study. Additional DMA testing and STXM data may help answer some questions raised in this work. Dynamic mechanical frequency scans were attempted with no success, but further exploration of this technique may yield a successful isothermal testing method to obtain the dynamic mechanical properties of this system without the added complication of *in situ* demixing during DMA testing. If more STXM time could be obtained at Brookhaven National Laboratory, a more thorough investigation of the microstructure of each injection molded bar as well as Control and CMA 10h powders would be desirable. Work at NCSU has used this technique with some success to study the microstructure of melt-pressed films made from mechanically alloyed powders.

One limitation to the work done in this study is the lack of current ability to compare the properties and microstructure of the cryogenically mechanically alloyed material to an analogous system blended thermally (rather than “hand-mixed”) using industrial equipment. Given the current ball mill capabilities, producing coupons using industrial equipment is out of the question due to the extremely large amount of mechanically alloyed polymer required. It may be possible, however, to thermally blend PC and PEEK using industrial equipment, pelletize the blend, and then use the laboratory Microinjector to produce coupons using the same conditions from this study. This capability will be available soon in Center for High Performance Manufacturing labs at Virginia Tech and James Madison University, which would allow a comparison of the mechanically alloyed material to an industrial blend of the same materials.

If future studies are to take place, a redesign of the ball mill would be desirable. The ball mill used in this work was designed with cryogenic capability and ease of design scale-up being of utmost importance. For these purposes, it works well. Because of the linear motion of the vial, however, it is an inefficient design because powder is allowed to fall to the bottom of the vial, making long milling times necessary. Other studies of cryogenically mechanically alloyed polymer at NCSU fitted a commercial SPEX mill with a liquid nitrogen sleeve. This approach is an alternative one for achieving cryogenic capabilities, but the SPEX mill has a batch capability of one-third of the one used in this work, making even more replicate runs necessary to get an appreciable amount of sample powder. Even the use of this commercial mill required milling times up to 24 hours. Recently, SPEX introduced a new ball mill (SPEX 6850) capable of milling 50cm<sup>3</sup> of material at cryogenic temperatures. This mill has potential for use in laboratory scale studies and its 3-axis motion is superior to the mill used in this work. It may be found, however, that cryogenic temperatures are not necessary to process polymers in a ball mill; a “refrigerated” system may be sufficient. Designing a mill without cryogenic capabilities would certainly limit its use to polymers with higher  $T_g$ 's. No studies have been performed on such a system. A new ball mill design, preferably one that could produce larger batches of material, would be necessary for efficiently studying new directions in mechanically alloying polymers.

## **10.2 New Directions for Mechanically Alloying Polymers**

### **10.2.1 Fundamental Demixing Studies**

If it is determined that mechanical alloying holds no promise for producing commercially viable blends, it may be possible to use the mechanical alloying technique to achieve finely mixed phases for fundamental demixing studies on subsequently heated powders. Microstructural demixing during subsequent heating could be studied as a function of molecular weight for mechanically alloyed systems, then their microstructures could be investigated. Since demixing kinetics are slow in polymer systems compared to small molecule systems, it may be possible to watch the demixing as a function of molecular weight, temperature, and time for mechanically alloyed blends.<sup>3,10,11,13</sup> Nucleation and growth or spinodal

decomposition studies could be performed with carefully controlled temperature in a system without impurities. The size of phase domains could be investigated using small angle X-ray scattering or small angle light scattering methods in quenched films, or could be monitored real-time using an environmental scanning electron microscope. In addition, the MA technique could be employed in compositional studies on model polymer systems that are known to exhibit some solubility in one another.

### **10.2.2 Novel Materials for Selective Laser Sintering**

One promising application for mechanically alloying polymers is the use of mechanically alloyed materials for selective laser sintering. Recent studies have revealed that a major limitation to this use is the change of powder size and shape that occurs upon mechanical alloying, which adversely affects the packing of the powders into the SLS bed.<sup>52,54,61</sup> In order for mechanical alloying to be used for SLS, an investigation should first be done to determine if the intimately mixed microstructure can, in fact, be retained upon selective laser sintering. Techniques similar to ones used here could be employed to determine microstructure after cryogenic mechanical alloying and before SLS, as well as after selectively laser sintering at various conditions. While the commercial SLS equipment requires a large amount of material to be used, a laboratory scale SLS machine such as the one built at Virginia Tech<sup>52</sup> could be used for initial studies. If it is shown that the intimately mixed microstructure can be retained in testable parts produced by this technique, then the issues regarding packing the bed as well as batch scale-up capabilities should be addressed. The design of an SLS unit could be modified to accommodate the more flake-like particles resultant from the MA process. For example, rather than packing the powder bed using a rolling mechanism, the powders could be placed in the bed, ultrasonically vibrated to enhance packing, then further packed by pressing the powder bed with a plate from above.

If these issues were addressed, excessive sample porosity may be eliminated and the mechanically alloyed powders are likely to produce a quality selectively laser sintered part. The SLS technique could also be used in combination with using a reactive polymer-polymer systems, or the dispersing capabilities of MA

could be exploited for use in selectively laser sintered polymer-solid curing agent, polymer-ceramic, or polymer-metal systems.

### 10.2.3 Reactive Systems

If retention of mechanically alloyed microstructure is the goal for polymer-polymer systems, a shift in research focus is needed to systems where the chemistry of the system can be exploited to form *in situ* reactions during the mechanical alloying process. It has been shown that the addition of solid compatibilizers to the vial assists in the retention of the mechanically alloyed microstructure upon subsequent heating.<sup>10</sup> Additionally, polymers that partially cross-link during mechanical alloying hold promise for the retention of intimate mixing.<sup>9</sup> In this case, achieving a partial network during MA (which could be completed upon subsequent thermal processing) may allow some retention of the mechanically alloyed microstructure. Both of these areas represent potential for successfully mechanically alloying future polymer-polymer systems. One of the most intriguing possibilities lies in the use of the mechanical alloying technique to form block or graft copolymers *in situ* from homopolymers with reactive end groups. The chemical reaction could be initiated by the addition of mechanical energy from the milling process, UV light during the mechanical alloying process, or perhaps an encapsulated catalyst. If the reactive end groups combined while the phases were being intimately mixed, there would be chemical bonds in place to restrain the chains and limit demixing of the powders during post-processing. Investigation of reactive polymer systems is perhaps the most promising topic for future mechanically alloying studies.

## 11. TECHNICAL ACKNOWLEDGMENTS

Steve McCartney of the Materials Institute at Virginia Tech has proven to be an invaluable resource for this project. The author would like him for technical advice, sample preparation, microscopy instruction and assistance. The author gratefully acknowledges the support of NSF grant #9975678 associated with the FESEM used in this work. Thanks also goes to Frank Cromer in the Chemistry Department for training and use of the SEM.

Scanning transmission X-ray microscopy data was taken using the X-1A STXM developed by the group of Janos Kirz and Chris Jacobsen at SUNY Stony Brook with support from the Office of Biological and Environmental Research, U.S. DoE under contract DE-FG02-89ER60858, and the NSF under grant DBI-9605045. A special thanks goes Dr. Chris Jacobsen and Sue Wirick for help with acquiring and analyzing STXM data.

Thanks go to Ashish Aneja and Dr. Garth Wilkes in the Chemical Engineering Department for use of their lab's FTIR and to Nick Gariano and Dr. Tim Long in the Chemistry Department for use of their melt rheometer. The assistance of Dr. Y. Kim in the Chemistry Department and Dr. Wei Sen Wong at Viscotek in running GPC samples was greatly appreciated. Additional thanks goes to Kate Nelson, who contributed to this project as part of the National Science Foundation SURP program, and to MSE student Kelly Hales, who assisted in the lab.

The author would like to thank Jeff Schultz at Virginia Tech, who designed, built, and kept the ball mill operational throughout this project. He also contributed to numerous technical discussions and offered advice. Additional thanks go to Scott Trenor, Sumitra Subrahmanyam, Julie Uan-Zo-li, and Dr. Eric Pappas for editing and helpful discussions. Finally, the author would like to acknowledge and thank the members of this committee for their assistance in the form of valuable conversations, technical knowledge, ideas, and general support: Ron Kander, Alex Aning, Brian Love, Steve Kampe, and Tom Ward.

## 12. REFERENCES

- <sup>1</sup> Pan, W.J.D., and Shaw, J., *Journal of Applied Polymer Science*, **56**, 1995, 557-566.
- <sup>2</sup> Smith, A.P., et al., *Macromolecular Rapid Communication*, **19**, 1998, 557-561.
- <sup>3</sup> Smith, A.P., et al., *Advanced Materials*, **11**, 1999, 1277-1281.
- <sup>4</sup> Shaw, W.J.D., and Pan, J., *Journal of Applied Polymer Science*, **52**, 1994, 507-514.
- <sup>5</sup> Ishida, T., *Journal of Materials Science Letters*, **13**, 1994, 623-628.
- <sup>6</sup> Balik, C. M., et al., *Materials Research Society Symposium Proceedings*, **461**, 1997, 39-44.
- <sup>7</sup> Farrell, M.P., Kander, R.G., and Aning, A.O., *Journal of Materials Synthesis and Processing*, **4**, 1996, 151-161.
- <sup>8</sup> Smith, et al., *Polymer*, **41**, 2000, 6271-6283.
- <sup>9</sup> Smith, et al., *Macromolecular Materials Engineering*, **274**, 2000, 1-12.
- <sup>10</sup> Smith, et al., *Macromolecules*, **33**, 2000, 1163-1172.
- <sup>11</sup> Smith, et al., *Macromolecules*, **33**, 2000, 2595-2604.
- <sup>12</sup> Smith, et al., *Polymer*, **41**, 2000, 6271-6283.
- <sup>13</sup> Smith, et al., *Macromolecular Materials Engineering*, **274**, 2000, 1-12.
- <sup>14</sup> Shaw, W. J. D., Pan, J. and Gowler, M.A., Proceedings of the Second International Conference on Structural Applications of Mechanical Alloying, 1993, 431-437.
- <sup>15</sup> Koch, C.C. et al., Unpublished report, "Nonequilibrium Processing of Polymeric Materials by Mechanical Attrition."
- <sup>16</sup> Favis, B.D., *The Canadian Journal of Chemical Engineering*, **69**, 1991, 619-625.
- <sup>17</sup> Sperling, L.H., *Introduction to Physical Polymer Science*, 1992, 71-77, 127-140.
- <sup>18</sup> Utracki, L.A. *Polymer Blends and Alloys*, 1989, 1-52.
- <sup>19</sup> Paul, D. R. and Newman, S., Eds, *Polymer Blends*, 1-52.
- <sup>20</sup> Bonner, J.G., and Hope, P.S., in *Polymer Blends and Alloys*, 1993, 46-73.
- <sup>21</sup> Sperling, L. H., *Polymeric Multicomponent Materials: An Introduction*, 1997, 51-79.
- <sup>22</sup> Seo, Hong, and Hwang, *Polymer*, **3**, 1995, 515-523.
- <sup>23</sup> Gilman, P. S. and Benjamin, J. S., *Annual Review in Materials Science*, **13**, 1983, 279-300.
- <sup>24</sup> Benjamin, J.S., *Metallurgical Transactions*, **1**, 1970, 2943-2951.
- <sup>25</sup> Sundareson, R. and Froes, F.H., *Journal of Metals*, 1987, 22-27.
- <sup>26</sup> Han, S.H., Gshneidner, K.A., and Beaudry, B.J., *Scripta Metallurgica et Materialia*, **24**, 1990, 295-298.
- <sup>27</sup> Schaffer, G.B., and McCormick, P.G., *Metallurgical Transactions A*, **23A**, 1992, 1285-1290.
- <sup>28</sup> Hellstern, E., et al., *Journal of Applied Physics*, **65**, 1989, 305-310.
- <sup>29</sup> Schwarz, R.B., Petrich, R.R., and Saw, C.K., *Journal of Non-Crystalline Solids*, **76**, 1985, 281-302.
- <sup>30</sup> Maurice, D.R. and Courtney, T.H., *Metallurgical Transactions A*, **21A**, 1990, 289-303
- <sup>31</sup> Miller, P.J., Coffey, C.S., and DeVast, V.F., *Journal of Applied Physics*, **59**, 1986, 913.
- <sup>32</sup> Davis, R.M., McDermott, B., and Koch, C.C., *Metallurgical Transactions A*, **19A**, 1988, 2867-2874
- <sup>33</sup> Forrester, J.S. and Schaffer, G.B., *Metallurgical and Materials Transactions A*, **26A**, 1995, 725-730.
- <sup>34</sup> Aning, A.O., Wang, Z., and Courtney, T.H., *Acta Metall. Mater.*, **41**, 1993, 164-174.
- <sup>35</sup> Maurice, D.R. and Courtney, T.H., *Metallurgical Transactions A*, **26A**, 1995, 2437-2444
- <sup>36</sup> Maurice, D.R. and Courtney, T.H., *Metallurgical Transactions A*, **26A**, 1995, 2431-2435.
- <sup>37</sup> Maurice, D.R. and Courtney, T.H., *Metallurgical Transactions A*, **27A**, 1996, 1973-1979.
- <sup>38</sup> Maurice, D.R. and Courtney, T.H., *Metallurgical Transactions A*, **27A**, 1996, 1973-1979.
- <sup>39</sup> Maurice, D.R. and Courtney, T.H., *Metallurgical Transactions A*, **25A**, 1994, 147-158.
- <sup>40</sup> Bai, et al, *Polymer*, in press
- <sup>41</sup> Shaw, W.J.D., U.S. Patent #5,367,048, 1994
- <sup>42</sup> Pan, J., and Shaw, W.J.D., *Microstructural Science*, **20**, 351-365
- <sup>43</sup> Pan, J., and Shaw, W.J.D., *Microstructural Science*, **19**, 659-669

- 
- <sup>44</sup> Font, J. Muntasell, J., and Cesari, E., *Materials Research Bulletin*, **32**, 1997,1691-1696.
- <sup>45</sup> Font, J. Muntasell, J., and Cesari, E., *Materials Research Bulletin*, **34**, 1999,157-165.
- <sup>46</sup> Castricum, H.L., *et al.*, *Proceedings of the International Symposium on Metastable, Mechanically Alloyed, and Nanocrystalline Materials*,1996, 211-216.
- <sup>47</sup> Nambodri, S., *et al.*, *Polymer*, **35**, 1994, 4088-4091
- <sup>48</sup> Smith, *et al.*, *Polymer*, **42**, 4453-4457(my #145)
- <sup>49</sup> Bai, C., *Polymer*, 2000,**41**,7147
- <sup>50</sup> Sperling, L. H., *Introduction to Physical Polymer Science, Second Edition*, John Wiley & Sons, 1992, 314-318,368-370.
- <sup>51</sup> Young, R. J., and Lovell, P. A., *Intro to Polymers, Second Edition*, Chapman & Hall, 1991, 331-335.
- <sup>52</sup> Schultz, J., "Materials for Selective Laser Sintering," Honors Senior Thesis at Virginia Polytechnic Institute and State University, 1999.
- <sup>53</sup> Devaux, D., *et al.*, *Polymer*, **26**,1985,1994-2000.
- <sup>54</sup> Schultz, J.P. and Kander, R.G., and Suchicital, C.T.A., *Solid Freeform Fabrication Proceedings*, 1999, 311-317.
- <sup>55</sup> Justi, Sherman, Olariu, *Materials Science Forum*, **166-169**,1994, 109-113.
- <sup>56</sup> Roberston, Jennifer E., "Thermal Degradation Studies of Polycarbonate", Doctoral Dissertation at Virginia Polytechnic Institute and State University, 2001.
- <sup>57</sup> Shaw, W. J. D., *Materials Science Forum*, **269-272**, 19-30.
- <sup>58</sup> Senowitz, C. J., Aning, Alex O., and Stawovy, Michael, "Tri-Calcium Phosphate Reinforced PHB/PHV Copolymer for Use in an Intramedullary Fracture Fixation Device," Report to National Science Foundation Science and Technology Center, August 1995.
- <sup>59</sup> Hales, Kelly D. and Kander, Ronald G., "Mechanical Alloying of Elastomer Filled Systems", Progress Report submitted to Michelin, Inc., August 2000.
- <sup>60</sup> Nelson, J. C., "Selective Laser Sintering: A Definition of the Process and Empirical Sintering Model", Ph.D. dissertation, University of Texas, May 1993.
- <sup>61</sup> Heil, T. M., "Ceramic/Polymer Powders for Selective Laser Sintering", Honors Senior Thesis at Virginia Polytechnic Institute and State University, May 2001.

---

## VITA

Julie P. Martin was born on March 16, 1974 to Patricia and Earl Martin. Julie graduated from Independence High School in Charlotte, North Carolina in 1992. She then attended North Carolina State University (NCSU) in Raleigh, where she was an active member of the Materials Science and Engineering Department and the University Scholars Program. While an undergraduate at NCSU, she participated in the National Science Foundation's Summer Undergraduate Research Program at Virginia Tech in 1994 and 1995, where she first met and collaborated with Dr. Ron Kander. Following graduation from NCSU with honors in 1996, she joined his research group at Virginia Tech. Julie will pursue a post-doctoral research position in the BioEngineering Department at Clemson University upon completion of her Ph.D., redirecting her research interests in the area of absorbable polymer scaffolds for tissue engineering.